8-2019

Uncertainty Estimates in Few-Body Physics

Daniel Odell Jr
University of Tennessee, dodell4@vols.utk.edu

Recommended Citation

Odell, Daniel Jr, "Uncertainty Estimates in Few-Body Physics. " PhD diss., University of Tennessee, 2019.
https://trace.tennessee.edu/utk_graddiss/5587

Uncertainty Estimates in Few-Body Physics

A Dissertation Presented for the
Doctor of Philosophy
Degree
The University of Tennessee, Knoxville

Daniel Mackenzie Odell
August 2019

For my wife, whose enduring patience and countless sacrifices have carried me through failure and success.

Acknowledgments

My continued thanks to my advisor, Lucas Platter, for his persistent guidance, endless supply of ideas, and tenacious problem solving. I would also like to thank Thomas Papenbrock for introducing me to research and demonstrating a contagious curiosity toward physics. In addition, it has been my pleasure to work alongside Bijaya Acharya, Jose Bonilla, Arnoldas Deltuva, and Andreas Ekström as collaborators.

Abstract

Uncertainty estimates in theoretical physics are just as important as they are in experimental physics. As a theorist, one must qualify a given calculation with the assumptions on which the calculation is performed. Such a practice equips the scientific community with the context necessary to evaluate the validity of a theory. It also provides some basis upon which the theory can develop improvements. The work presented here concerns itself with two sources of uncertainty in theoretical physics. First, we discuss numerical uncertainties. Particularly, we quantify the uncertainties introduced by basis truncations and the exploit it to extrapolate infinite-basis results. Second, we examine framework uncertainties — those attributable to the inherent failure of the employed model to describe the fullness of nature. We establish the sufficiency of a two-body contact interaction to renormalize short-distance physics in the two- and three-body sectors of systems where singular potentials relevant to nuclear and atomic dominate the low-energy behavior.

Table of Contents

List of Figures

Chapter 1

Infrared Extrapolations

This section describes the investigation into truncation error. A majority of the content of this section comes from the corresponding publications [45] and [1].

First, we introduce the underlying concepts. Then we apply them to the derivation of an extrapolation formula for the deuteron's quadrupole moment and study our result for a toy model as well as a realistic nucleon-nucleon interaction. We then generalize the extrapolation formula to the case where the bound-state wave functions mix partial waves with orbital angular momenta l and $l+2$, respectively, or where the bound-state has a finite $l > 0$. We generalize those concepts to derive an IR extrapolation formula for $E2$ transition matrix elements between bound states and conclude with a summary. Finally, we extend our analysis from bound-state properties to $E\lambda$ and $M(\lambda+1)$ matrix elements between bound states and the continuum.

1.1 Background

The numerical calculation of observables of strongly interacting systems frequently requires the use of truncated Hilbert spaces. For example, lattice QCD simulations are carried out in a finite volume with periodic boundary conditions. Nuclear structure calculations frequently employ the spherical harmonic oscillator (HO) basis as it preserves rotational symmetry and facilitates a straightforward way of separating out the center-of-mass motion, see, e.g., Refs. [42, 3]. Such calculations require a clear understanding of the quantitative and qualitative corrections due to the imposed Hilbert space truncation. For nuclear structure calculations in the HO basis it was only recently understood that the truncated HO can be thought of as imposing long-range, hard-wall boundary conditions with an additional short distance regulator [18]. Specifically, it was found that a HO basis consisting of N oscillator shells with oscillator length b has an ultraviolet (UV) cutoff [55].

$$\Lambda \approx \sqrt{2N}/b \ , \tag{1.1}$$

while the infrared (IR) cutoff and therefore the spatial extent of the basis is approximately [30, 32]

$$L \approx \sqrt{2N} b \ . \tag{1.2}$$

Relations (1.1) and (1.2) are leading order (LO) approximations and valid for $N \gg 1$. A more precise expression for an HO in three dimensions was derived in Ref. [39]

$$L = \sqrt{2(N_{\max} + 3/2 + 2)} b \ . \tag{1.3}$$

Here, $b = \sqrt{\hbar/(\mu\Omega)}$, μ, and Ω denote the oscillator length, the reduced mass, and the oscillator frequency, respectively. We note that Eq. 1.3 is specific to a two-body system in relative coordinates (or a single particle in three dimensions). Precise values for the IR length scale L were also derived for many-body product spaces [19] and no-core shell model spaces [57].

Previous work [18, 20] have shown the bound-state energies converge as

$$E_L = E_\infty + a_0 e^{-2k_\infty L} \ , \tag{1.4}$$

and radii converge as

$$\langle \hat{r}^2 \rangle_L \approx \langle \hat{r}^2 \rangle_\infty - \left[c_0 (k_\infty L)^3 + c_1 k_\infty L \right] e^{-2k_\infty L} \ . \tag{1.5}$$

Here a_0, k_∞, E_∞, and c_0, c_1, and $\langle \hat{r}^2 \rangle_\infty$ are determined by fitting to numerical data in many-body systems.

In both cases (as well as for the quadrupole moment extrapolation derived below) the $e^{-2k_\infty L}$ term comes from the universal long-range behavior of the radial wave function, $\mathcal{R}_l(r)$. The spherical Hankel functions, $h_l(\pm ikr)$, are the negative-energy solutions in the free region, and imposing a Dirichlet boundary condition such that $R_l(L) = 0$ gives a solution of the form

$$\mathcal{R}_l(r) = h_l(ik_L r) + C h_l(-ik_L r) \ , \tag{1.6}$$

where $C = e^{-2k_L L}$ in LO for $k_L L \gg 1$. Here and in what follows, k_L denotes the momentum of the system bounded by a hard wall at $r = L$, k_∞ denotes the momentum of the system bounded only by the asymptotic boundary condition at $r \to \infty$, and k denotes the momentum of an unspecified system.

1.2 Quadrupole Moments

Derivation Here, we summarize the derivation of an IR extrapolation formula for the quadrupole moment

$$\langle \mathbf{r}' | \, \hat{Q} \, | \mathbf{r} \rangle = e\sqrt{\frac{\pi}{5}} r^2 Y_{20}(\theta, \phi) \delta^{(3)}(\mathbf{r} - \mathbf{r}') \ , \tag{1.7}$$

and take the deuteron as an example. For the deuteron, r is the relative coordinate. While computing the deuteron's quadrupole moment poses no challenge in HO model spaces, it is already challenging to compute converged quadrupole moments in p-shell nuclei, see Refs. [9, 16, 38] for examples. This motivates us to study the IR convergence for bound-state expectation values of the quadrupole moment and for $E2$ transition matrix elements between bound states.

The deuteron is a spin-1, $J = 1$ state

$$|\Psi\rangle = |\Psi_0\rangle + \eta \, |\Psi_2\rangle \ , \tag{1.8}$$

superposed of an S-state Ψ_0 and a D-state Ψ_2. The d-state amplitude is denoted by η. Without loss of generality we focus on the state with maximum $J_z = 1$ spin projection. The wave function for a state with orbital angular momentum l is

$$\Psi_l(r,\theta,\phi) = \mathcal{R}_l(r) \sum_{m,m_s} C^{1,1}_{l,m;1,m_s} Y_{l,m}(\theta,\phi)\chi_{s,m_s} \; . \tag{1.9}$$

Here $\mathcal{R}_l(r)$ denotes the solution to the radial Schrödinger equation. The orbital angular momentum, represented by the spherical harmonics $Y_{lm}(\theta,\phi)$, and spin, represented by the spinor χ_{s,m_s}, are coupled to a total angular momentum $J = 1$ by means of the Clebsch-Gordan coefficient $C^{1,1}_{l,m;1,m_s}$ [56].

For the computation of the IR correction of the quadrupole moment we follow closely the corresponding derivation made in Ref. [20] for the radius squared. In a finite oscillator basis with IR length scale L, the expectation value of the quadrupole moment (1.7) will differ from the infinite-space result, and

$$Q_L = Q_\infty + \Delta Q_L \; . \tag{1.10}$$

Here

$$\Delta Q_L = \frac{\langle\Psi_L|\hat{Q}|\Psi_L\rangle}{\langle\Psi_L|\Psi_L\rangle} - \frac{\langle\Psi_\infty|\hat{Q}|\Psi_\infty\rangle}{\langle\Psi_\infty|\Psi_\infty\rangle} \; , \tag{1.11}$$

defines the expressions for Q_L and Q_∞ such that any L-independent terms will cancel in Eq. (1.11). The wave functions Ψ_L and Ψ_∞ are the deuteron wave functions in the finite and infinite oscillator spaces, respectively.

Using Eqs. (1.8) and (1.9), four terms enter the expectation value in the first term of Eq. (1.11), and

$$\begin{aligned}\langle\Psi_L|\hat{Q}|\Psi_L\rangle = e\sqrt{\frac{\pi}{5}} \int_0^L \int_0^\pi \int_0^{2\pi} \mathrm{d}r r^2 \mathrm{d}\theta \sin\theta \mathrm{d}\phi \left[\mathcal{R}_{L,0} Y^*_{00}\chi^\dagger_1 + \eta\mathcal{R}_{L,2} \sum_{m,m_s} C^{1,1}_{2,m;1,m_s} Y^*_{2m}\chi^\dagger_{m_s}\right] \\ \times r^2 Y_{20} \left[\mathcal{R}_{L,0} Y_{00}\chi_1 + \eta\mathcal{R}_{L,2} \sum_{m,m_s} C^{1,1}_{2,m;1,m_s} Y_{2m}\chi_{m_s}\right] \; .\end{aligned} \tag{1.12}$$

The expectation value in the second term on the right-hand side of Eq. (1.11) is found by replacing L by ∞. The S-S term is zero, so we have only to consider the remaining S-D

mixing terms and the D-D term. Our interest is in the L-dependence of the quadrupole moment which is contained entirely in the radial integrations carried out in the first term on the right-hand side of Eq. (1.11)

$$\int_0^L \mathrm{d}r r^4 \mathcal{R}_{L,0}(r)\mathcal{R}_{L,2}(r) \; , \tag{1.13}$$

and

$$\int_0^L \mathrm{d}r r^4 \mathcal{R}_{L,2}(r)\mathcal{R}_{L,2}(r) \; . \tag{1.14}$$

We assume that the nuclear potential vanishes beyond $r = R$ and split the radial integration into two parts. In general,

$$\int_0^L \mathrm{d}r r^4 \mathcal{R}_{L,l_1}(r)\mathcal{R}_{L,l_2}(r) = \int_0^R \mathrm{d}r r^4 \mathcal{R}_{L,l_1}(r)\mathcal{R}_{L,l_2}(r) + \int_R^L \mathrm{d}r r^4 \mathcal{R}_{L,l_1}(r)\mathcal{R}_{L,l_2}(r) \; . \tag{1.15}$$

The interior region, between 0 and R, depends primarily on the details of the interaction. The resulting L-dependence from the integration over the interior region scales as $\mathcal{O}(L^0)e^{-2kL}$ [20] and therefore does not contribute to the dominant correction terms [the polynomial in kL at $\mathcal{O}(e^{-2kL})$]. We therefore concentrate on the second region between R and L, and consider the integrals

$$\int_R^L \mathrm{d}r r^4 \mathcal{R}_{L,0}(r)\mathcal{R}_{L,2}(r) \; , \tag{1.16}$$

and

$$\int_R^L \mathrm{d}r r^4 \mathcal{R}_{L,2}(r)\mathcal{R}_{L,2}(r) \; , \tag{1.17}$$

in the region free from the potential. Here, the radial wave functions are

$$\mathcal{R}_{L,0}(r) = h_0(ik_L r) + C_0 h_0(-ik_L r) \; , \tag{1.18}$$

with

$$C_0 = -\frac{h_0(ik_L L)}{h_0(-ik_L L)} = e^{-2k_L L} \ , \tag{1.19}$$

and

$$\mathcal{R}_{L,2}(r) = h_2(ik_L r) + C_2 h_2(-ik_L r) \ , \tag{1.20}$$

with

$$C_2 = -\frac{h_2(ik_L L)}{h_2(-ik_L L)} = e^{-2k_L L}\frac{(k_L L)^2 + 3k_L L + 3}{(k_L L)^2 - 3k_L L + 3} \ . \tag{1.21}$$

The coefficients C_0 and C_2 are chosen such that the wave function vanishes at $r = L$.

Restricting our analysis to the highest powers of kL, we arrive at

$$Q_L = Q_\infty - a(k_\infty L)^3 \left(1 + \frac{d}{k_\infty L}\right) e^{-2k_\infty L} \ , \tag{1.22}$$

with corrections of order $\mathcal{O}(k_\infty L e^{-2k_\infty L})$. Here Q_∞, a, d, and k_∞ can be treated as fit parameters. Note that to LO, $k_L \approx k_\infty$, where (in the two-nucleon system)

$$k_L = k_\infty - \gamma_\infty^2 e^{-2k_\infty L} + \mathcal{O}(e^{-4k_\infty L}) \ , \tag{1.23}$$

and γ_∞ is the asymptotic normalization coefficient [20]. The LO term is all we need to determine the polynomial at $\mathcal{O}(e^{-2k_\infty L})$ for Q_L.

Results To test our prediction, we calculate the quadrupole moment of the deuteron using an interaction derived from chiral effective field theory as described in Ref. [37]. For the quadrupole fits, we take the bound-state momentum k_∞ from the known binding energy of the deuteron for this interaction. Fits of the quadrupole moment to Eqs. (1.22) and (1.29) yield virtually identical results and are shown in Fig. 1.1.

One might also try to extract higher-order corrections to the quadrupole moment that are smaller than $\mathcal{O}((k_\infty L)^2 e^{-2k_\infty L})$. These are terms proportional to $(k_\infty L)^m e^{-2k_\infty L}$ with $m \leq 1$, and terms proportional to $e^{-4k_\infty L}$. We define (with $Q(L) \equiv Q_L$)

$$\delta Q_m = \frac{Q_{\text{calculated}} - Q_{m+1}(L)}{c_m (k_\infty L)^m} \ , \tag{1.24}$$

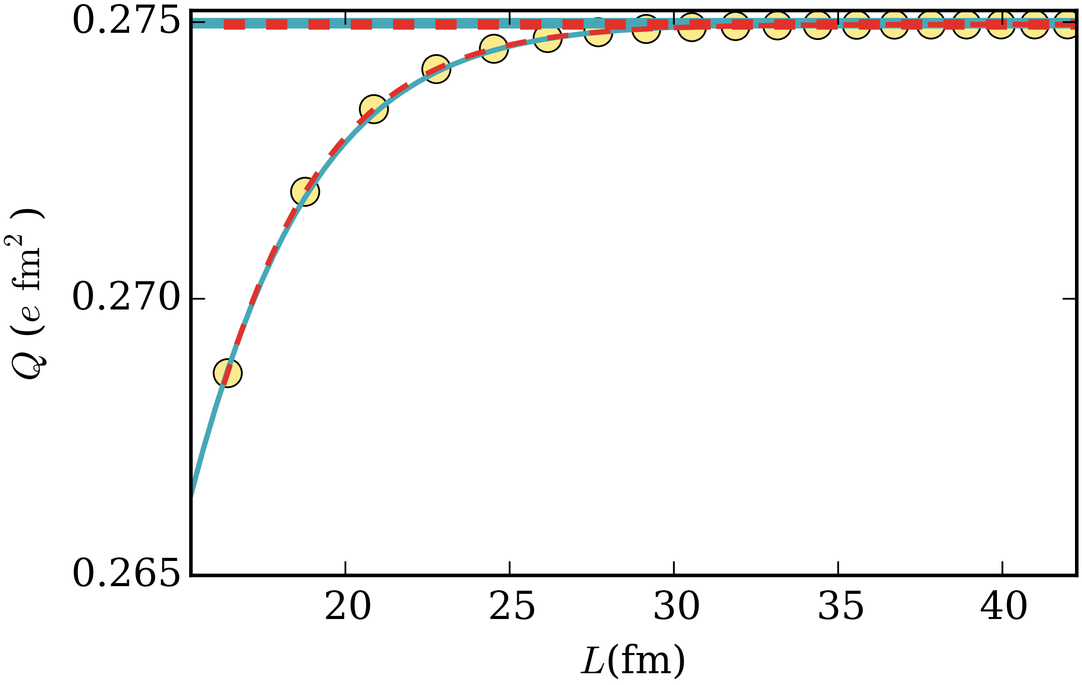

Figure 1.1: Extrapolation of the deuteron quadrupole moment computed from a chiral potential. The yellow circles are the data from the calculation. The thin, blue, solid line is the fit to Eq. (1.29). The thick, blue, solid line is Q_∞ from the fit to Eq. (1.29). The thin, red dashes are the fit to Eq. (1.22), and the thick, red dashes are Q_∞ from the fit to Eq. (1.22).

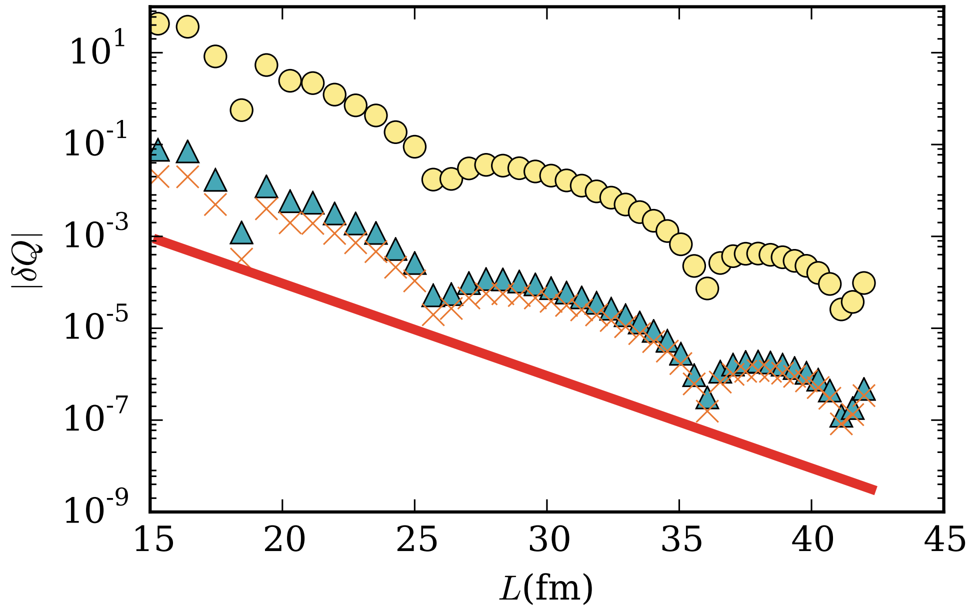

Figure 1.2: The yellow circles represent δQ_1 as defined by Eq. (1.24). The blue triangles represent δQ_0. The orange crosses represent δQ_{-1}. The red line is proportional to $e^{-2k_\infty L}$.

where

$$Q_m(L) = \sum_{n=m}^{3} c_n (k_\infty L)^n e^{-2k_\infty L} \ , \tag{1.25}$$

is the data reproduced with the fit parameters (represented by c_n and c_m). If we plot δQ alongside what we expect analytically, we ought to be able to establish trends for the higher order corrections. The results are shown in Fig. 1.2. The overall slopes of the corrections match well with the predicted slope, and as each lower order of $(k_\infty L)$ is included, the data approaches the $e^{-2k_\infty L}$ line as expected, supporting the validity of our analysis.

1.3 Generalized Angular Momentum States

We can apply this reasoning to a system with an arbitrary mixture of l states, i.e.

$$|\Psi\rangle = |\Psi_{l_1}\rangle + \eta \, |\Psi_{l_2}\rangle \ . \tag{1.26}$$

For simplicity we limit ourselves to LO and consider only the asymptotic form

$$h_l(\rho) \to \frac{i}{\rho} e^{-i(\rho - \frac{l\pi}{2})} , \tag{1.27}$$

of the spherical Hankel functions at large ρ. As before, if we consider $\pm i\rho$ (where $\rho = kr$) solutions and enforce the boundary condition at $r = L$, we have for the radial behavior

$$\mathcal{R}_{L,l}(k_L r) = -\frac{1}{k_L r} e^{i\pi l/2} \left(e^{-k_L r} - e^{-2k_L L} e^{k_L r} \right) . \tag{1.28}$$

We compute the quadrupole moment as before and obtain an expression for the IR extrapolation

$$Q_L = Q_\infty - a(k_\infty L)^3 e^{-2k_\infty L} . \tag{1.29}$$

We see that the general case agrees in LO with the particular case (1.22) for the deuteron. Furthermore, Eq. (1.29) also applies to quadrupole expectation values of bound-states of a single, finite orbital angular momentum $l > 0$. This makes Eq. (1.29) the main result of this section. Higher-order corrections depend on orbital angular momenta involved in the particular case under consideration.

1.4 $E2$ Bound State Transitions

Derivation The quadrupole moment operator also describes electric quadrupole ($E2$) transitions. If we consider a simple model where the initial state is a pure D-wave state and the final state is a pure S-wave state, the amplitude for such a transition is

$$\mathcal{A} = \langle \Psi_0 | \hat{Q} | \Psi_2 \rangle . \tag{1.30}$$

As before, computing such an amplitude in a truncated basis effectively imposes a Dirichlet boundary condition on the wave functions. Likewise, we can describe the amplitude in the truncated basis ($\mathcal{A}_L$) as the amplitude in the infinite basis ($\mathcal{A}_\infty$) plus a correction term.

$$\mathcal{A}_L = \mathcal{A}_\infty + \Delta\mathcal{A}_L , \tag{1.31}$$

and we seek to compute $\Delta\mathcal{A}_L$. We note that the bound-state momentum k_l depends on the state Ψ_l. With Ψ_l from Eq. (1.9), and the radial wave functions from Eqs. (1.18) and (1.20) for $\Psi_{L,0}$ and $\Psi_{L,2}$, respectively, we can easily derive an expression for $\mathcal{A}_L$. Essentially, we need to evaluate Eq. (1.16) for states with different angular momenta (or different k_l values). While the procedure is similar to the calculation of quadrupole moments, the result is somewhat more complex. We obtain (written explicitly as a function of L)

$$\mathcal{A}_L = \mathcal{A}_\infty + a_0 \left[1 + \frac{a_1}{k_2 L} + \mathcal{O}\left(\frac{1}{(k_2 L)^2}\right)\right] e^{-2k_2 L} \ , \tag{1.32}$$

where terms of $\mathcal{O}[(k_0 + k_2)Le^{-(k_0+k_2)L}]$ and higher have been dropped. Here, k_0 and k_2 represent the S- and D-wave binding momenta, respectively (as k_∞ previously represented the separation energy in the case of the deuteron), and the constants a_0 and a_1 are fit parameters.

In general, $E2$ transitions might occur between any states of identical parities whose angular momenta differ by at most two units. Employing the asymptotic form (1.27), we find that the transition between bound states with angular momenta l_1 and l_2 and bound-state momenta k_1 and k_2, respectively, extrapolates as

$$\mathcal{A}_L = \mathcal{A}_\infty + a_0 e^{-2k_< L} \ . \tag{1.33}$$

Here, $k_< \equiv \min(k_1, k_2)$. The general LO formula (1.33) is the main result of this section. One might be surprised that the LO formula (1.33) for $E2$ transitions differs from the LO formula (1.29) for expectation values by the absence of the factor proportional to L^3. Inspection shows that the limit $k_1 \to k_2$ is interesting because terms with prefactors involving $(k_1 - k_2)^{-3}$ become proportional to L^3 in this limit.

Results To test our result (1.32) for $E2$ transitions, we employ a Hamiltonian with a Gaussian well potential

$$V(r) = -V_0 e^{-\left(\frac{r}{R}\right)^2} \ , \tag{1.34}$$

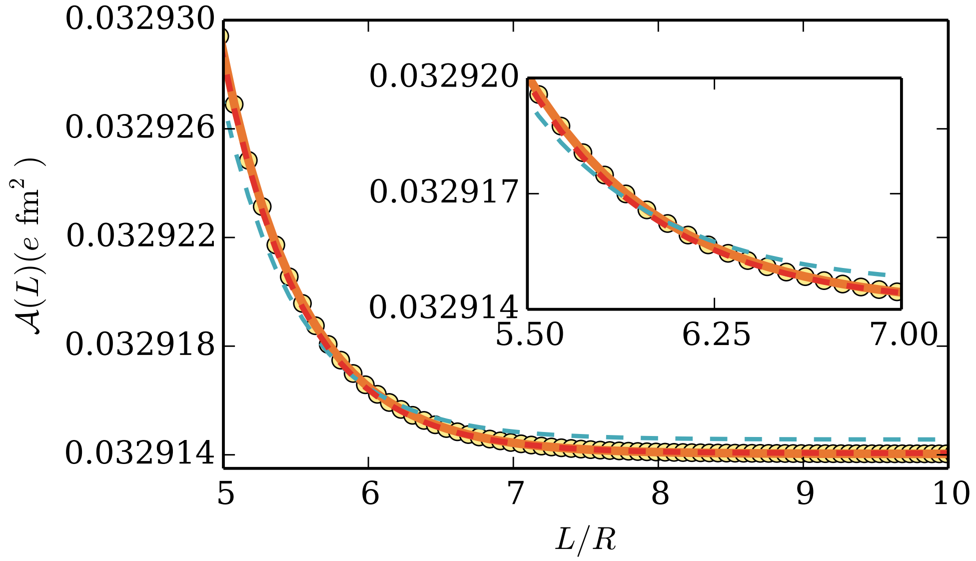

Figure 1.3: Convergence of the $E2$ transition amplitude as a function of L for a simple Gaussian well model. The yellow dots are the results of the numerical calculation. The thin, light blue dashes are the fit to the LO result in Eq. (1.32). The thick, red dashes correspond to a fit including the $(1/k_2L)^2$ term in Eq. (1.32). And the solid orange line includes the $(1/k_2L)^3$ term in the fit.

that is deep enough to contain a bound D-wave state as well as the ground S-wave state. Because $k_2 < k_0$, the dominant correction contains the exponential e^{-2k_2L}. Below, we consider three different orders of the polynomial in k_2L preceding the exponential e^{-2k_2L} that governs the correction term. From Fig. 1.3 we can see that the data is more accurately described as increasing powers of $1/(k_2L)$ are considered. However, over large ranges of k_2L, which we are able to take advantage of in the simple model presented here, the LO result can be sufficient to obtain accurate asymptotic values. Figure 1.3 highlights a small region where the differences in the fitting can be seen.

The log-scale plot, shown in Fig. 1.4, reveals the differences between the fits and, more importantly, the improvement as higher orders of $(1/k_2L)$ are included. Here, we plot the residual transition amplitude, *i.e.* the difference between the values calculated in the truncated basis ($\mathcal{A}_{\text{calculated}}$) and the values reproduced by the fit parameters (A_∞ and c_n). We define

$$\delta\mathcal{A}_m = \frac{\mathcal{A}_{\text{calculated}} - \mathcal{A}_\infty}{\sum_{n=m}^{0} c_n (k_2L)^n} \ , \tag{1.35}$$

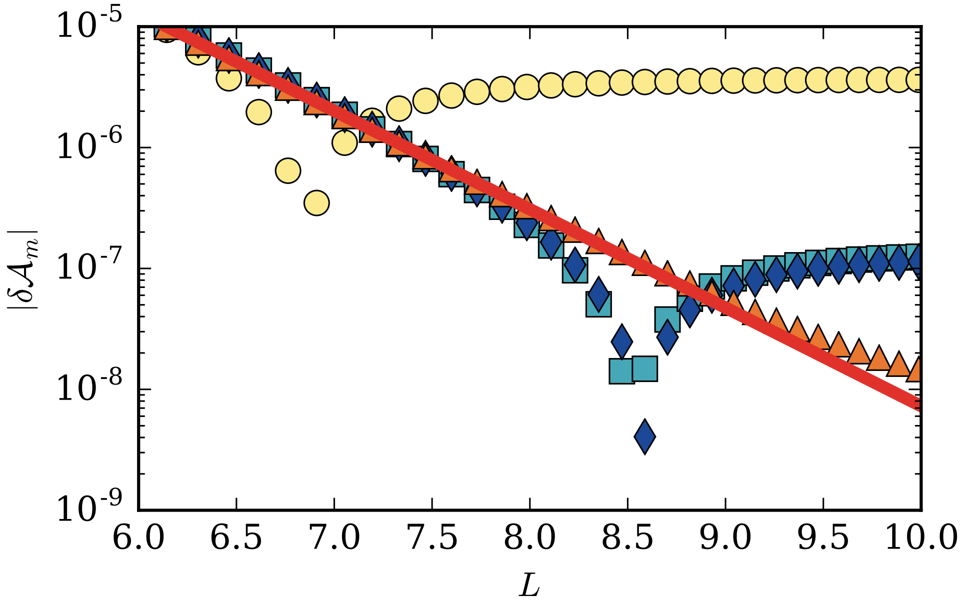

Figure 1.4: The residual transition amplitude from fitting to increasing powers of $(1/k_2L)$ in Eq. (1.32). The yellow dots represent a LO fit ($m = 0$), the light blue squares include also the $(1/k_2L)$ term ($m = -1$), the dark blue diamonds include also the $(1/k_2L)^2$ term ($m = -2$), and the orange triangles include also the $(1/k_2L)^3$ term ($m = -3$). The red, solid line represents e^{-2k_2L} where k_2 is determined from a d-wave energy fit.

where $m < 0$, and we plot the result in Fig. 1.4 as a measure of how well the fit describes the data for different m values. Little improvement comes from the $m = -2$ term due to its small coefficient. Most importantly, we can see that the deviation of the data from the expected behavior happens at larger and larger L values as more terms in the polynomial factor are included.

We note that the sudden drops shown in the Figures 1.2 and 1.4 are the result of the fitting line crossing the original data, implying that the difference changes its sign. As higher-order terms are included in the fit, these dips tend to move to increasing values of L.

1.5 Electromagnetic Multipole Transitions between Bound-States and the Continuum

Derivation We now turn to nucleon capture reactions where we have a transition from a scattering state to a bound state (or vice versa). We assume that the scattering state is obtained in a way that is independent of basis truncation error. However, the bound state is still subject to such errors, and we derive the IR extrapolation for the matrix elements that use this truncated state.

In what follows, we focus on the nucleon-nucleon (NN) processes as examples where the truncation error can be fully understood. This allows us to derive IR extrapolation formulas that have a more general applicability. The generalization to heavier nuclei will be discussed below. We assume that the nuclear interaction vanishes beyond the range R. Thus, at relative distances $r \geq R$ the bound state radial wave function calculated in a truncated basis has the asymptotic form [39]

$$u_L(r) \to A_\infty e^{-\gamma_\infty r}\left[1 - e^{-2\gamma_\infty (L-r)}\right] , \tag{1.36}$$

where $u_L(r) \sim r\mathcal{R}_L(r)$. Here, γ_∞ and A_∞ are, respectively, the binding momentum and the asymptotic normalization coefficient in the infinite volume limit [39]. Equation (1.36) is asymptotically valid for all partial waves. However, its higher order corrections for s-wave are of $\mathcal{O}(e^{-\gamma_\infty(2L+r)})$, much smaller than the $\mathcal{O}(1/(\gamma_\infty r))$ corrections for higher partial waves.

Calculations of capture cross sections in a truncated basis, therefore, effectively involve the radial matrix elements

$$\mathcal{I}_\lambda(k;\eta;L) \equiv \int_0^L \mathrm{d}r\, u_L(r)\, r^\lambda\, u_k(r) \ , \tag{1.37}$$

where k is the momentum of the scattering wave function $u_k(r)$ in the initial state. η is the Sommerfeld parameter and λ defines the multipolarity of the transition. For an electromagnetic capture process, the multipolarity is equal to λ for electric transitions and to $\lambda + 1$ for magnetic transitions. For the weak process, the dominant contribution at low energies comes form $\mathcal{I}_0(k;\eta;L)$.

At $r \geq R$ and $kr \gg \eta$, the radial wave function of the initial state has the form

$$\begin{aligned} u_k(r) \to & \cos\delta_l\, \sin\left[kr - \eta\log(2kr) + \sigma_l - \frac{\pi l}{2}\right] \\ & + \sin\delta_l\, \cos\left[kr - \eta\log(2kr) + \sigma_l - \frac{\pi l}{2}\right] \ , \end{aligned} \tag{1.38}$$

with σ_l being the Coulomb phase shift. For the case of neutron capture, $\sigma_l = 0 = \eta$. Apart from the subleading η dependence, Eq. (1.38) has additional $\mathcal{O}(1/(kr))$ corrections for $l > 0$ even in the absence of Coulomb interaction.

We now derive the IR truncation error, $\Delta\mathcal{I}_\lambda(k;\eta;L)$, in the matrix element $\mathcal{I}_\lambda(k;\eta;L)$ calculated in Hilbert spaces with $L \gg R$. However, in order to use the asymptotically valid approximations for the wave functions given in Eqs. (1.36) and (1.38), we additionally require $kL \gg \eta$ for proton capture and fusion reactions, and $kL \gg l$ for capture in partial waves with orbital angular momentum l.

As previously done with the quadrupole moment, we split the radial integral, Eq. (1.37), into two regions and focus on the region $r \in [R, L]$, which is independent of the details of the nuclear interaction. This integral can be evaluated analytically using Eqs. (1.36) and (1.38) to give

$$\int_R^L \mathrm{d}r\, u_L(r)\, r^\lambda\, u_k(r) = \int_R^\infty \mathrm{d}r\, u_\infty(r)\, r^\lambda\, u_k(r) + 2\,\mathrm{Re}\left[f_\lambda(k;\eta;L)\right] \ , \tag{1.39}$$

where $u_\infty(r)$ is $u_L(r)$ at $L \to \infty$, and

$$\begin{aligned} f_\lambda(k;\eta;L) = \frac{i}{2} A_\infty\, e^{i(\delta_l+\sigma_l-\pi l/2)}\, (2k)^{-i\eta} [&(\gamma_\infty - ik)^{(-\lambda-1+i\eta)} \\ &\times \Gamma(\lambda+1-i\eta, \gamma_\infty L - ikL) - e^{-2\gamma_\infty L}(-\gamma_\infty - ik)^{(-\lambda-1+i\eta)} \\ &\times \Gamma(\lambda+1-i\eta, -\gamma_\infty L - ikL)], \end{aligned} \tag{1.40}$$

is the result of an overlap integral of the asymptotic incoming and outgoing scattering wave function with the finite volume bound state wave function.

Here $\Gamma(c,z)$ is the complex continuation of the incomplete Gamma function. We have dropped terms of $\mathcal{O}(e^{-\gamma_\infty(2L-R)})$ in Eq. (1.39). We express the corrections to the radial integral as

$$\begin{aligned} \Delta\mathcal{I}_\lambda(k;\eta;L) &= \mathcal{I}_\lambda(k;\eta;\infty) - \mathcal{I}_\lambda(k;\eta;L) \\ &= -2\,\mathrm{Re}\left[f_\lambda(k;\eta;L)\right] \ , \end{aligned} \tag{1.41}$$

where

$$\mathcal{I}_\lambda(k;\eta;\infty) = \int_0^\infty \mathrm{d}r\, u_\infty(r)\, r^\lambda\, u_k(r) \tag{1.42}$$

is the radial matrix element $\mathcal{I}_\lambda(k;\eta;L)$ at $L \to \infty$.

In addition to the exponentially suppressed term we explicitly dropped above, we have also neglected the contributions to $\Delta\mathcal{I}_\lambda(k;\eta;L)$ from the higher-order η dependence and higher partial wave corrections to Eqs. (1.36) and (1.38). These terms scale as $\Delta\mathcal{I}_{\lambda-1}(k;\eta;L)$ and are therefore only suppressed by a factor of $1/L$. Using the LO approximation in the asymptotic expansion of the Gamma function,

$$\Gamma(c,z) = z^{c-1}\, e^{-z} \left(1 + \frac{c-1}{z} + \dots\right) \,, \tag{1.43}$$

valid for $|z| \gg 1$ and $|\arg z| < 3\pi/2$, in Eq. (1.40), the IR truncation error in the capture matrix element reduces to a much simpler form,

$$\Delta\mathcal{I}_\lambda(k;\eta;L) = \frac{2A_\infty\gamma_\infty}{\gamma_\infty^2 + k^2} L^\lambda e^{-\gamma_\infty L} \sin\left(\delta_l + \sigma_l - \frac{\pi l}{2} + kL - \eta \log 2kL\right) \,, \tag{1.44}$$

for asymptotically large values of $\gamma_\infty L$. We note that the approximation for $\Gamma(c,z)$ used here in order to arrive at Eq. (1.44) is exact for $\lambda = 0$ neutron capture. However, at larger values of λ and η, this approximation gets worse and it may be necessary to obtain the IR truncation error using Eqs. (1.40) and (1.41) instead.

Eqs. (1.41) and (1.44) hold for heavier nuclei and for all reasonable models of the nuclear Hamiltonian because the single-particle wave functions have the asymptotic forms given in Eqs. (1.36) and (1.38) in the range $R \leq r < L$. They are valid for neutron capture as well as for proton capture unless the energy is low enough to warrant the use of Coulomb wave functions $F_l(kr)$ and $G_l(kr)$ for all $r \lesssim L$ instead of the sine and the cosine functions in Eq. (1.38).

Results For numerical calculations, we use the chiral EFT interaction from Ref. [12]. We obtain the proton-proton (*pp*) and neutron-proton (*np*) scattering states by solving the momentum-space Schrödinger equation. We then calculate the radial matrix elements,

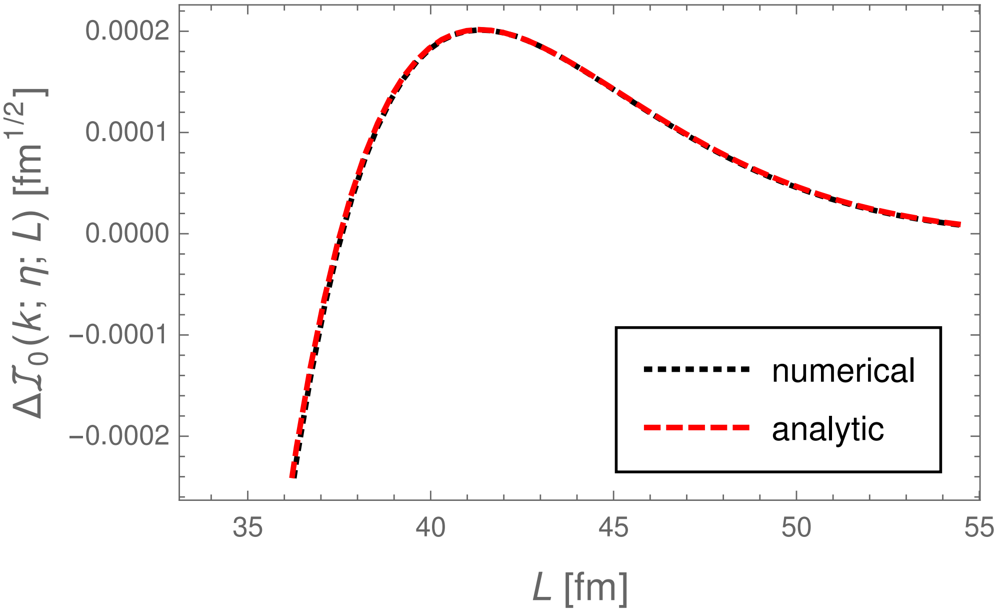

Figure 1.5: Numerical (black, dotted) and analytic (red, dashed) results for the correction $\Delta\mathcal{I}_0(k;\eta;L)$ to the radial overlap between the $^1S_0$ pp scattering wave function at 1 MeV center-of-mass energy and the deuteron s-wave state.

$\mathcal{I}_\lambda(k;\eta;L)$, numerically for a range of L values by expanding the deuteron wave function in HO bases of varying dimensionality.

For the NN processes, it is computationally feasible to calculate $\mathcal{I}_\lambda(k;\eta;L)$ in a large enough basis and obtain an accurate numerical approximation to $\mathcal{I}_\lambda(k;\eta;\infty)$. We begin by comparing the numerical truncation error, $\Delta\mathcal{I}_\lambda(k;\eta;L)$, thus obtained with those predicted by Eq. (1.44).

In Fig. 1.5, we plot $\Delta\mathcal{I}_\lambda(k;\eta;L)$ for pp fusion at 1 MeV center-of-mass energy. Since $\eta = 0.11 \ll 1$ at this energy, we obtain excellent agreement even at smaller L.

Finally, in Fig. 1.6, we plot the IR truncation error in the matrix element of the electric dipole ($E1$) operator between the deuteron s-wave and the np $^3P_1$ wave functions, which contributes to the radiative np capture,

$$n + p \to d + \gamma, \tag{1.45}$$

and its reverse process, deuteron photodisintegration. Here the analytic formula for $\Delta\mathcal{I}_\lambda(k;\eta;L)$ has neglected terms from the $\mathcal{O}(1/(kr))$ corrections to Eq. (1.38). Since these

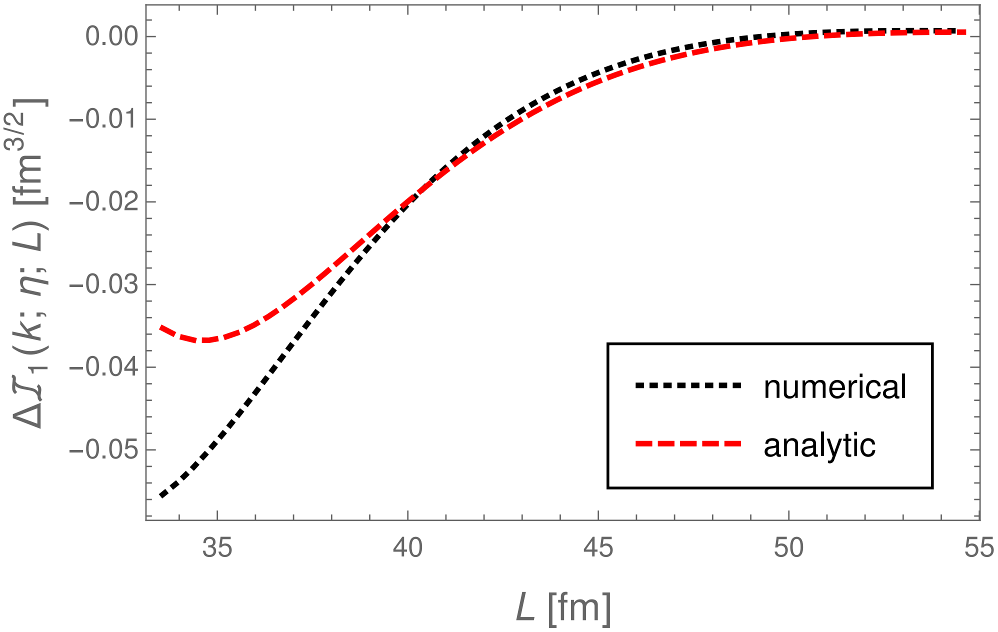

Figure 1.6: Numerical (black, dotted) and analytic (red, dashed) results for the correction $\Delta\mathcal{I}_1(k;\eta;L)$ to the radial matrix element of the $E1$ operator between the np $^3P_1$ scattering wave function at 1 MeV center-of-mass energy and the deuteron s-wave state.

terms are suppressed by a factor of $1/L$, we get a better agreement between the analytic and the numerical results at larger L values.

The analytic results shown above in Fig. 1.5 were not fit to the data. The quantities A_∞, γ_∞, and δ_l were known *a priori* from the wave functions, and the IR truncation error was thus completely predicted by Eq. (1.44). For systems with $A > 2$, however, extracting values for the single-particle separation energies, asymptotic normalization coefficients and phase shifts might not be as straight-forward. Moreover, the use of our analytic results in practical applications is to obtain $\mathcal{I}_\lambda(k;\eta;\infty)$ by extrapolation when the size of the basis is constrained due to unavailability of computational resources. One computes $\mathcal{I}_\lambda(k;\eta;L)$ at several large values of L, and fits Eq. (1.44) [or, if required, Eq. (1.41)] to this data with $\mathcal{I}_\lambda(k;\eta;\infty)$, A_∞, γ_∞, and δ_l treated as fit parameters.

Since Eq. (1.44) is valid at asymptotically large values of L, we obtain better fits when the input data contains larger L values. However, even for smaller L, the extrapolation error is much smaller than the IR truncation error one would make by avoiding extrapolation and simply using $\mathcal{I}_0(k;\eta;L_{\max})$ instead.

Chapter 2

Effective Field Theory

Effective theories have proven to be useful tools for making accurate calculations. They allow us to work with simpler descriptions of nature within a well-defined energy range. With EFT, there is also a well-defined process for adding in corrections to these simplified descriptions and therefore improving the results [33].

One example that illustrates the separation of distance scales is gravitation. The Newtonian gravitational potential energy for a mass m is the presence of the gravitational field due to the presence of mass M is

$$U = -G\frac{Mm}{r} \ , \tag{2.1}$$

where r is the distance between the two bodies and G is the gravitational constant. Let us consider that M is a sphere of radius R and m rests on the surface of M. We could express U as

$$U = -G\frac{Mm}{R+h} \ , \tag{2.2}$$

where h is the small (relative to R) distance above the surface that m can move. If we do an expansion of this equation in h/R, we get

$$\begin{aligned} U =& -G\frac{Mm}{R}\frac{1}{1+h/R} \\ \approx& -G\frac{Mm}{R}\left[1-h/R+(h/R)^2+\mathcal{O}\left((h/R)^3\right)\right] \ . \end{aligned} \tag{2.3}$$

The LO term is a constant, and since what we care about in dynamics is *changes* to U, we can drop it. The next-to-leading-order term can be simplified as

$$U \approx mgh \ , \tag{2.4}$$

where $g = GM/R^2$. We recover what is commonly taught in early physics courses as the gravitational potential energy. And we see that the error in this approximation is estimated by the next term in the expansion at $\mathcal{O}\left((h/R)^2\right)$. This gives 1% accuracy for values of h up to about 60km, quite reasonable for the kinematics typically explored in early physics classes.

An example from quantum field theory that illustrates the usefulness of the separation of scales, this time in momentum space, is the Fermi theory of the weak interaction. At low energies, the propagator for the W boson

$$\frac{1}{q^2 - M_W^2} \ , \tag{2.5}$$

can be expanded in q/M_W

$$(1/M_W^2)\left[1 + (q/M_W)^2 + \mathcal{O}\left((q/M_W)^4\right)\right] \ , \tag{2.6}$$

where q is the incoming momentum and M_W is the mass of the W boson. The LO term, $(1/M_W^2)$, translates to a contact interaction, the same type of interaction proposed by Fermi to explain β decay. The large mass of the W boson makes the interaction necessarily short-ranged. In fact, at low energies, it is indistinguishable from a contact interaction. The interaction's LO position in the low-energy q/M_W expansion accounts for Fermi's success in applying it.

We aim to develop such an effective theory for systems that are characterized by a short-range interaction and a long-range $1/r^\alpha$ ($\alpha > 2$) tail. For example, the strength of the potential

$$\frac{-C_6}{r^6} \ , \tag{2.7}$$

is defined by the C_6 coefficient. This coefficient can be translated to a length

$$\beta_6 = \left(\frac{2\mu C_6}{\hbar^2} \right)^{1/4} \quad , \tag{2.8}$$

where μ is the reduced mass of the 2-body system. For systems where this length is much greater than the length scale (R) of the more complicated short-range physics, we ought to be able to establish an expansion for observable quantities in terms of R/β_6. Such an expansion exploits the separation of scales between R and β_6.

Effectively, the short-range interactions are replaced by a contact interaction ($\delta(\vec{r}-\vec{r}')$ in coordinate space). Higher-order corrections to this assumption are associated with increasing powers of R/β_6.

To accurately describe van der Waals physics with an EFT, we need to deal with the singularity of (2.7) and be able to renormalize. Our first efforts are discussed below.

Chapter 3

Inverse Cube Potential

This section describes our study the regularization and renormalization of a finite range inverse cube (FRIC) potential in the two- and three-body sectors. The majority of the content presented here has been submitted to Physical Review C for publication [44]. Specifically, we compare and contrast three different regularization schemes frequently used to study few-body systems as well as the associated renormalization group (RG) flows. We also calculate bound state and scattering observables over a wide range of cutoffs, demonstrating the sufficiency of a two-body contact interaction to renormalize two- and three-body observables. We supplement these plots with quantified analyses of the observables' residual cutoff dependence.

3.1 Introduction

Effective field theories (EFTs) have become a standard tool in nuclear few-body physics to construct the interactions between the considered degrees of freedom [13, 31]. For example, chiral effective theory is a low-energy expansion of the nucleon-nucleon (NN) interaction that employs only nucleons and pions as degrees of freedom and that uses the pion mass m_π (or a small momentum) over a large scale Λ that can be associated with the lightest degree of freedom not included in the EFT (e.g. the ρ-meson)[37]. This framework is then used to derive the nuclear Hamiltonian in a systematic low-energy expansion. The resulting potential has been used extensively in few-nucleon studies and ab initio nuclear structure calculations.

It was pointed out that the most singular piece of the one-pion exchange in the deuteron channel is an inverse cube potential [53, 48]. The renormalization of this leading order (LO) potential has been studied repeatedly in the two- and three-nucleon sector [47, 43, 7, 35, 52]. Here, we intend to study the renormalization of the inverse cube potential in the much simpler three-boson system thereby removing the complications due to the spin-dependent tensor force. In particular, we will study whether the three-body system with pairwise inverse cube interactions requires a three-body counterterm for renormalization, and whether residual cutoff corrections can be used as a reliable tool to build a power counting scheme as suggested in Ref. [29]. We note that there is also interest in atomic physics regarding the inverse cube interaction, however, most attention has been focused on the low-energy properties in the *infinite* range limit [40, 23] as opposed to the case we study here where the mass of the exchanged pion limits the range of the inverse cube potential.

Since the residual cutoff dependence to some extent can be influenced by the chosen regularization scheme, we will carry out this analysis for various schemes that are currently used by the community. Specifically, we will consider a *local* regularization scheme [25] that cuts off the potential in coordinate space at a small distance R, a non-local regularization scheme [13] that cuts off the high momenta in the momentum space form of the two-body interaction $V(p, p')$ separately, and a semi-local regularization scheme [14] that applies these strategies separately to the long-range inverse cube part of the interaction and the short-distance regulator.

These different regularization schemes have different advantages for different methods that are used to diagonalize the nuclear Hamiltonian. For example, local interactions are commonly used in quantum Monte Carlo calculations, though progress has been made including nonlocal interactions (e.g. [51, 36]). However, while these have been used extensively in the literature, a detailed comparison of these approaches is missing.

We find that the regularization schemes analyzed can be used to obtain regulator-independent results. We find however that the regulator dependence of the short-distance counterterm is different for the regulation schemes we apply. In agreement with findings in the three-nucleon sector[43, 52], we find that three-body observables are completely renormalized without the inclusion of an additional three-body counterterm. However, an analysis of the cutoff dependence of three-body observables shows also that observables converge more slowly than expected from previous studies of the three-nucleon sector [52].

In Sec. 3.2, we will discuss the regularization schemes, the renormalization and calculation of observables. In Sec. 3.3, we will present the results obtained for the two- and three-boson system as well as quantitative analyses of the remaining cutoff corrections. We conclude with a summary and an outlook.

3.2 Theory

In the following subsections, we describe the interaction that is used in this work, how it is regulated, and how it is renormalized. We comment also briefly on technical details such as the normalization of states and the calculation of observables through the Schrödinger, Lippmann-Schwinger, and Faddeev equations.

The starting point of our calculations is most generally a *local* interaction. A local interaction is diagonal in coordinate space such that

$$\langle \vec{r}\,'|V|\vec{r}\rangle = \delta(\vec{r}\,' - \vec{r})V(\vec{r}) \ . \tag{3.1}$$

These interactions appear frequently in nuclear and atomic systems, and they allow for a clear interpretation of the relevant scales of the physics involved. The non-regulated, singular potential $V_{\mathrm{S}}(r)$ that we will consider is a FRIC potential of the form

$$V_{\mathrm{S}}(r) = -C_3 \frac{e^{-m_\pi r}}{r^3} \ . \tag{3.2}$$

We choose $m_\pi = 138$ MeV and $C_3 = 0.8\ \mathrm{fm}^2$ such that a deuteron-like state ($B_2 = 2.2$ MeV) exists when we regulate the potential at ~ 1 fm. This potential has to be regulated at short distances and observables will depend strongly on the regularization scale as the interaction is too singular [17]. Below we will display how a (*smeared out*) short-distance counterterm can be introduced to address this problem.

We perform our calculations in momentum space, and we Fourier transform the interaction V and carry out a partial-wave projection

$$\tilde{V}_l(p,k) \equiv FT\left[V(r)\right] = \frac{2}{\pi}\int_0^\infty dr r^2 j_l(pr)V(r)j_l(kr) \ , \tag{3.3}$$

where $j_l(z)$ are the spherical Bessel functions of order l.

3.2.1 Regulator Formulations

Local Regulation

For a local, singular potential, $V_S(r)$, we have implemented three different forms of regulation: local, semi-local, and nonlocal. The locally regulated potential has the form

$$V(r) = \rho(r;R)V_S(r) + g(R)\chi(r;R) \ , \tag{3.4}$$

where $\rho(r;R)$ is an arbitrary function that overcomes $V_S(r)$ in the $r \to 0$ limit such that the product $\rho(r;R)V_S(r)$ is finite. For the locally regulated case we use

$$\rho(r;R) = \left(1 - e^{-(r/R)^2}\right)^4 \ , \tag{3.5}$$

where R is the range at which the characteristic behavior of $V_S(r)$ is cut off. The powers were chosen to match the semi-locally regulated case where some care had to be taken in the selection (see Appendix A). The counterterm

$$g(R)\chi(r;R) \ , \tag{3.6}$$

has two components. The first, $g(R)$ is an R-dependent coupling strength. We tune this parameter to match some low-energy, two-body observable such as the two-body binding energy. The second, $\chi(r;R)$, is a contact-like interaction or a *smeared* δ function such that

$$\lim_{R\to 0} \chi(r;R) \sim \delta(r) \ . \tag{3.7}$$

For the locally regulated case we use

$$\chi(r;R) = e^{-(r/R)^3} \ . \tag{3.8}$$

The power of r/R in the exponential is chosen to match the divergence of the long-range potential so that the range below which the inverse cube potential is not considered corresponds well with the range beyond which the short-distance counterterm does not act. We will discuss below that the RG flow of the locally-regulated counterterm strength, $g(R)$, contains multiple branches [4]. To ensure consistency between our results and others', we have also implemented a semi-local regulation scheme.

Semi-Local Regulation

The difference between local regulation and semi-local regulation lies in the definition of the counterterm. In Eq. (3.4) we defined the counterterm in coordinate space. This counterterm, that regulates the relative distance in the two-body system and thereby the momentum exchange, has multiple solutions (provided the short-distance cutoff is small enough) for which the two-body binding energy B_2 is reproduced.

If we instead define the counterterm in momentum space as

$$g(R)\tilde{\chi}(p;R)\tilde{\chi}(k;R) \ , \tag{3.9}$$

such that, by itself, only permits one state, we obtain a unique RG flow. The full potential in momentum space is then

$$\tilde{V}(p,k) = FT\left[\rho(r;R)V_S(r)\right] + g(R)\tilde{\chi}(p;R)\tilde{\chi}(k;R) \ , \tag{3.10}$$

where FT represents the Fourier transform and partial-wave projection shown in Eq. (3.3).

For the semi-locally regulated case, similar to [14], we use

$$\rho(r;R) = \left[1 - e^{-(r/R)^2}\right]^4 \ , \tag{3.11}$$

and

$$\tilde{\chi}(p;R) = e^{-(pR/2)^2} = e^{-(p/\Lambda)^2} \ , \tag{3.12}$$

where $\Lambda \equiv 2/R$. For a brief discussion on the different $\rho(r;R)$ functions used for the locally and semi-locally regulated cases, see Appendix A.

Nonlocal Regulation

For the fully nonlocal interaction, we take the semi-local interaction Eq. (3.10), including the forms of $\rho(r;R)$ and $\tilde{\chi}(p;R)$, and modify the first term as follows

$$\tilde{V}(p,k) = \tilde{\chi}(p;R) FT\left[\rho(r;R_<)V_S(r)\right]\tilde{\chi}(k;R) + g(R)\tilde{\chi}(p;R)\tilde{\chi}(k;R) \ . \tag{3.13}$$

The momentum-space regulators multiplying the first term suppress the diagonal matrix elements where the incoming and outgoing momenta are large but similar, removing some sensitivity to the choice of $\rho(r;R)$ that we discuss in A. The short-distance cutoff used before we take the Fourier transform, $R_<$, is chosen to be much less than R. This allows us to ensure that the resulting cutoff dependence in the observables is attributable to the regulator function, $\tilde{\chi}(p;R)$, rather than the Fourier transform.

3.2.2 Two-Body Bound States

We calculate two-body binding energies by solving the Schrödinger equation

$$(\hat{H}_0 + \hat{V})\,|\psi\rangle = E\,|\psi\rangle \ \ , \tag{3.14}$$

in coordinate and momentum space. $\hat{H}_0 = \hat{p}^2/m$ is the kinetic energy operator, $\hat{V}$ is the interaction, $|\psi\rangle$ is the state representing the system, and E is the total energy of the system. In coordinate space, we tune the counterterm such that for a desired value E, the radial equation

$$-\frac{1}{m}\frac{d^2u}{dr^2} + V(r)u(r) = E\,u(r) \ , \tag{3.15}$$

is solved where $u(r) \equiv rR_0(r)$. We have dismissed the centrifugal term as only s-waves are considered. We rearrange Eq. (3.14) such that we have

$$\hat{G}_0(E)\hat{V}\,|\psi\rangle = |\psi\rangle \ , \tag{3.16}$$

where $G_0(z) \equiv 1/(z - \hat{H}_0)$. After discretization with the basis states $|p_i\rangle$, Eq. (3.16) becomes an eigenvalue problem that is easily solved by finding the energies that fulfill

$$\det\left[\hat{1} - K_{ij}(E)\right] = 0 \ , \tag{3.17}$$

where $K_{ij}(E) = \langle p_i|\hat{G}_0(E)\hat{V}|p_j\rangle$ and we tune the counterterm such that the requirement Eq. (3.17) is satisfied.

3.2.3 Lippmann-Schwinger Equation

To obtain two-body phase shifts, we calculate the two-body t-matrix defined as

$$\hat{t} = \hat{V} + \hat{V}\hat{G}\hat{V} \ , \tag{3.18}$$

where

$$\hat{G} = \hat{G}(z) \equiv \left(z - \hat{H}\right)^{-1} \ ,$$

is the Green's operator for the full Hamiltonian

$$\hat{H} = \hat{H}_0 + \hat{V} \ .$$

The Green's operator corresponding to the free Hamiltonian, $\hat{H}_0$ is defined by

$$\hat{G}_0 \equiv \left(z - \hat{H}_0\right)^{-1} \ .$$

We can relate $\hat{G}$ to $\hat{G}_0$ by the operator identity

$$\hat{A}^{-1} = \hat{B}^{-1} + \hat{B}^{-1}(\hat{B} - \hat{A})\hat{A}^{-1} \ ,$$

such that

$$\hat{G} = \hat{G}_0 + \hat{G}_0 \hat{V} \hat{G} \ .$$

Multiplying Eq. 3.18 by $\hat{G}_0$ from the left, we have

$$\begin{aligned} \hat{G}_0 \hat{t} &= \hat{G}_0 \hat{V} + \hat{G}_0 \hat{V} \hat{G} \hat{V} \ , \\ \hat{G}_0 \hat{t} &= \left[\hat{G}_0 + \hat{G}_0 \hat{V} \hat{G} \right] \hat{V} \ , \\ \hat{G}_0 \hat{t} &= \hat{G} \hat{V} \ . \end{aligned} \tag{3.19}$$

Inserting the last line of Eq. 3.19 into Eq. 3.18, we get the Lippmann-Schwinger equation in operator form

$$\hat{t} = \hat{V} + \hat{V} \hat{G}_0 \hat{t} \ . \tag{3.20}$$

In the partial-wave projected momentum basis, considering bosons interacting in s-waves only, we have

$$\begin{aligned} \langle p \,| \hat{t} | p' \rangle &= \langle p \,| \hat{V} | p' \rangle + \langle p \,| \hat{V} \, \hat{G}_0(E + i\epsilon) \, t | p' \rangle \ , \\ t(p, p'; E) &= \tilde{V}(p, p') + \int_0^\infty dq \, q^2 \, \frac{\tilde{V}(p, q) \, t(q, p'; E)}{E + i\epsilon - q^2/m} \end{aligned} \tag{3.21}$$

where m is the nucleon mass and $\epsilon \to +0$. From the on-shell matrix element $t(p, p; E = p^2/m)$ we extract the phase shift via

$$t(p, p; E = p^2/m) = -\frac{2}{m\pi} \frac{1}{p \cot \delta - ip} \ . \tag{3.22}$$

The scattering length is defined by the effective range expansion

$$p \cot \delta \approx = -\frac{1}{a} + \frac{r_s}{2} p^2 \ , \tag{3.23}$$

which allows us to calculate it exactly from the on-shell t-matrix amplitude at $p = 0$.

$$a = \frac{m\pi}{2} t(0, 0; 0) \ . \tag{3.24}$$

3.2.4 Three-Body Bound States

To calculate three-body binding energies, we start with the equation for a single Faddeev component of a system containing three identical particles

$$|\psi\rangle = \hat{G}_0(E)\hat{t}\hat{P}\,|\psi\rangle \ , \tag{3.25}$$

where

$$\hat{P} = \hat{P}_{12}\hat{P}_{23} + \hat{P}_{13}\hat{P}_{23} \ , \tag{3.26}$$

is the permutation operator with $\hat{P}_{ij}$ interchanging particles i and j [28]. After projecting onto the partial-wave, momentum basis for three identical bosons described by two Jacobi momenta p (the relative momentum between particles 1 and 2) and q (the relative momentum between particle 3 and the center of mass of the 1–2 subsystem), we discretize the equation and solve for the bound state energy E using the same techniques as in the two-body case, as long as E remains below the deepest state in the two-body spectrum. However, this limitation is in conflict with our goal of studying the cutoff dependence of two- and three-body observables. As we go to higher momentum-space cutoffs (smaller R values), spurious bound states enter the two-body spectrum. Three-body states quickly become resonances in this regime, bounded above and below by two-body bound states. There are two ways that we deal with this.

The first method follows [43] and is repeated here. It involves *removing* the spurious two-body state from the spectrum by transforming the potential

$$\hat{V} \to \hat{V} + |\phi\rangle\,\lambda\,\langle\phi| \ , \tag{3.27}$$

which takes the eigenvalue of the state ϕ and modifies it by an amount λ. Using this transformed potential in the Lippmann-Schwinger equation and taking the limit of $\lambda \to \infty$ (removing the state from the spectrum), we have

$$\lim_{\lambda\to\infty} \hat{t}(\lambda) = \hat{t} - |\eta\rangle\,\frac{1}{\langle\phi|\hat{G}_0|\eta\rangle}\,\langle\eta| \ , \tag{3.28}$$

as our modified t-matrix where

$$|\eta\rangle = |\phi\rangle + \hat{t}\hat{G}_0 \, |\phi\rangle \ . \tag{3.29}$$

This only requires that we have the wave function $\langle p|\phi\rangle$ to calculate the modified t-matrix where that state no longer contributes a pole. In practical calculations using a large, finite λ value in (3.27) is sufficient. If there are several spurious two-body states, the procedure is repeated for each of them.

The second method we employ to study the cutoff dependence of three-body resonances is to look for the resonances in the three-body phase shifts.

3.2.5 Three-Body Phase Shifts

In the cutoff regime where spurious two-body bound states exist, we can scatter a third particle off the spurious deep two-body state and scan the phase shifts in the energy range between the two-body states for a resonance. To do this, we calculate the three-body T-matrix using [27]

$$\hat{T} = \hat{t}\hat{P} + \hat{t}\hat{G}_0\hat{P}\hat{T} \ , \tag{3.30}$$

which relates to the elastic scattering operator U by

$$\hat{U} = \hat{P}\hat{G}_0^{-1} + \hat{P}\hat{T} \ . \tag{3.31}$$

In the partial-wave-projected, momentum basis, considering bosons interacting only via s-waves, we have

$$\begin{aligned}\langle pq|\hat{T}|\phi\rangle &= \langle pq|\hat{t}\hat{P}|\phi\rangle + \\ &\int_0^\infty dq'(q')^2 \int_{-1}^{1} dx \, \frac{t(p,\pi_1,E-3q^2/4m)\,G(q,q',x)}{E+i\epsilon-q^2/m-(q')^2/m-qq'x/m} \, \langle \pi_2 q'|\hat{T}|\phi\rangle \ ,\end{aligned} \tag{3.32}$$

where the incoming state $|\phi\rangle = |\varphi k\rangle$ contains the wave function $\varphi(p)$ of the two-body bound state and the relative momentum k between the third particle and the center of mass of the two-body subsystem, $G(q, q', x)$ is a geometrical factor introduced by the permutation operator, $\pi_1 = \sqrt{q^2/4 + (q')^2 + qq'x}$, and $\pi_2 = \sqrt{q^2 + (q')^2/4 + qq'x}$.

The elastic scattering amplitude M is related to the U operator by

$$M = -\frac{2m\pi}{3} \langle \phi | \hat{U} | \phi \rangle \ , \tag{3.33}$$

and the atom-dimer phase shift by

$$M = \frac{1}{k \cot \delta - ik} \ . \tag{3.34}$$

In the three-body sector, we have a similar effective range expansion

$$k \cot \delta \approx -\frac{1}{a_{AD}} + \frac{r_{s,AD}}{2} k^2 \ , \tag{3.35}$$

which defines the atom-dimer scattering length a_{AD} and atom-dimer effective range $r_{s,AD}$.

3.2.6 Quantitative Uncertainty Analysis

To analyze the uncertainties induced by short-distance physics of our regularization procedure, we study in this section the regulator dependence of observables. Similar to the analysis done by Song *et al.* [52], our uncertainty analysis is based on a simple power series expansion of observables quantities $\mathcal{O}$ of the form

$$\mathcal{O}(\Lambda) \approx \mathcal{O}_\infty \left[1 + \sum_i^\infty c_i \left(\frac{q}{\Lambda} \right)^i \right] \ , \tag{3.36}$$

where q is associated with the low-momentum scale relevant to the calculation; however, i is *not* assumed to be an integer. For the purposes of this project, we truncate the summation over i after the first term $i = n$, leaving

$$\mathcal{O}(\Lambda) \approx \mathcal{O}_\infty \left[1 + c_n \left(\frac{q}{\Lambda} \right)^n \right] \ , \tag{3.37}$$

We seek to establish the value of n. In Ref. [52], n was found by fitting the first few terms in the above expansion with integer n to the cutoff dependence of observables. Here, we will study the cutoff dependence at very large cutoffs, focus on the dominant term in the expansion, and fit n itself to data and allow for non-integer values.

To extract the power of the leading cutoff correction, we examine both the Λ and the q dependence. The first approach we take to investigate the Λ dependence is to calculate observable $\mathcal{O}$ over a range of Λ values, and fit the results to Eq. (3.37) for a range of n values. For each n, we evaluate a penalty function that we define as

$$p_n = \sum_i \left(\frac{\mathcal{O}_{calc}(\Lambda_i) - \mathcal{O}_{fit}(\Lambda_i)}{\mathcal{O}_{calc}(\Lambda_i)} \right)^2 , \tag{3.38}$$

where $\mathcal{O}_{calc}(\Lambda)$ is the observable calculated for a specific value of Λ and $\mathcal{O}_{fit}(\Lambda)$ is the value of the observable as it is "reproduced" by Eq. (3.37) and the fit parameters $\mathcal{O}_\infty$ and c_n. Once we have p_n for a range of n values, we search for a minimum p_n where n is optimal.

Another way to isolate the Λ dependence is to extract $\mathcal{O}_\infty$ from a fit to Eq. (3.37) and construct the quantity

$$\frac{\mathcal{O}(\Lambda) - \mathcal{O}_\infty}{\mathcal{O}_\infty} = \sum_i c_i \left(\frac{q}{\Lambda}\right)^i , \tag{3.39}$$

such that truncating the sum after the first term leaves

$$\frac{\mathcal{O}(\Lambda) - \mathcal{O}_\infty}{\mathcal{O}_\infty} \approx c_n \left(\frac{q}{\Lambda}\right)^n . \tag{3.40}$$

Now our task is to determine n. Taking the logarithm of both sides, we have

$$\ln \frac{\mathcal{O}(\Lambda) - \mathcal{O}_\infty}{\mathcal{O}_\infty} \approx \ln \left[c_n \left(\frac{q}{\Lambda}\right)^n \right] . \tag{3.41}$$

Finally, we expose $\ln \Lambda$ by itself, leaving

$$\ln \frac{\mathcal{O}(\Lambda) - \mathcal{O}_\infty}{\mathcal{O}_\infty} \approx -n \ln \Lambda + b , \tag{3.42}$$

where b is an intercept that we fit. Plotting the residual uncertainties as a function of $\ln \Lambda$, we ought to be able to extract the slope n, or at least some upper limit on it.

Grießhammer has argued [29] that the q dependence of observables provides a necessary though insufficient window into the order of cutoff-dependent corrections. To isolate the q dependence, we have to restrict the observables we study to those whose q dependence is well understood. Doing so allows us to calculate the observable at two different cutoffs and study the relative difference

$$\frac{\mathcal{O}(\Lambda_2) - \mathcal{O}(\Lambda_1)}{\mathcal{O}_\infty} \approx q^n c_n \left[\frac{1}{\Lambda_2^n} - \frac{1}{\Lambda_1^n} \right] . \tag{3.43}$$

Taking the logarithm, we get

$$\ln \left[\frac{\mathcal{O}(\Lambda_2) - \mathcal{O}(\Lambda_1)}{\mathcal{O}_\infty} \right] = n \ln q + b , \tag{3.44}$$

where b, again, is an intercept that we fit. As in Eq. (3.42), n corresponds to the slope.

3.3 Results

3.3.1 Renormalization Group Flow

The first aspect of the regulation schemes we compare is the running of the counterterm constants, the RG flow. We choose to fix the shallowest two-body state at $B_2 = 2.2$ MeV. Figure 3.1 shows the stark difference between the RG flow found using a local counterterm and the RG flows found with nonlocal counterterms. The main difference is the issue of uniqueness. For the locally regulated potential, as pointed out by [4], $g(R)$ has multiple solutions that give a two-body bound state at the desired binding energy. There is one branch where there exists one state in the two-body system. Each branch below that branch contains successively one additional state. The RG flow shown for the locally regulated interaction connects four of those branches, "hopping" downward when it is easier to add an additional state than to continue to maintain the shallowness of the fixed state. Only two of the "hops" are visible in the plot due to the scale and the relative difference between the magnitudes of g between the different branches. Note also the difference in the units of

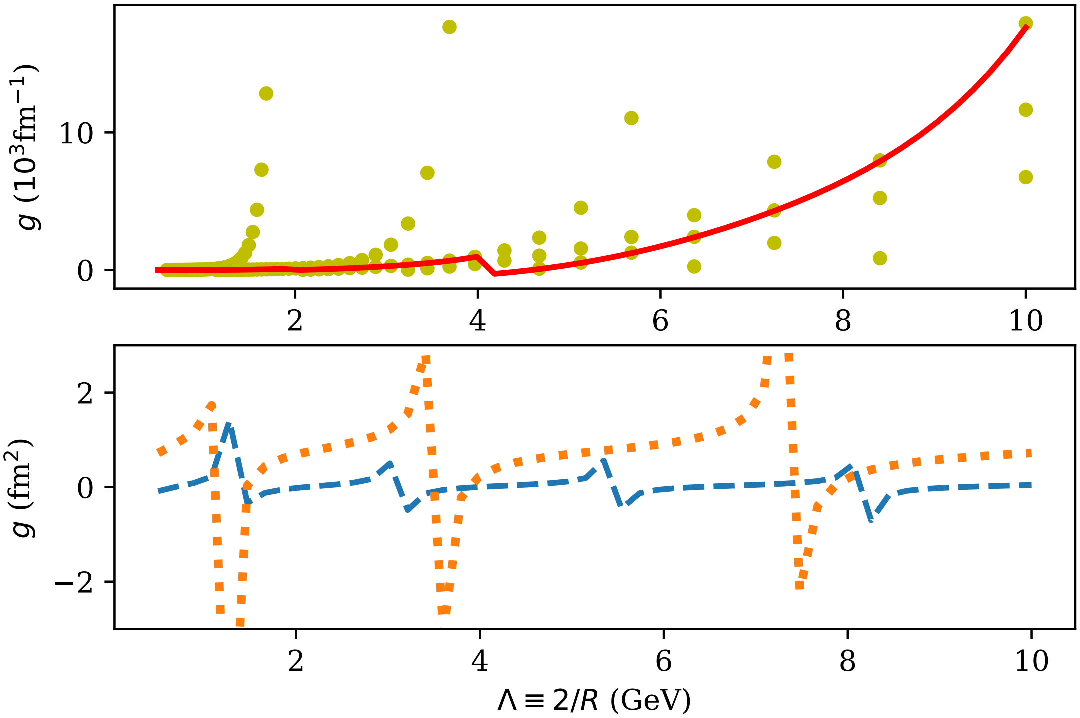

Figure 3.1: RG flows of the counterterm coupling g. The yellow circles in the upper plot represent $g(R)$ values calculated with a local regulator and local counterterm. The red, solid line in the upper plot are the $g(R)$ values used to calculate the phase shifts in Fig. 3.2. The blue, dashed line in the lower plot corresponds to the semi-locally regulated interaction. The orange, dashed line corresponds to the nonlocally regulated interaction.

the upper and lowers plots if Fig. 3.1. There is a factor of R^3 that comes from the Fourier transform and partial-wave projection of $\chi(r; R)$.

The other two functions shown in the lower plot of Fig. 3.1 are qualitatively very similar. They correspond to the semi-local and nonlocal regulation schemes. While the same $\rho(r; R)$ is used in both, the prescription is somewhat different as one can see from Eq. (3.10) and Eq. (3.13). The semi-local regulation scheme brings in spurious bound states faster than the nonlocal regulation scheme, but as mentioned before, nonlocal regulation cuts off the potential at large incoming and outgoing momenta, suppressing high-momentum contributions. Still, they are very similar interactions, thus they provide very similar RG flows.

3.3.2 Two-Body Scattering

As the different regulation schemes are tuned to reproduce the same shallow state at $B_2 = 2.2$ MeV, we expect that differences in low-energy scattering observables are highly suppressed when large cutoffs are employed. We calculate the phase shifts using all three regulation schemes and show the results in Fig. 3.2. The left plot contains the phase shifts of an non-renormalized, nonlocally regulated potential with $g(R) = 0$, demonstrating the strong cutoff dependence of low-energy observables and the need for a counterterm. The most important feature of the right plot is the agreement between the different regulation schemes. It is also worth mentioning the Λ value at which the phase shifts begin to converge (≈ 2 GeV). Studies of the one-pion-exchange potential [52, 43] share a similar scale. This is consistent with the known result that the one-pion-exchange potential goes like an inverse cube potential at short distances (high cutoffs) [53, 48]. Coupled with our chosen C_3 value, we expect similar renormalization behavior.

It is clear from Fig. 3.2 that a two-body contact interaction is sufficient to renormalize the two-body phase shifts. The corresponding result for the two-body scattering length is shown in Fig. 3.3.

One of the advertised, key advantages of EFT is quantifiable uncertainty which in turn requires a power counting that orders contributions in the Hamiltonian according to their importance. These uncertainties have usually two sources: (i) the truncation of the low-energy expansion and (ii) uncertainties that are introduced when low-energy counterterms are fitted to data. Here we focus on the first source of uncertainties and some information on this truncation error is contained in the convergence behavior of observables as the short-distance cutoff is increased. To study this problem, we first choose a range of cutoffs over which to fit the scattering length to Eq. (3.37). As we fix the bound state, we assume $q = \gamma \equiv mB_2$ in the fit. Then we assume a number of n values and evaluate Eq. (3.38) for each one. The results are shown in Fig. 3.4. Of course, we want to know how robust this procedure is. To establish that, we repeat the procedure for different *windows* of cutoffs. The results are shown in Fig. 3.4. In the left-hand plot of 3.4, we show the penalty function Eq. (3.38) as it depends on the n used in the fit to Eq. (3.37). We performed this fit over range

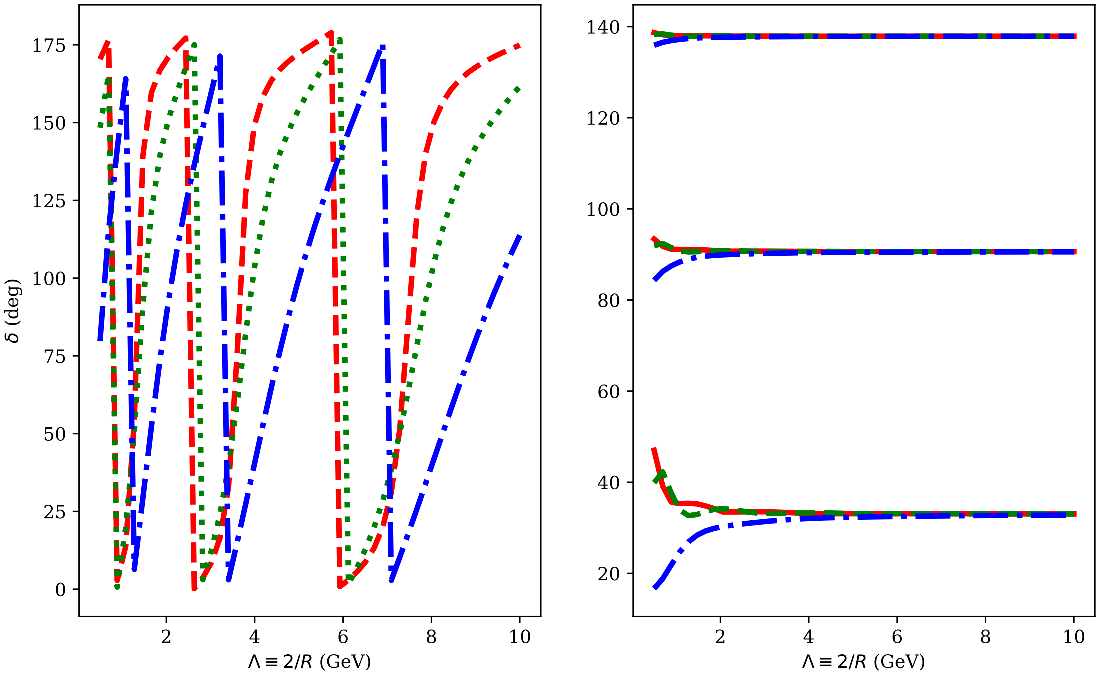

Figure 3.2: [Left] Cutoff dependence of the s-wave phase shifts at $E = 1$ (red, dashed), 10 (green, dotted), and 100 MeV (blue, dot-dashed) calculated via a nonlocally regulated potential without a counterterm. [Right] Cutoff dependence of the s-wave phase shifts at (from top to bottom) $E = 1$, 10, and 100 MeV in the center-of-mass frame. The solid, red lines are the phase shifts calculated from a locally regulated potential. The green, dashed lines are the phase shifts at the same energies calculated with a semi-locally regulated interaction. The blue, dot-dashed lines are the phase shifts using a nonlocally regulated interaction. All three schemes include a contact-like counterterm.

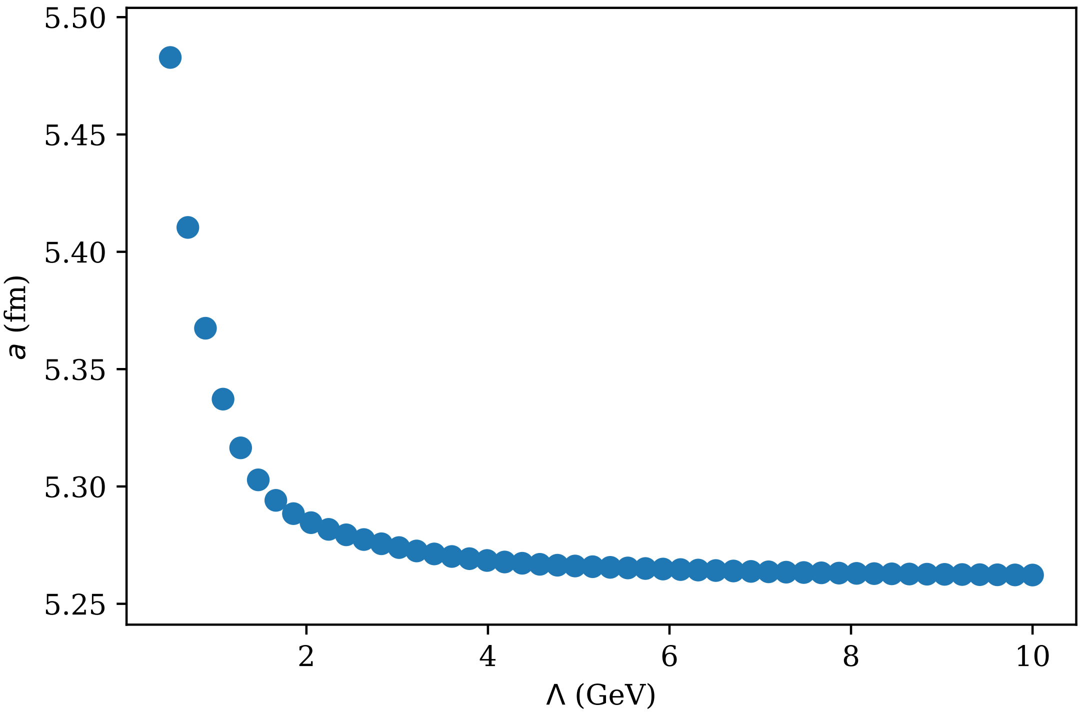

Figure 3.3: The scattering length is shown as a function of the high-momentum (short-distance) cutoff. The blue circles are the numerical results.

$[\Lambda_{\text{min}}, \Lambda_{\text{max}}]$ with $\Lambda_{\text{max}} = 10$ GeV. Each line corresponds to a different Λ_{min}. Our expectation was that as the range of Λ shrinks to include exclusively higher and higher values, the value of n would converge. However, it is easy to see that n is sensitive to the range of cutoffs over which $a(\Lambda)$ is fit. Second, above ≈ 4 GeV, the minimum p_n moves to higher and higher n values. The coefficients, c_n, at these higher values of n grow unnaturally large, clouding the reliability with which we can relate n to the LO correction. As the results of fitting $a(\Lambda)$ to Eq. (3.37) are somewhat inconclusive, we turn to our second method of extracting the power of the LO corrections — fitting to Eq. (3.43). Fig. 3.5 shows the results of calculating the two-body phase shifts and cross sections at two different cutoffs, $\Lambda_1 = 2439$ MeV and $\Lambda_2 = 6316$ MeV. The fit of the phase shifts is performed over a small region of k above γ. The region is chosen to be relatively small to ensure that the slope is not affected by the unfortunate zero that occurs just above 2 fm^{-1}. Momenta below γ are ignored to ensure that the low-momentum scale most relevant to the calculation is, in fact, k. The slope of the fit line is ≈ 1.4. As Grießhammer explains in [29], the slope from these corrections is an upper

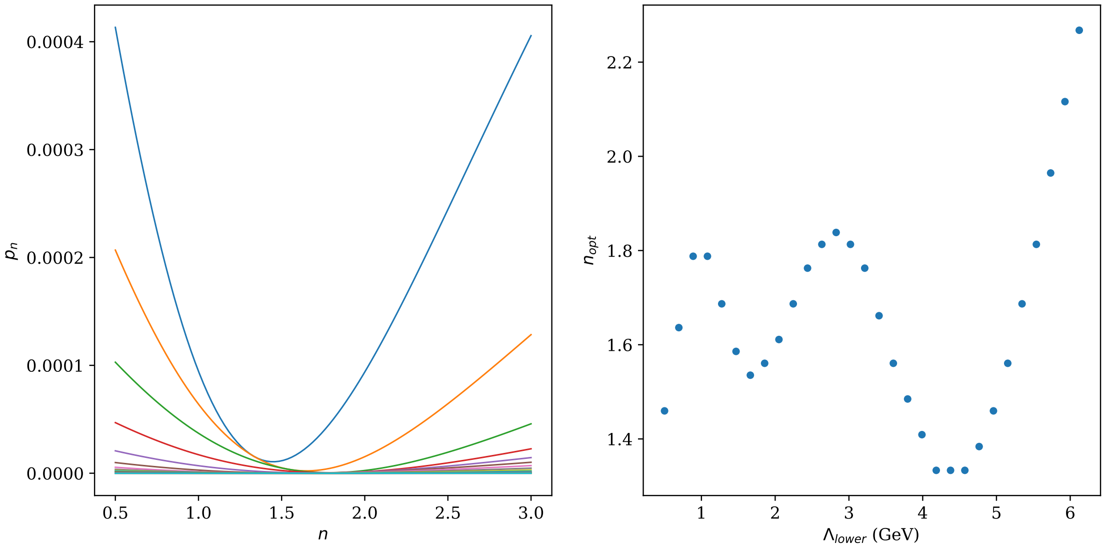

Figure 3.4: [Left] The penalty function as a function of the power, n, used to fit the two-body scattering length to Eq. (3.37). Different lines correspond to different lower bounds, Λ_{min}, used to perform the fit. The correspondence between the lines and the specific value of Λ_{min} is not being emphasized, just the existence of a minimum and its movement as Λ_{min} varies. [Right] The location of the minima in the left hand plot as a function of the lower bound used in the fit to Eq. (3.37).

limit. However, we also perform a similar fit to Eq. (3.44) for the cross sections at the same values of Λ_1 and Λ_2. Here, we choose a small region that straddles an unfortunate crossing of $\sigma(\Lambda_1)$ and $\sigma(\Lambda_2)$ at $\approx 0.75\,\text{fm}^{-1}$ and a zero in $\sigma(\Lambda_2)$ between 2 and 3 fm^{-1}. The slope from a fit to this small region is ≈ 3.3. A similar fit of $k\cot\delta$ at the same cutoffs results in a slope just a little greater than 1. These inconsistencies prohibit a strong conclusion about the value of n from Eq. (3.37) for two-body observables.

A closer examination of the cutoff dependence of the two-body scattering length reveals some interesting behavior that may explain the inconsistencies in our results. Fig. 3.6 contrasts the numerical results of $\Lambda(da/d\Lambda)$ against the expected behavior based on a fit to Eq. (3.37) with $n = 1.5$. Clearly, there is additional, oscillatory behavior that is not captured by the simple form of Eq. (3.37). Similar oscillations are observed in the two-body phase shifts as well. These oscillations are likely responsible for the variation in n as the window of Λ values is adjusted.

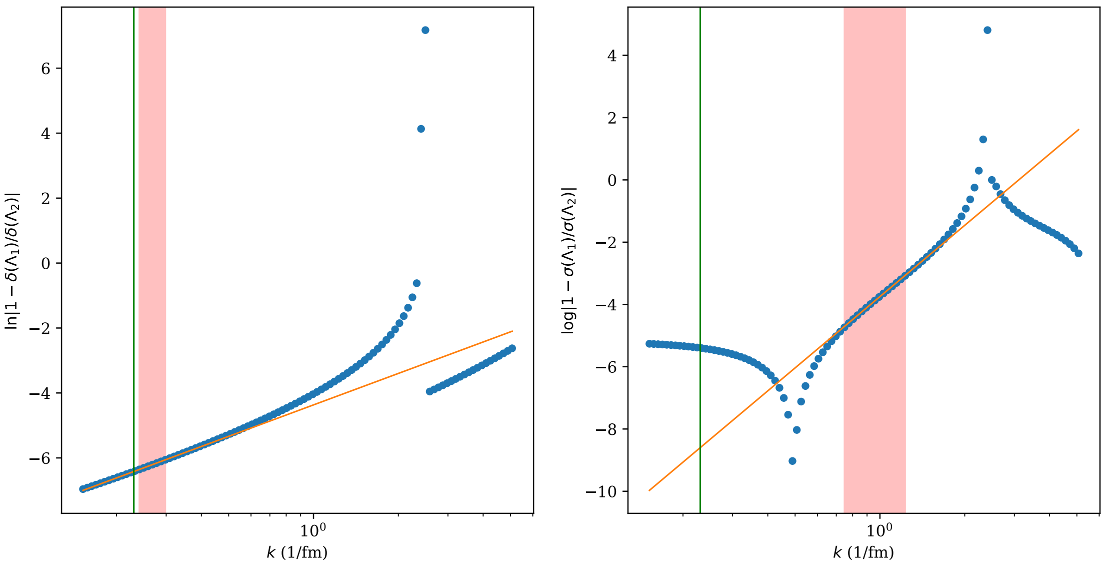

Figure 3.5: [Left] Residual cutoff corrections to the two-body phase shifts as a function of the relative momentum. The blue circles represent the numerical calculation. The yellow line represents the fit to Eq. (3.44). The pink, shaded region represents the range of k over which the fit was performed. The vertical, green line is the binding momentum γ. [Right] Residual cutoff corrections to the two-body cross sections at two distinct Λ values. The legend goes similarly to the left-hand plot.

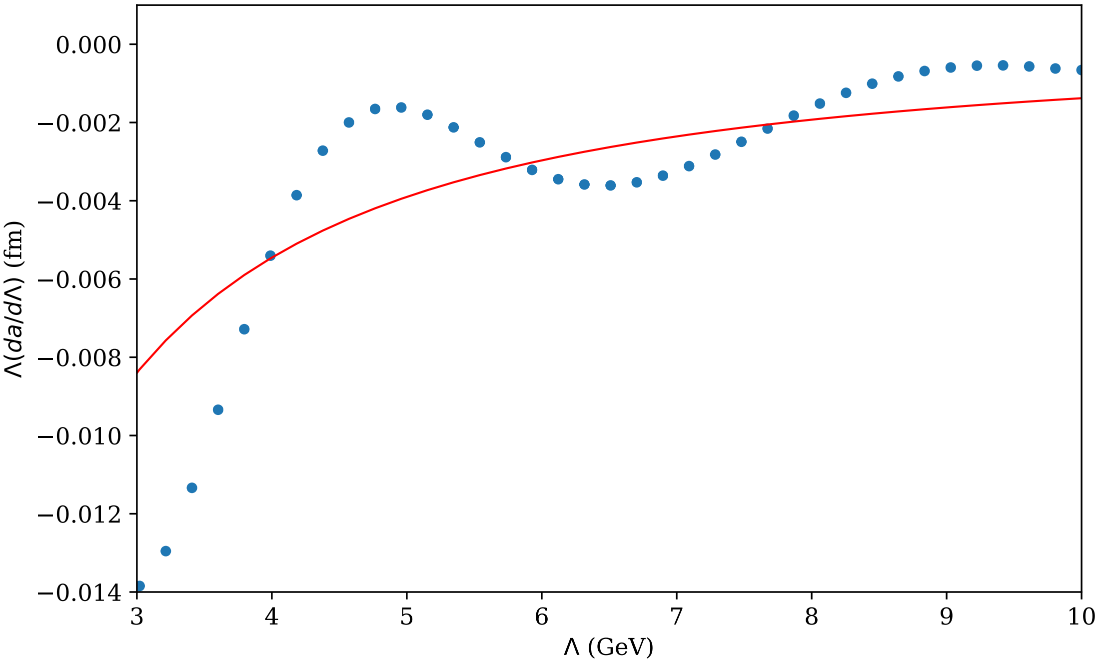

Figure 3.6: $\Lambda(da/d\Lambda)$ as a function of the cutoff. The blue dots are the numerical calculation. The solid, red line is the expected behavior based on a fit to Eq. (3.37) with $n = 1.5$.

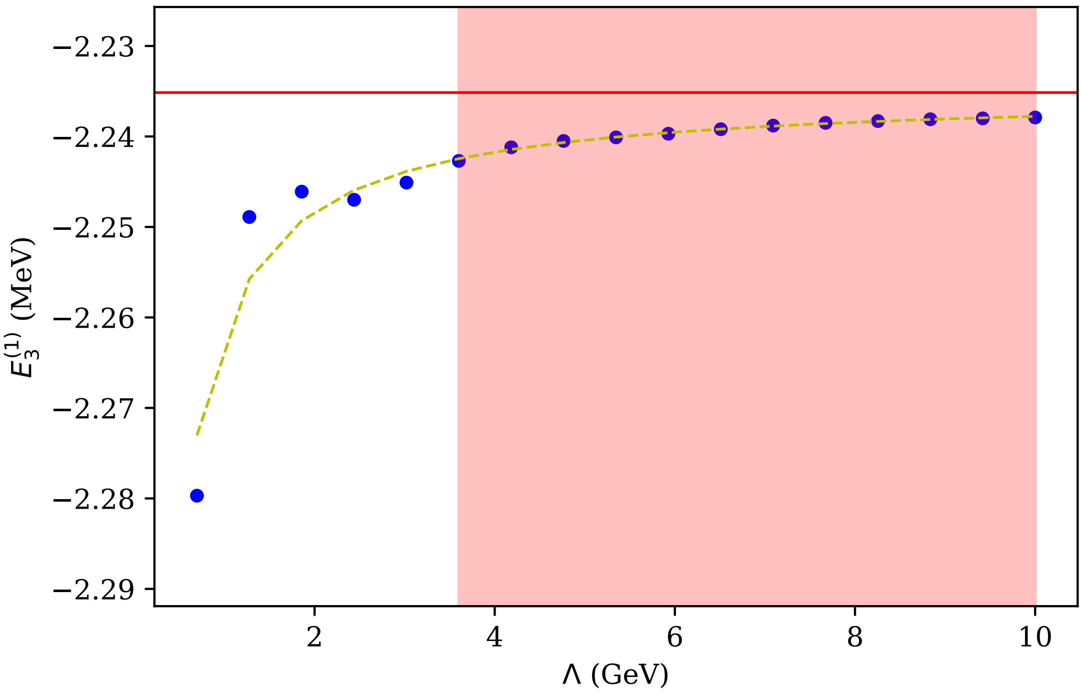

Figure 3.7: Three-body excited state/resonance energy as a function of the short-distance cutoff. Blue dots represent the numerical calculation. The yellow, dashed line represents a fit to Eq. (3.42). The red, solid line is $E_{3,\infty}^{(1)}$ from the fit to Eq. (3.37) with $n = 1$.

3.3.3 Three-Body Bound States

One of the main goals of these efforts has been to examine the sufficiency of a two-body counterterm to renormalize three-body observables. In Figs. 3.7 and 3.8, we plot the cutoff dependence of the three-body binding energies associated with two three-body states that appear in the system defined by the nonlocally regulated interaction Eq. (3.13).

The primary feature of Figs. 3.7 and 3.8 is the convergence of the binding energies. At ≈ 2 GeV, the binding energies (or rather, the resonant energies) begin to flatten out, just as in the two-body phase shifts.

We analyze the three-body states as we did the two-body scattering length — fitting the energy values over a wide range of cutoffs to Eq. (3.37) for a range n values and calculating Eq. (3.38) each time. The n values for which p_n is a minimum are plotted in Fig. 3.9. The left-hand plot in Fig. 3.9 corresponds to the ground three-body state; the right-hand plot in Fig. 3.9 corresponds to the excited three-body state. Again, we see a strong sensitivity to

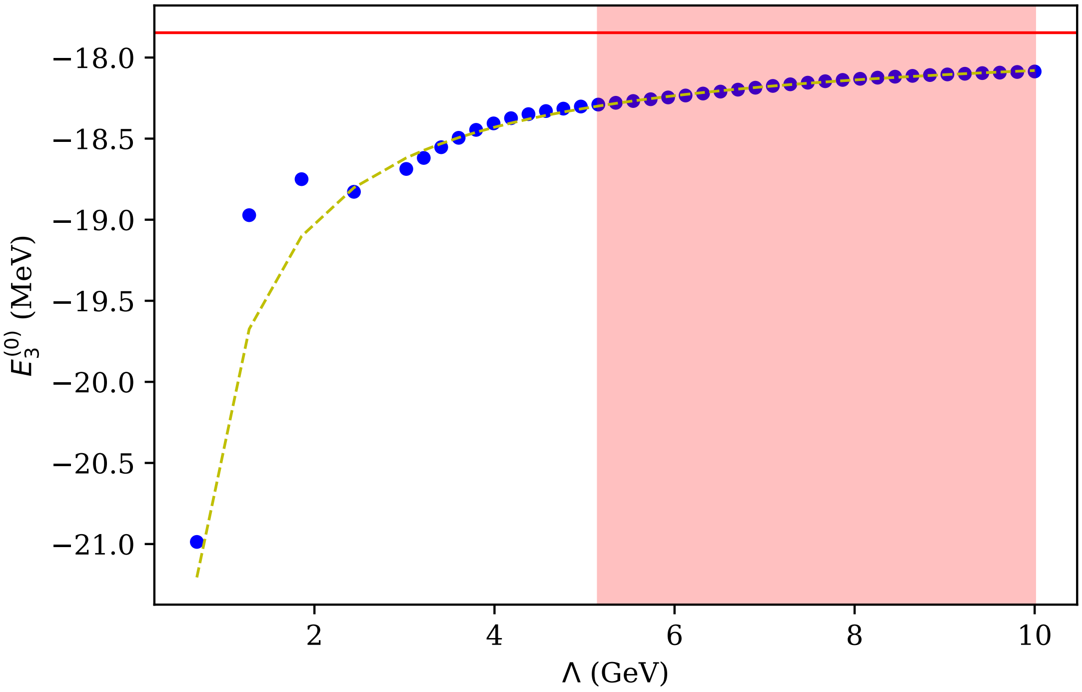

Figure 3.8: Three-body ground state/resonance energy as a function of the short-distance cutoff. Blue dots represent the numerical calculation. The yellow, dashed line represents a fit to Eq. (3.42). The red, solid line is $E_{3,\infty}^{(0)}$ from the fit to Eq. (3.42) with $n = 1$.

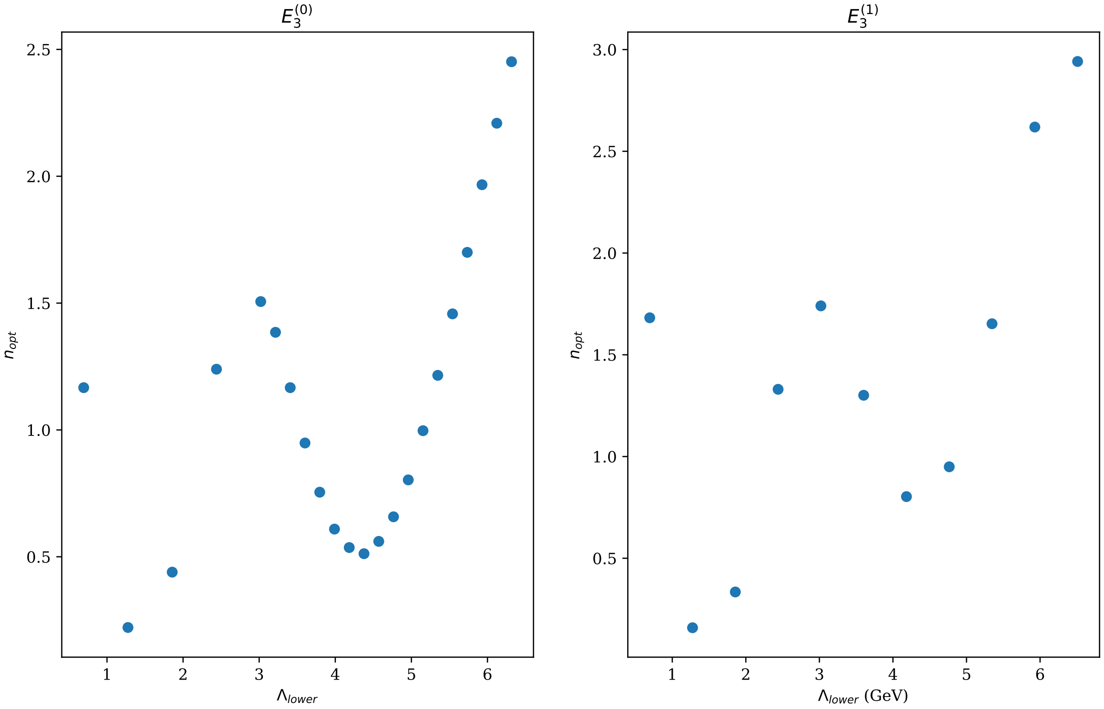

Figure 3.9: [Left] Optimal values of n from a minimization of p_n evaluated from a fit to Eq. (3.37) for the ground three-body state. [Right] Similar values of n from the same fit for the excited three-body state.

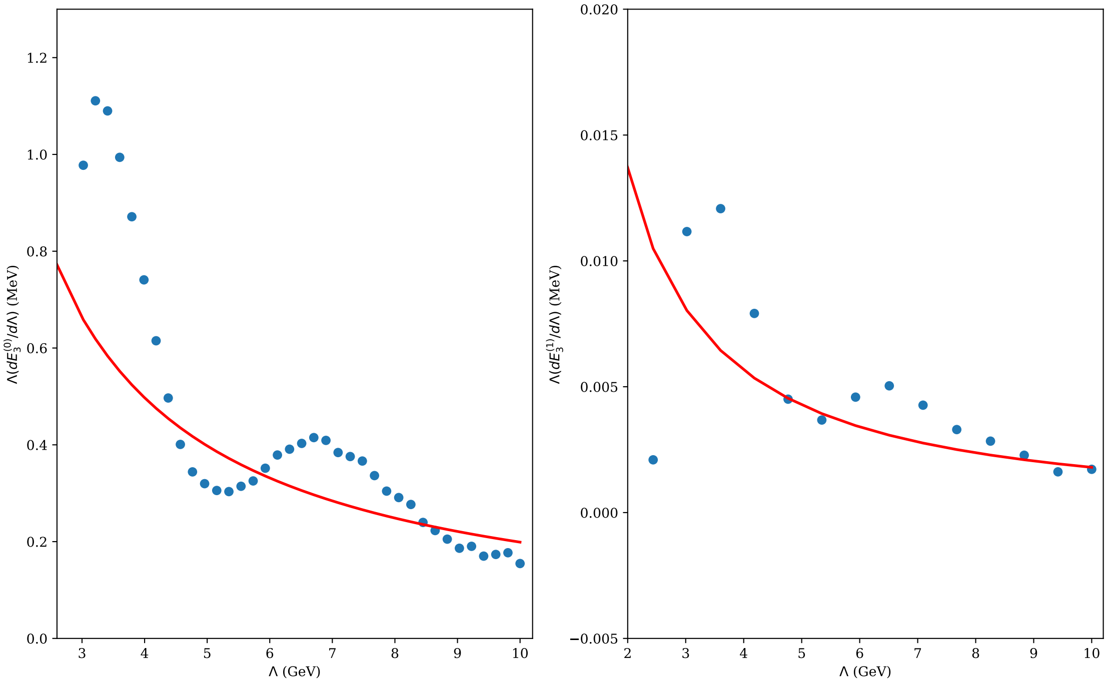

Figure 3.10: [Left] $\Lambda(d/d\Lambda)$ applied to the three-body ground state energy. The blue dots are the numerical calculation. The solid, red line is the expected behavior based on Eq. (3.37) with $n = 1$. [Right] $\Lambda(d/d\Lambda)$ applied to the three-body excited state. The blue dots and solid, red line are as in the left-hand plot.

the lower bound Λ_{min} used in the fit. If Eq. (3.37) accurately captured the behavior of the cutoff dependence, one would expect these n_{opt} values to converge as the window of cutoff values focuses increasingly on larger values of Λ. However, we see no such convergence.

Fig. 3.10 shows the same $\Lambda(d/d\Lambda)$ analysis we performed with the two-body scattering length. Clearly there are oscillations in the cutoff dependence that are not properly accounted for by a simple power series expansion. These oscillations are again suspected as the source of the inconsistencies we encounter when fitting n.

3.3.4 Three-Body Scattering

Alongside the binding energies, we also study the cutoff dependence of the atom-dimer (or 2+1) scattering length, a_{AD}, shown in Fig. 3.11.

As with the two-body scattering length, we show our analysis of the cutoff dependence of the atom-dimer scattering length in Fig. 3.12. The plot is similar to the right-hand plot

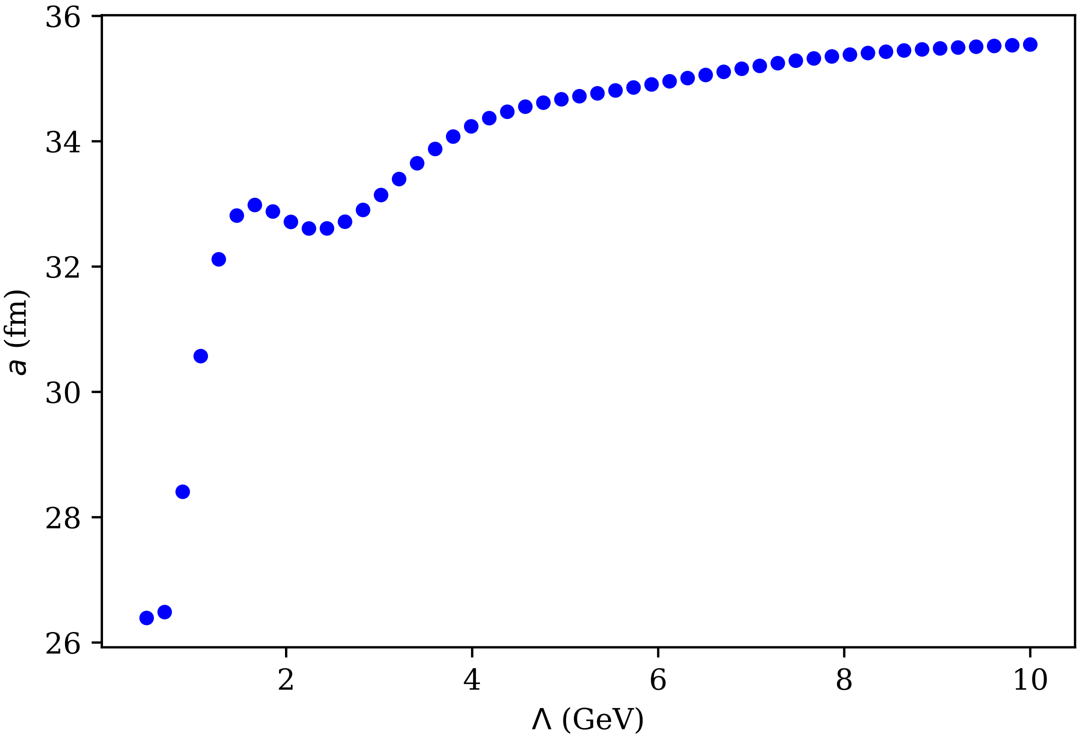

Figure 3.11: The cutoff dependence of the atom-dimer scattering length.

in Fig. 3.3. We track the value of n that minimizes our penalty function Eq. (3.38). We see the same kind of sensitivity to Λ_{min} and the same increase as the coefficients c_n grow unnaturally large.

Looking closer at the cutoff dependence of a_{AD}, we see the now familiar oscillations, shown in Fig. 3.13 where they are enhanced by the taking the derivative of a_{AD} with respect to Λ. Again, these oscillations can not be captured by the power series expansion Eq. (3.36) we apply. They are most likely responsible for the sensitivity of n_{opt} to Λ_{min}.

3.4 Summary

In this manuscript, we have set out to understand the renormalization properties of the FRIC potential in the two- and three-body sector. In particular, we have studied the regulator dependence of observables such as two-body phase shifts, three-body binding energies, and the atom-dimer scattering length. Motivated by a recent development in the nuclear theory community, we did these calculations using different, frequently used regulator functions.

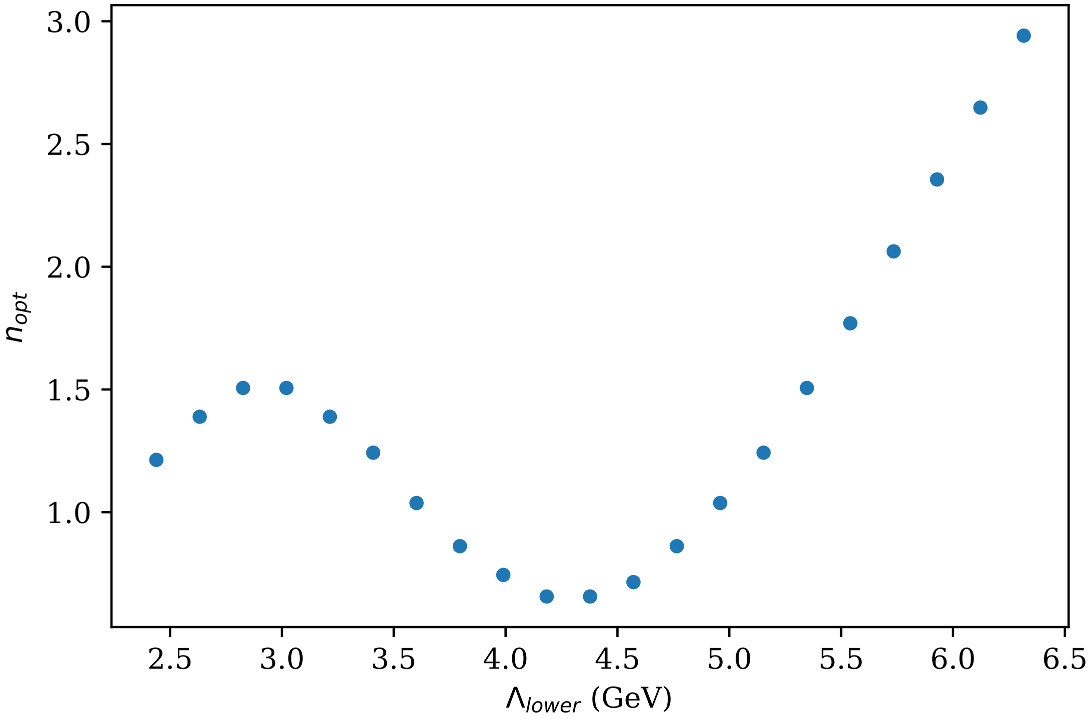

Figure 3.12: The x-axis is the lower bound of the cutoffs over which the fit to Eq. (3.37) was done. The y-axis is the power of the leading correction in Eq. (3.37) that minimizes the penalty function Eq. (3.38) for a_{AD}.

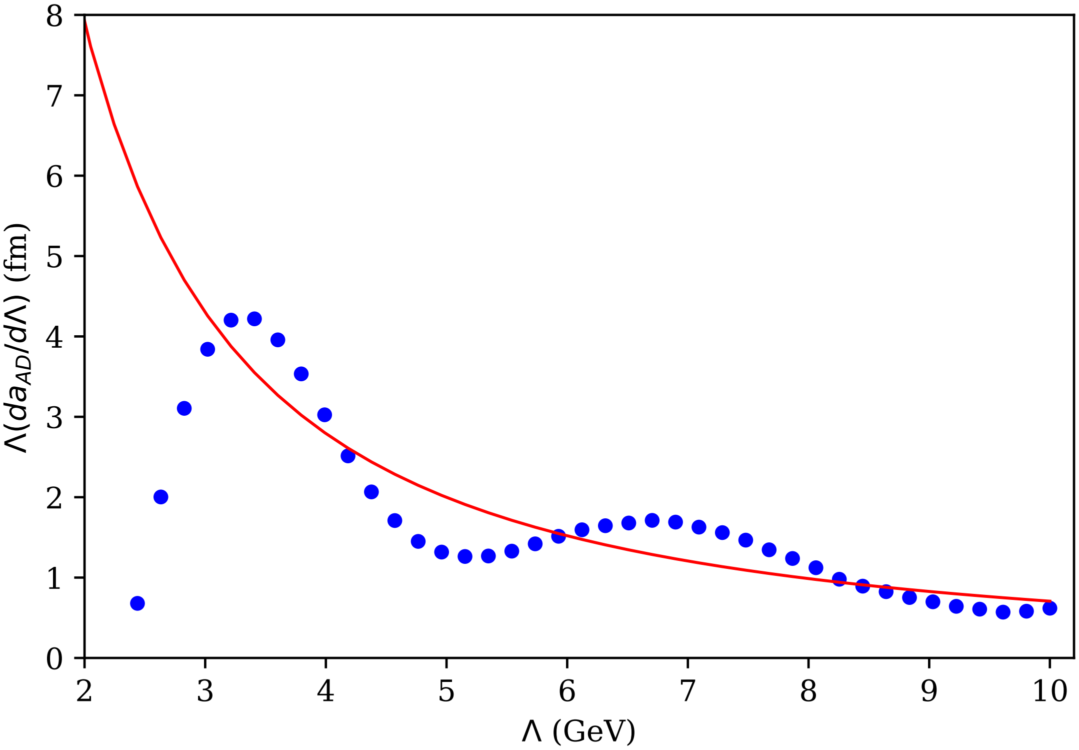

Figure 3.13: $\Lambda(d/d\Lambda)$ applied to the atom-dimer scattering length. Shown as a function of the cutoff. Blue dots are the numerical calculation. The solid, red line represents the expected behavior based on a fit to Eq. (3.37) with $n = 1.5$.

Our results in the two-body sector confirm that the two-body sector is properly renormalized. One input parameter is required (at leading order) to renormalize one low-energy counterterm and thereby the two-body sector. In the three-body sector, we have demonstrated that a three-body force is not needed at leading order to renormalize three-body observables for the inverse cube interaction.

In both the two- and three-body sectors, we have observed significant oscillatory behavior in the cutoff dependence of observables. These oscillations are not captured by a simple power series expansion. It is therefore hard to extract the leading cutoff dependence even when observables are calculated up to very large cutoffs. This is an important outcome since it seems to imply that a numerical analysis of cutoff dependence will also provide very limited information in the nuclear case. So while it is of course always possible to identify whether observables converge, it might not be easy to clarify whether the addition of a counterterm reduces the residual cutoff dependence as required in a working power counting scheme.

The oscillatory behavior of the cutoff dependence obscures a conclusive determination of the power of the LO correction. However, our analysis indicates that n is consistent with approximately 1.5 for two-body observables and approximately 1 for three-body observables. It is an interesting question whether this has any significance for the counting of two- and three-body counterterms in an EFT for the inverse cube potential. For example, the singular $1/r^2$ has been considered previously as the starting point for an EFT expansion in Ref. [34], however the inverse cube and all other singular coordinate space potentials need their own independent analysis.

Having tested several different local, semi-local, and nonlocal regulators and having found no significant differences, we conclude that these oscillations are most likely attributable to the singular nature of the inverse cube potential in coordinate space.

In the future, we plan to carry an analysis of higher order corrections in the three-boson and three-nucleon sector. However, we plan to also extend our work to the infinite range inverse cube potential that is of relevance to the atomic dipole interaction. This will let us combine the results obtained by Müller [40] with three-body observables and study the dependence of three-body observables on the boundary condition employed in the two-body sector. A more detailed analysis of the short-distance behaviour of the three-nucleon wave function might also provide novel insights into the power counting of electroweak currents [49].

Chapter 4

One-Pion Exchange

4.1 Introduction

The results shown in Ch. 3 motivated us to study the One-Pion-Exchange (OPE) potential directly. Specifically, we wanted to test the consistency between different regularization schemes. Alongside those tests, we also wanted to introduce a different regularization scheme that may offer the minimal number of required counterterms.

Motivated by Gao's result[24] for atomic systems and an unsuccessful attempt made by Nogga et al. [43] to renormalize all p-wave channels with a single counterterm with tensor structure, we sought to simplify the requirement established by previous work [52] which showed that counterterms are required in all attractive tensor channels. One promising technique previously applied to nuclear physics [5] is Pauli-Villars regularization which mimics the complicated spin-isospin structure of the OPE. Using this technique, we investigate the possibility of renormalizing all spin-triplet channels with a single counterterm.

4.2 Theory

In the following subsections, we describe the one-pion exchange potential and how it is regulated and renormalized. We also comment briefly on technical details such as the normalization of states and the calculation of observables through the Schrödinger and Lippmann-Schwinger equations.

4.2.1 One-Pion-Exchange Potential

The OPE is given in coordinate space by

$$V(\vec{r}) = \frac{m_\pi^3}{12\pi}\left(\frac{g_A}{2f_\pi}\right)^2 (\tau_1 \cdot \tau_2)\left[S_{12}T(r) + \sigma_1 \cdot \sigma_2 Y(r)\right] \tag{4.1}$$

where the pion mass $m_\pi = 138$ MeV, the axial coupling constant $g_A = 1.25$, the pion decay constant $f_\pi = 93$ MeV, τ_i is the isospin operator of the i-th particle, σ_i is the spin operator of the i-th particle, S_{12} is the tensor operator, and

$$\begin{aligned} T(r) &= \frac{e^{-m_\pi r}}{m_\pi r}\left[1 + \frac{3}{m_\pi r} + \frac{3}{m_\pi r}\right], \\ Y(r) &= \frac{e^{-m_\pi r}}{m_\pi r}. \end{aligned} \tag{4.2}$$

There are a couple of features of Eq. (4.1) we want to point out. One, the most singular piece of the OPE goes like $1/r^3$. Being more singular than $1/r$, this requires an additional boundary condition [34] that we impose with a local regulator function. Two, the attractiveness or repulsiveness of $T(r)$ and $Y(r)$ is determined by $(\tau_1 \cdot \tau_2)S_{12}$ and $(\tau_1 \cdot \tau_2)(\sigma_1 \cdot \sigma_2)$, respectively. The nuclear interaction conserves total angular momentum j, but it does not conserve the relative angular momentum l. This introduces $l_1 - l_2$ coupling in certain channels. This fact along with the variety of values and signs taken by $T(r)$ and $Y(r)$ introduces a significant amount of complex behavior.

In general, the complexity of this behavior can be ignored. Applying a local regulator and a simple (local or nonlocal) counterterm appears to be sufficient to produce accurate and stable results. However, as we present below, we have found that accommodating this complex behavior can result in a simplified renormalization procedure.

4.2.2 Regulator Formulations

The local, semi-local, and nonlocal regulation schemes were covered in Chapter 3 Section 3.2.1.

Pauli-Villars Regulation

Following a regularization technique developed in quantum field theory [46] and previously applied perturbatively in nuclear physics [5], we employ a local regulation scheme that is designed to capture all of the details of the OPE. The full potential is

$$V(\vec{r}) = \rho(r;R)\left[V_{1\pi}(\vec{r}) + g(M)V_{PV}(\vec{r};M)\right], \tag{4.3}$$

where $\rho(r;R)$ is a local regulator acting on the OPE and the Pauli-Villars term. $g(M)V_{PV}(r;M)$ resembles a heavy-particle-exchange potential with mass M and $g(M)$ is a tunable strength similar to $g(R)$. Here, M is the high-momentum scale on which our observables will depend. $\rho(r;R)$ is still necessary here as $V_{1\pi}(\vec{r})$ and $V_{PV}(\vec{r})$ are both singular, and of course, as before, there is a momentum scale associated with R. We choose $R \equiv 2/(10M)$ to ensure that M is the *lowest* and therefore the most influential of the two scales. $V_{PV}(r;M)$ is found by replacing m with M in Eq. (4.1). From Eq. (4.1) one can see that as M increases the range of $V_{PV}(r;M)$ decreases.

4.2.3 Lippmann-Schwinger Equation

To obtain two-body phase shifts, we calculate the numerical solution of the Lippmann-Schwinger Equation (LSE). In the partial wave projected momentum basis, we have

$$\begin{aligned}
\langle p\,\alpha|t|p'\alpha'\rangle &= \langle p\,\alpha|\tilde{V}|p'\alpha'\rangle + \langle p\,\alpha|\tilde{V}\,G_0(E)\,t|p'\alpha'\rangle \qquad (4.4)\\
&= \langle p\,\alpha|\tilde{V}|p'\alpha'\rangle + \sum_{\alpha''}\int_0^\infty dq\,q^2\,\frac{\langle p\,\alpha|\tilde{V}|q\,\alpha''\rangle\,\langle q\,\alpha''|t|p'\alpha'\rangle}{E+i\epsilon-q^2/m} \qquad (4.5)\\
t_{\alpha\alpha'}(p,p') &= \tilde{V}_{\alpha\alpha'}(p,p') + \sum_{\alpha''}\int_0^\infty dq\,q^2\,\frac{\tilde{V}_{\alpha\alpha''}(p,q)t_{\alpha''\alpha'}(q,p')}{E+i\epsilon-q^2/m} \qquad (4.6)
\end{aligned}$$

where m is the nucleon mass. For the sake of brevity, we have lumped all of the quantum numbers together in α. Our partial-wave states are normalized such that

$$\mathbb{I} = \sum_{l,m}\int dq\,q^2\;|q\,lm\rangle\,\langle q\,lm|\,. \tag{4.7}$$

For uncoupled channels, we extract take the on-shell matrix element $t_{\alpha\alpha}(p,p)$ and extract the phase shift via

$$t_{\alpha\alpha}(p,p) = -\frac{2}{m\pi}\frac{1}{p\cot\delta - ip}. \tag{4.8}$$

For coupled-channel calculations, we use the Stapp [54] parameterization of the S-matrix

$$S = \begin{pmatrix} \cos(2\bar{\epsilon})e^{2i\bar{\delta}_1} & i\sin(2\bar{\epsilon})e^{i(\bar{\delta}_1+\bar{\delta}_2)} \\ i\sin(2\bar{\epsilon})e^{i(\bar{\delta}_1+\bar{\delta}_2)} & \cos(2\bar{\epsilon})e^{2i\bar{\delta}_2} \end{pmatrix}. \tag{4.9}$$

The S-matrix is related to the t-matrix by

$$S = 1 - i\pi mqt. \tag{4.10}$$

where in the coupled-channel case,

$$t = \begin{pmatrix} t_{\alpha\alpha} & t_{\alpha\alpha'} \\ t_{\alpha'\alpha} & t_{\alpha'\alpha'} \end{pmatrix}. \tag{4.11}$$

Now, we calculate the Stapp parameters from the coupled-channel t-matrix amplitudes by

$$\begin{aligned} \tan 2\bar{\epsilon} &= \frac{-m\pi qt_{\alpha\alpha'}}{\left[(1-im\pi qt_{\alpha\alpha})\,(1-im\pi qt_{\alpha'\alpha'})\right]^{1/2}}, \\ e^{2i\bar{\delta}_1} &= \frac{1}{\cos 2\bar{\epsilon}}(1-i\pi mqt_{\alpha\alpha}), \\ e^{2i\bar{\delta}_2} &= \frac{1}{\cos 2\bar{\epsilon}}(1-i\pi mqt_{\alpha'\alpha'}), \end{aligned} \tag{4.12}$$

where the on-shell t-matrix element for arbitrary input channel β and output channel β' is

$$t_{\beta\beta'} = \langle q\beta | t(E = q^2/m) | q\beta' \rangle . \tag{4.13}$$

4.3 Results

The OPE potential is an important piece of chiral EFT, so we take the coordinate-space definition and apply the same tests as we did for the finite range inverse cubed potential.

First, we compare all four regulation techniques in the ${}^1S_0$ channel as well as the ${}^3S_1 - {}^3D_1$ channel. Second, we study the ${}^1P_1$ and ${}^1D_2$ channels with the Pauli-Villars RG flow in the ${}^1S_0$ channel. Finally, we apply the same analyses of the renormalization of the ${}^3P_1$, ${}^3D_2$, and ${}^3P_2 - {}^3F_2$ channels with the Pauli-Villars RG flow in the ${}^3S_1 - {}^3D_1$ channel.

The coordinate-space behavior of the ${}^1S_0$ channel is significantly different from the ${}^3S_1$ channel. In the ${}^1S_0$ channel, $S_{12} = 0$. What is left is simply the Yukawa term. On top of that, the interaction in the ${}^1S_0$ channel is repulsive as opposed to the attractive ${}^3S_1$ channel. Because of those differences, we get very different results as the reader will see below.

4.3.1 ${}^1S_0$ Channel

The local regulator used in the locally, semi-locally, and Pauli-Villars regulated cases is (per 3.4)

$$\rho(r; R) = 1 - e^{-(r/R)^2}, \tag{4.14}$$

and

$$\chi(r; R) = e^{-(r/R)^2}. \tag{4.15}$$

The nonlocal regulator we use in the semi-locally and nonlocally regulated cases is

$$\tilde{\chi}(p; R) = e^{-(pR/2)^2}. \tag{4.16}$$

In the Pauli-Villars regularization formulation, we regulate the OPE at $R = 1/(10M)$ fm. In all of these cases we tune g to reproduce the known ${}^1S_0$ scattering length $a_s = -23.75$ fm.

The RG flows generated by tuning the spin-singlet scattering length to $a_s = -23.75$ fm are shown in Fig. 4.1. The upper left and lower right plots correspond to the locally regulated Pauli-Villars regulated cases, respectively. Both schemes allow for multiple branches as with the inverse cube potential (see Sec. 3.3.1). What is shown is simply one of the non-unique paths. In the upper left plot of Fig. 4.1, the local counterterm is tuned such that the scattering length is reproduced and the number of states is fixed. It follows a single branch. In contrast, in the lower right plot of Fig. 4.1, the path shown "hops" across multiple

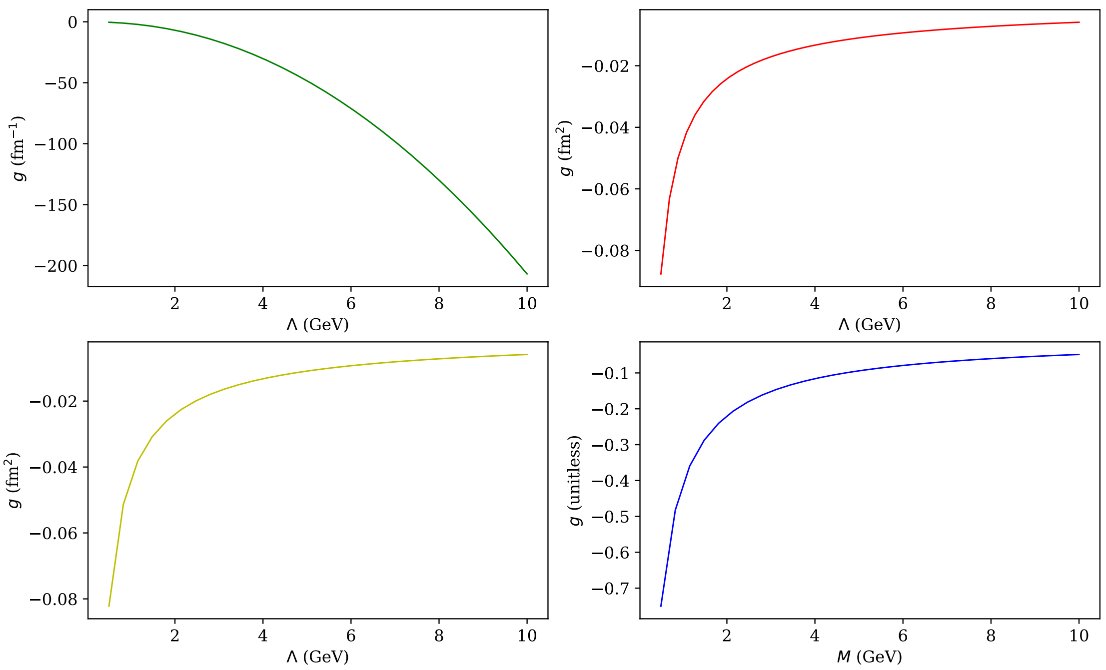

Figure 4.1: The running of the counterterm coupling constants for the locally (upper left), semi-locally (upper right), nonlocally (lower left), and Pauli-Villars regulated OPE potentials in the $^1S_0$ channel.

branches, resulting in a changing two-body spectrum as M increases. It was tuned in such a way as to minimize the absolute value of g. As shown in Fig. 4.3, the low-energy physics is the same regardless of the path chosen.

The cutoff dependence of the $^1S_0$ phase shifts is calculated using the RG flows shown in Fig. 4.1 and is shown in Fig. 4.2. Each of the four regularization schemes produces a similar LO approximation to the phase shift at $E = 2.5$ keV, and none of them change dramatically over the wide ranges of cutoffs or masses that were used in the calculation. This demonstrates the consistency between the different regulation techniques and the sufficiency of our single, two-body counterterm to renormalize two-body observables.

The energy dependence of $^1S_0$ phase shifts is calculated using the RG flows in Fig. 4.1 and is shown in Fig. 4.3. The maximum energy shown is only 2.5 MeV. This was chosen for two reasons. First, it highlights that the four regularization techniques produce accurate and similar results at low energies. Second, the $^1S_0$ channel phase shifts have a notoriously sharp turn above ≈ 1 MeV. At LO, it is very difficult to reproduce this turn as one can see from other approaches [52, 43, 58].

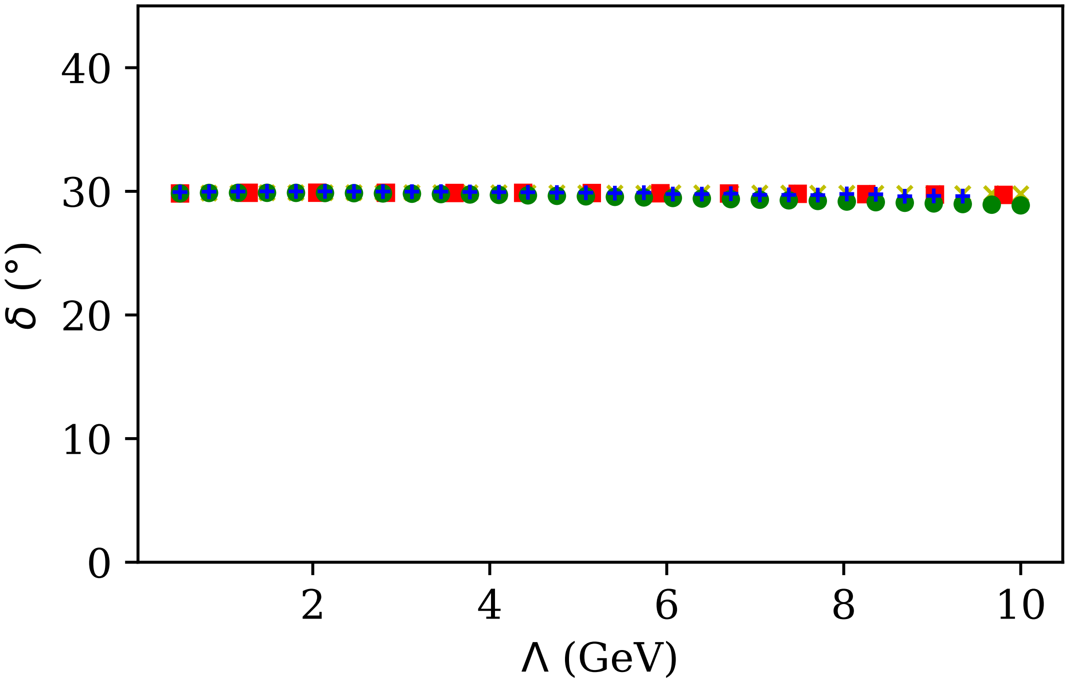

Figure 4.2: ${}^1S_0$ phase shifts using local (green circles), semi-local (red squares), nonlocal (yellow x's), and Pauli-Villars regularization (blue plus signs). These phase shifts are shown for $E = 2.5$ keV.

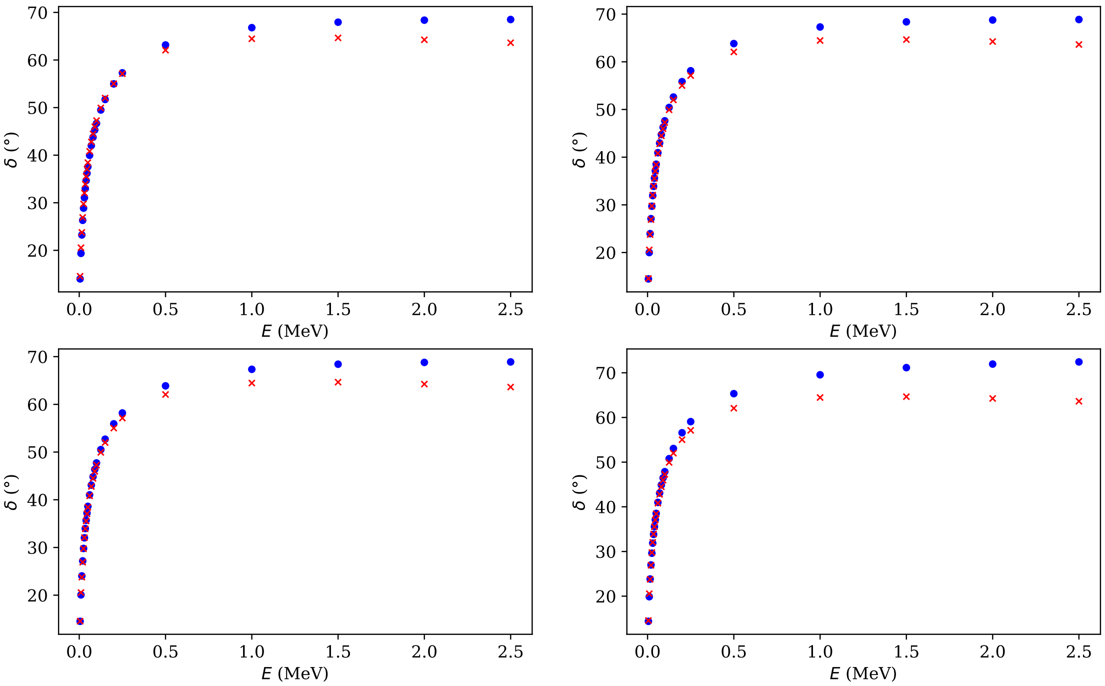

Figure 4.3: ${}^1S_0$ phase shifts using local (upper left), semi-local (upper right), nonlocal (lower left), and Pauli-Villars regularization (lower right). The blue circles correspond to our calculation while the red x's correspond to the Nijmegen partial-wave analysis PWA93. The momentum cutoff or mass used to calculate these phase shifts was 10 GeV.

4.3.2 $^3S_1$ Channel

The spin-triplet channel of the OPE also requires its own counterterm [43]. We perform the same procedure with the triplet channel of the OPE as we did with the singlet channel and the FRIC. The RG flows are calculated by tuning the scattering length of the triplet channel to $a_{\text{triplet}} = 5.42$ fm.

The local regulator used in the locally, semi-locally, and Pauli-Villars regulated schemes is

$$\rho(r; R) = \left[1 - e^{-(p/\Lambda)^2}\right]^4. \tag{4.17}$$

The local counterterm used in the locally regulated case is

$$\chi(r) = g(R)\, e^{-(r/R)^4}. \tag{4.18}$$

The nonlocal regulator used in the semi-locally and nonlocally regulated schemes is

$$\tilde{\chi}(p; R) = e^{-(pR/2)^4} \tag{4.19}$$

The RG flows found with the various regulation schemes are shown in 4.4.

The $^3S_1$ phase shift at $E = 10$ MeV for the four different regularization schemes is shown in Fig. 4.5 as a function of the high-momentum scale at which the potential is regulated. All four regularization schemes converge to a very similar value.

The energy dependence of the $^3S_1$ phase shifts is shown in Fig. 4.6.

4.3.3 Pauli-Villars Tensor Structure

Spin-Singlet Channels

One of the features of the Pauli-Villars regularization technique that we want to test is the tensor structure, specifically S_{12} is Eq. (4.1). By definition, our PV term potential has the same spin, isospin, and angular momentum structure as the OPE. This means that by fixing the deuteron binding energy in the $^3S_1 - ^3D_1$ channel we are also fixing the other spin-triplet channels.

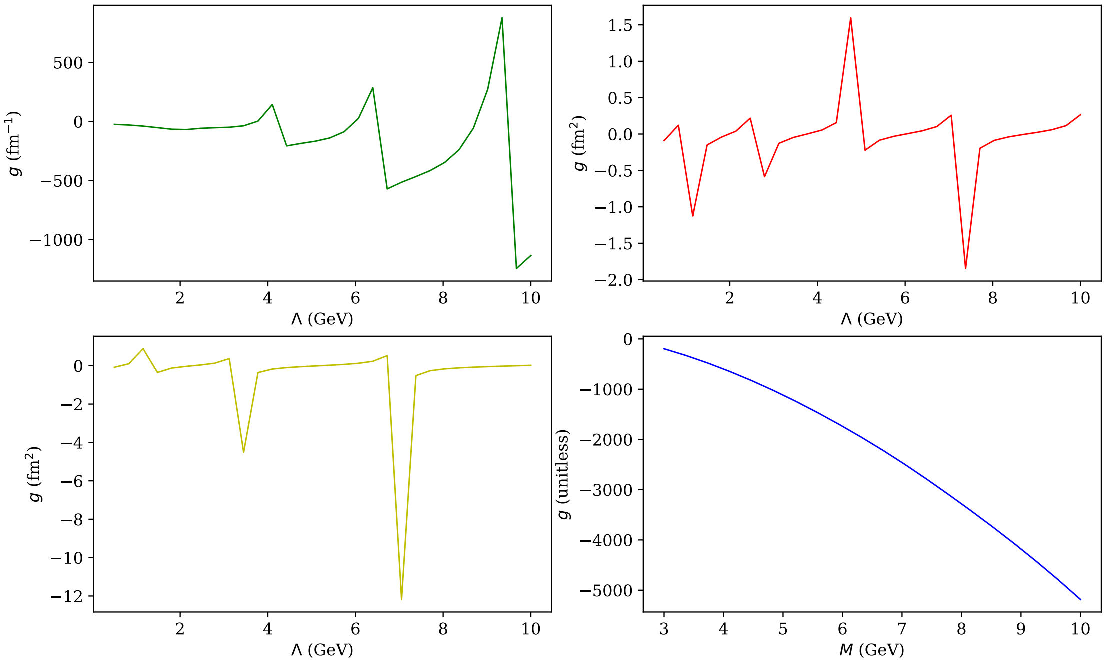

Figure 4.4: RG flows for the locally (upper left), semi-locally (upper right), nonlocally (lower left), and Pauli-Villars (lower right) regulated OPE potential in the $^3S_1$–$^3D_1$ channel.

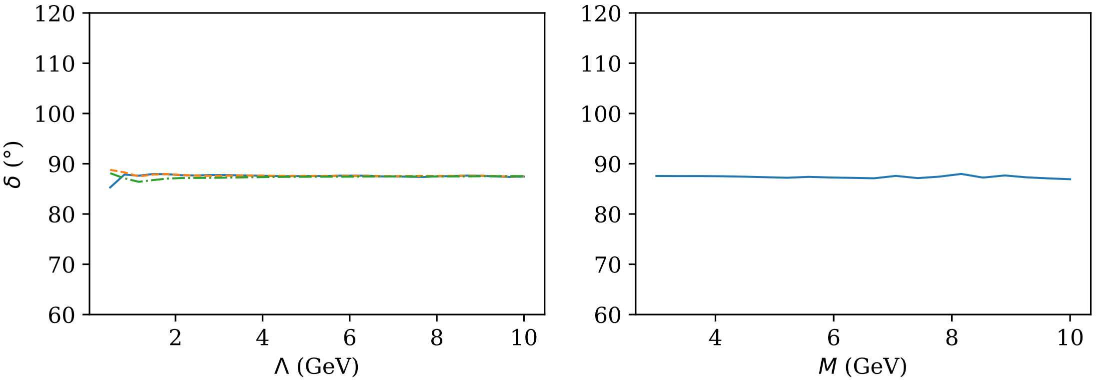

Figure 4.5: Cutoff dependence of the $^3S_1$ phase shifts at a center-of-mass energy of 10MeV for the locally (left plot, solid blue), semi-locally (left plot, green dot-dashed), nonlocally (left plot, yellow dashed), and Pauli-Villars (right plot) regulated OPE potentials.

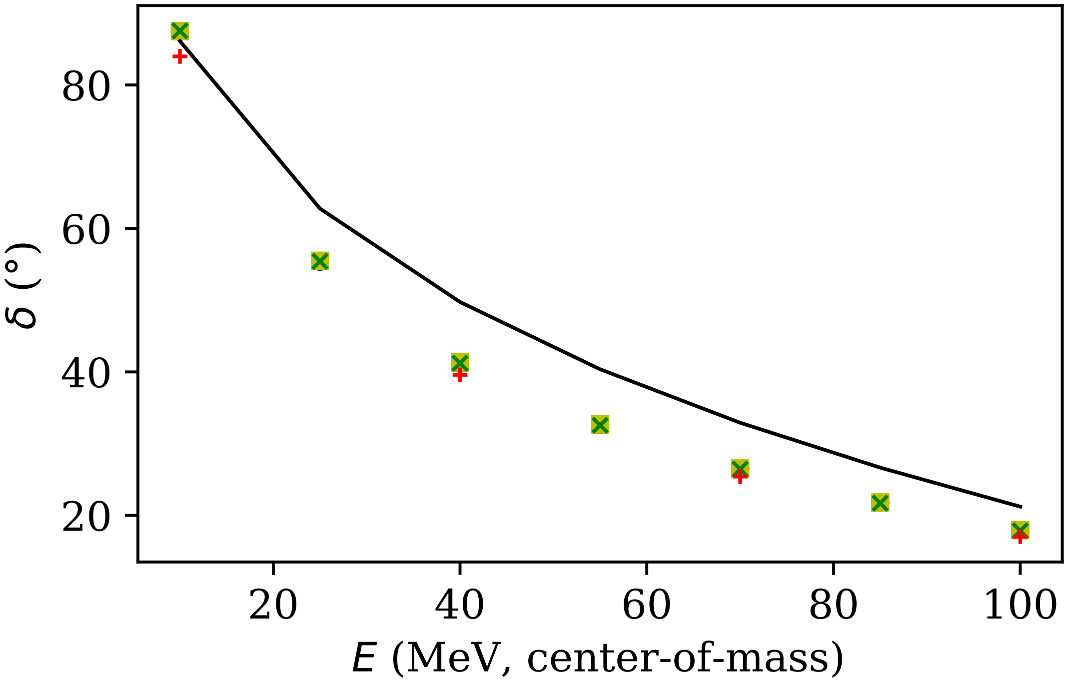

Figure 4.6: Energy dependence of the $^3S_1$ phase shifts for the locally (blue circles), semilocally (yellow squares), nonlocally (green x's), and Pauli-Villars (red +'s) regulated OPE potentials. The data from the Nijmegen PWA93 partial-wave analysis is represented by the solid, black line.

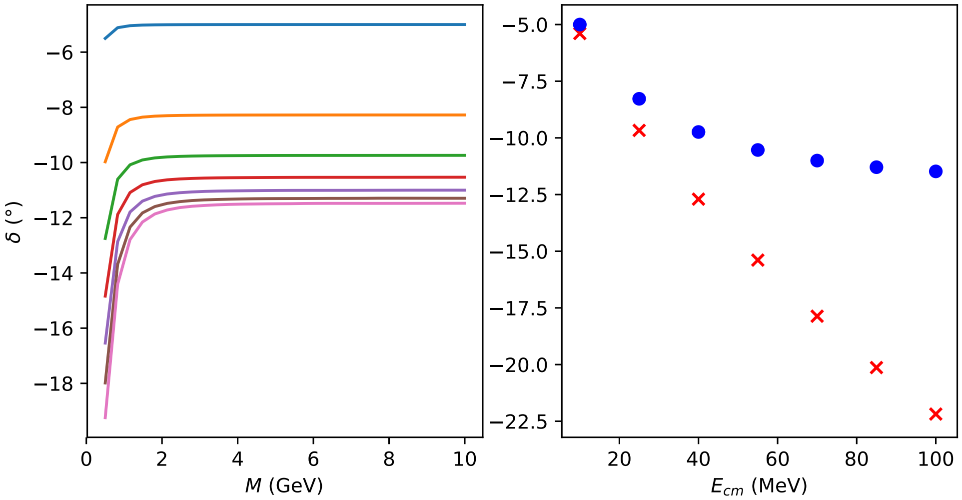

Figure 4.7: Phase shifts calculated with Pauli-Villars regularization in the $^1P_1$ channel. [Left] $^1P_1$ phase shifts as a function of the mass used in $V_{PV}(\vec{r})$. [Right] $^1P_1$ phase shifts at the maximum M value used in the calculation; plotted against the Nijmegen PWA93 data.

In Figs. 4.7 and 4.8, we try to exploit the tensor structure of the Pauli-Villars regularization to renormalize multiple channels with a single counterterm. We take the RG flow generated by tuning a_s in the $^1S_0$ and apply it to the phase shift calculations in the $^1P_1$ and $^1D_2$ channels.

Fig. 4.7 shows the cutoff dependence (left plot) and the energy dependence (right plot) of the $^1P_1$ phase shifts. The cutoff dependence clearly shows that the phase shifts are renormalized with the counterterm even though it is tuned in a different channel. The energy dependence shows that we are capturing the correct physics by comparing our values to the Nijmegen PWA93 partial-wave analysis. Our results are comparable to others' LO results [52, 43].

In Fig. 4.8, we see the same convergence with respect to M and accuracy with respect to E observed in the $^1D_2$ phase shifts. It should be noted that $S_{12} = 0$ in all spin-singlet channels and therefore do not require a counterterm [52]. The coefficient to $Y(r)$ does change by as much as a factor of -3. Of course, this is captured by $V_{PV}(\vec{r})$ precisely because it is chosen to replicate the OPE tensor structure. In this limited case, the Pauli-Villars regularization allows the counterterm to act outside of the channel in which it was tuned.

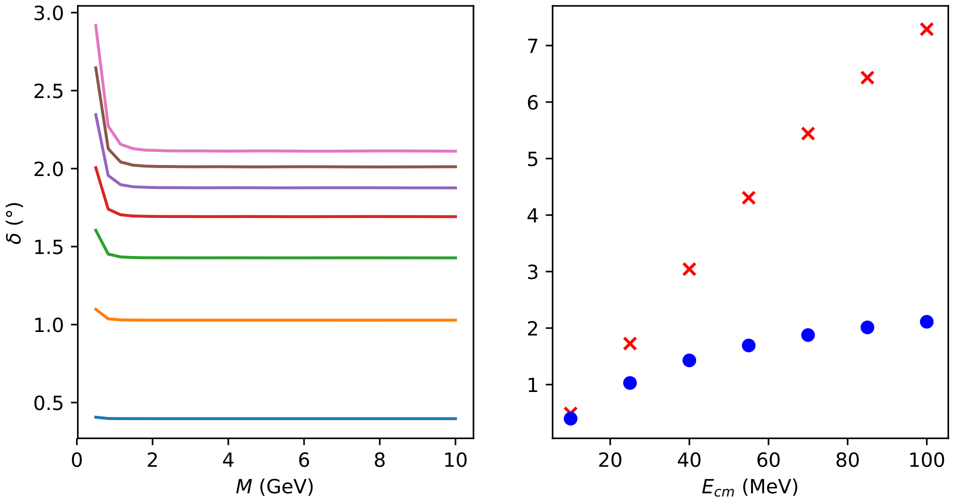

Figure 4.8: Phase shifts calculated with Pauli-Villars regularization in the $^1D_2$ channel. [Left] $^1D_2$ phase shifts as a function of the value of M used in $V_{PV}(\vec{r})$. [Right] $^1D_2$ phase shifts at the maximum M value used in the calculation (blue circles); plotted against the Nijmegen PWA93 data (red x's).

Spin-Triplet Channels

Having established some degree of confidence, we move on to the spin-triplet channels where we attempt to renormalize with a single counterterm using the Pauli-Villars regularization technique is the spin-triplet channels where the two spin-$\frac{1}{2}$ nucleons are coupled to a total spin of 1. In the s-wave channel, there exists a bound state, the deuteron. We fix the energy of this bound state by tuning $g(M)$ in (4.3). The $^3S_1 - {}^3D_1$ phase shifts were shown in Fig. 4.6.

We now extend that work and use the $g(M)$ values found by requiring the deuteron binding energy to calculate the phase shifts in other $S = 1$ channels. The $^3P_1$ phase shifts are showing in Fig. 4.9. The left plot shows the convergence of the phase shifts with respect to the fictitious mass in $V_{PV}(\vec{r})$. The right plot clearly displays that the correct physics is being captured as the low-energy phase shifts match up with the Nijmegen PWA93 data very well. Of course, as expected in an effective theory, the calculations increasingly deviate from experiment at high energy.

The $^3P_1$ channel is a repulsive tensor channel. According to Song et al. [52], a counterterm is not required to renormalize this channel. If we remove the counterterm and plot the cutoff

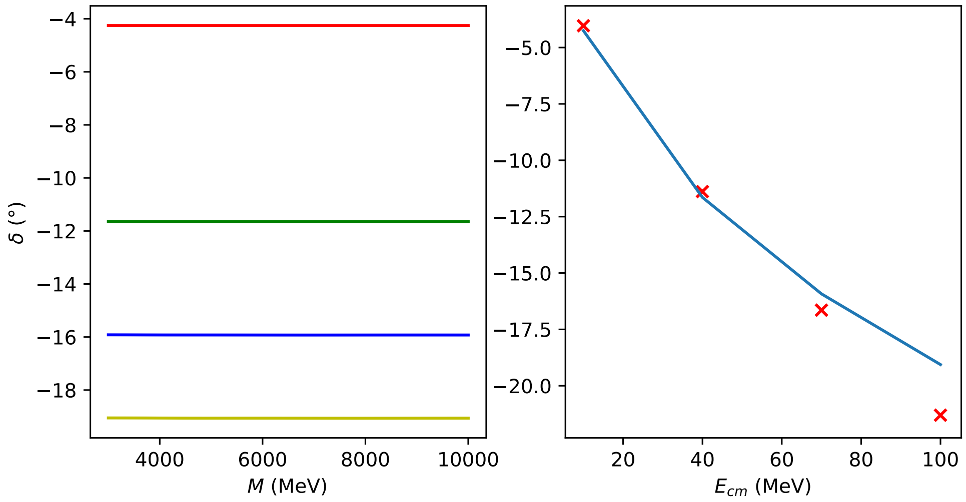

Figure 4.9: $^3P_1$ phase shifts calculated with the Pauli-Villars regularization technique. [Left] M dependence at 10 (red), 40 (green), 70 (blue), and 100 (yellow) MeV. [Right] Energy dependence of the calculated phase shifts (blue line) plotted against the Nijmegen PWA93 partial-wave analysis.

dependence, shown in Fig. 4.10, it is clear that the phase shift converges. In contrast, the $^3D_2$ channel is an attractive tensor channel, like the $^3S_1 -^3 D_1$ coupled channel in which the Pauli-Villars term is tuned. It serves as a much more rigorous test of our analysis.

The $^3D_2$ phase shifts are shown in Fig. 4.11. At lower values of M, the convergence and agreement with experiment is quite good. However, there appears to be some unfortunate "fine-tuning" at higher M values. We have tried a number of different approaches to remove this behavior including different local regulator forms, cutting off the Fourier transform in place of the local regulator, and repeating the calculation with the momentum-space definition of the interaction. The unexpected cutoff dependence persists regardless. At this point, we see the behavior as akin to the local regulator sensitivity though far more resilient.

One might hope that the unfortunate fine-tuning in the $^3D_2$ channel is isolated. It is not. The $^3P_2 - {}^3F_2$ phase shifts are shown in Fig. 4.12 and they contain the same type of unexpected cutoff dependence at as-yet-unpredictable values of M. Like the $^3S_1 - {}^3D_1$ channel, the $^3P_2 - {}^3F_2$ channel is a mixture of repulsive and attractive tensor interactions. Though we have not been able to eliminate the cutoff dependence to arbitrary cutoffs, we suspect that it is limited to attractive spin-triplet channels.

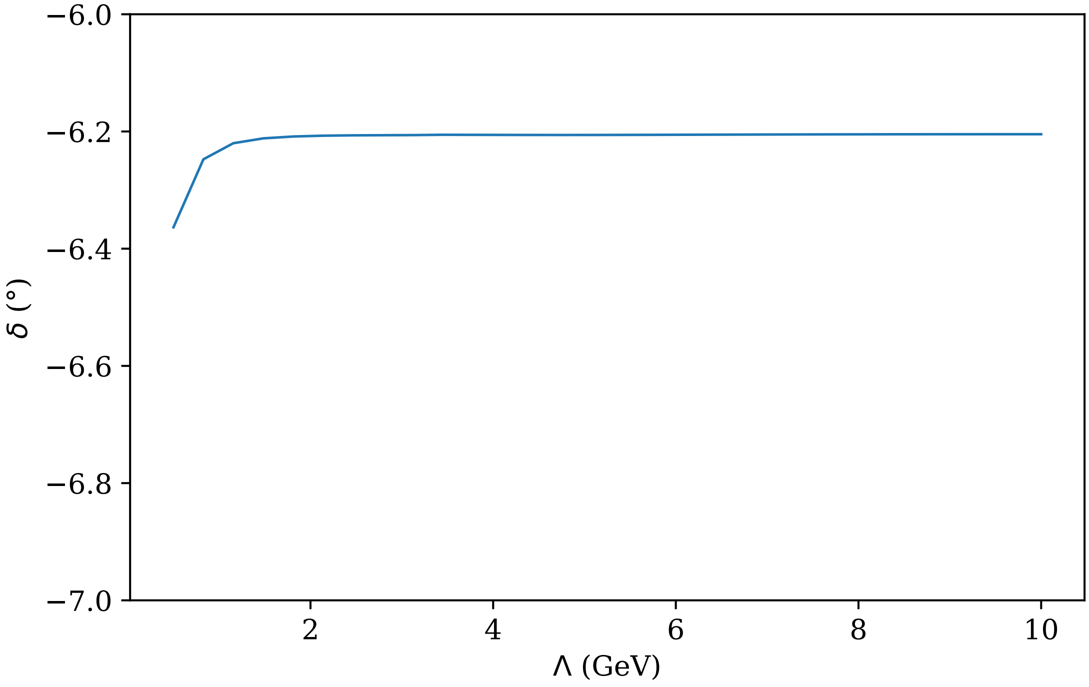

Figure 4.10: $^3P_1$ phase shift at a center-of-mass energy of 10 MeV as a function of the high-momentum (short-distance) cutoff. No counterterm is included in the calculation.

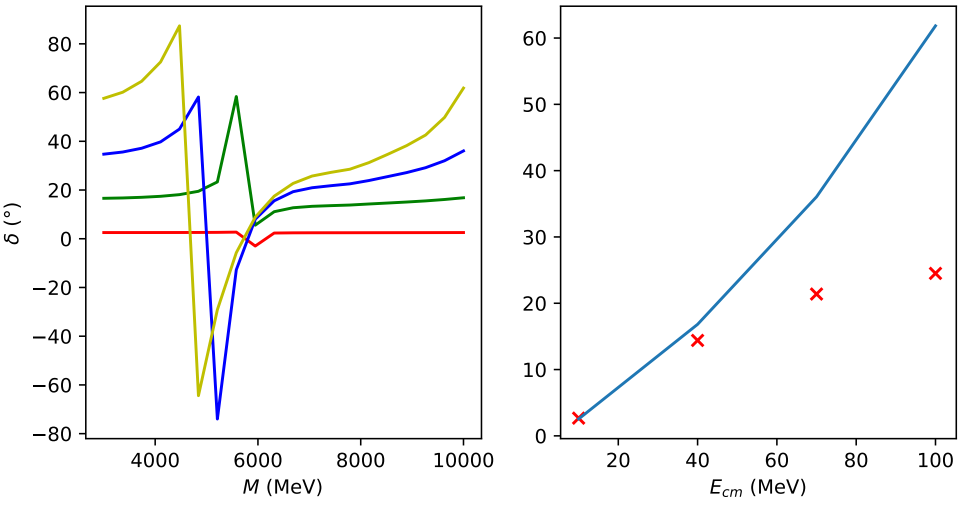

Figure 4.11: $^3D_2$ phase shifts calculated with the Pauli-Villars regularization technique. [Left] M dependence at 10 (red), 40 (green), 70 (blue), and 100 (yellow) MeV. [Right] Energy dependence of the calculated phase shifts (blue line) plotted against the Nijmegen PWA93 partial-wave analysis.

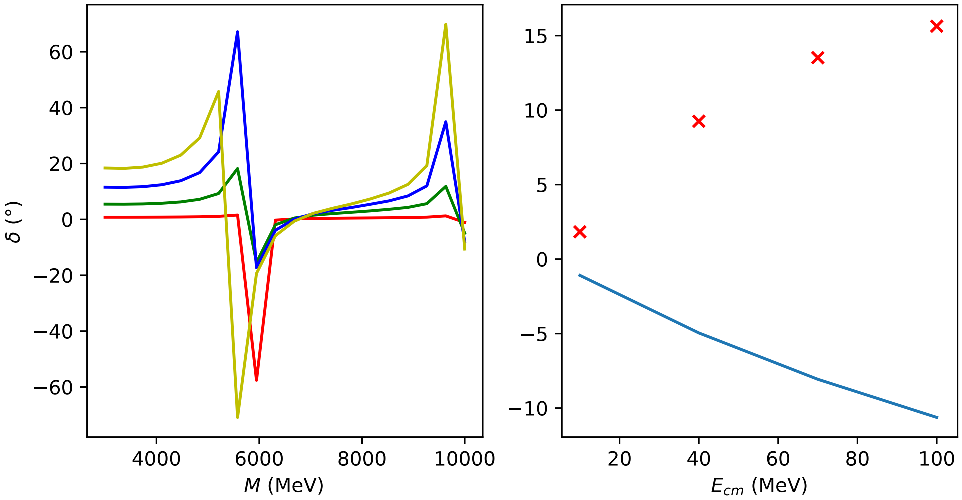

Figure 4.12: ${}^3P_2 - {}^3F_2$ phase shifts calculated with the Pauli-Villars regularization technique. [Left] M dependence at 10 (red), 40 (green), 70 (blue), and 100 (yellow) MeV. [Right] Energy dependence of the calculated phase shifts (blue line) plotted against the Nijmegen PWA93 partial-wave analysis.

4.4 Summary and Outlook

We have demonstrated numerical and physical consistency between the two-nucleon scattering observables found using three different regularization techniques: local, semi-local, and nonlocal. We have also shown that the use of the Pauli-Villars regularization technique fails to meet the goal for which we tasked it. While we are able to reduce the number of counterterms required to renormalize the spin-singlet channels and repulsive spin-triplet channels, the historically problematic attractive spin-triplet channels have failed to converge at large cutoffs.

In the future, we are working to implement a momentum-space formulation of the potential where

$$V(\vec{q}) = [V_{1\pi}(\vec{q}) - V_{PV}(\vec{q})] + gX(\vec{q}), \tag{4.20}$$

such that $[V_{1\pi}(\vec{q}) - V_{PV}(\vec{q})]$ always cancels at large $|\vec{q}|$ and the counterterm we add mimics the tensor structure but lacks the singular terms associated with the OPE.

Chapter 5

van der Waals Potential

5.1 Introduction

Cold, neutral atoms can induce dipole moments in one another. Fixed dipoles interact via a $1/r^3$ potential. The interaction of these *induced* dipoles, referred to the as van der Waals force, falls off like $1/r^6$. In systems where the electron configuration is such that these effects are pronounced (e.g. alkali metals), though $\lim_{r \to \infty} 1/r^6 = 0$, the long-range (low-energy) behavior is dominated by this $1/r^6$ tail.

Currently, these systems are studied with finely tuned potentials [2] composed of a $1/r^6$ tail and several terms accounting for short-distance effects. As the electron structure becomes more complex, the *ab initio* treatment of these short-range terms becomes untenable. Our goal is to apply an EFT description to these systems whereby the interaction consists minimally of a van der Waals tail and a parameterized contact interaction. This contact interaction can then be tuned to a number of different systems with widely varying electronic structures. Once LO is established, corrections to this simple description can be *systematically* included to improve the accuracy of the theory's predictions. Also, the universal features of the van der Waals potential [21, 41] — those depending solely on the strength of the potential — suggest that our description will be applicable to systems where the scattering length is not large.

In this chapter, we present the details of our proposed interaction as well as the results obtained in the two- and three-body sectors. We establish the renormalization of this LO interaction and test for the order of NLO corrections. We also show that our EFT is able to capture information about the system outside of large-scattering-length universality by explicitly including the van der Waals potential as the dominant, low-energy interaction. Many of the techniques will look familiar. In fact, much of the work presented in Chapters 3 and 4 came out of our initial investigation into the van der Waals potential.

5.2 Background

The van der Waals potential dominates the low-energy physics of alkali atoms, but it also has some universal features that make it particularly interesting to study. These "universal" features are universal in the sense that any system whose long-range behavior goes like $1/r^6$ has them.

5.2.1 Analytical Solutions

Bo Gao derived solutions to the attractive $1/r^6$ potential [22],

$$\begin{aligned} f^0_{El}(r) &= (\alpha^2_{El} + \beta^2_{El})^{-1}\left[\alpha_{El}\bar{f}_{El}(r) - \beta_{El}\bar{g}_{El}(r)\right] \\ g^0_{El}(r) &= (\alpha^2_{El} + \beta^2_{El})^{-1}\left[\beta_{El}\bar{f}_{El}(r) + \alpha_{El}\bar{g}_{El}(r)\right]. \end{aligned} \tag{5.1}$$

at energy E and angular momentum l. The general solution is composed of a linear combination of the two solutions

$$u_{El}(r) = A_{El}\left[f^0_{El}(r) - K^0_l g^0_{El}(r)\right]. \tag{5.2}$$

With those solutions and a technique called Quantum Defect Theory, he was able to calculate a modified effective range expansion and several universal relations for the observables in terms of the van der Waals length [21], the length scale associated with the strength of the van der Waals tail. With the potential described by $-C_6/r^6$, the length scale is defined as

$$\beta_6 \equiv (mC_6)^{1/4}, \tag{5.3}$$

where m is the mass. Of course, Gao solved the Schrödinger equation in the region where only the attractive $1/r^6$ acts. He connects the solution to the unknown, short-distance solution via the short-range K_l^0 matrix. For our purposes, this amounts to a boundary condition, set by the short-distance physics we wish to parameterize. The universal relations he gets are then dependent on the value of K_l^0. The scattering length and effective range are

$$\begin{aligned} a &= \frac{2\pi}{[\Gamma(1/4)]^2}\frac{K_0^0(0)-1}{K_0^0(0)}\beta_6 \ , \\ r_0 &\approx \frac{[\Gamma(1/4)]^2}{3\pi}\frac{K_0^0(0)^2+1}{[K_0^0(0)-1]^2}\beta_6 \ , \end{aligned} \tag{5.4}$$

where the $K_l^0(0)$ is evaluated at zero energy (threshold). The relation for r_0 is truncated under the assumption that the derivative of the short-range K-matrix is small. In effect, we can calculate the boundary condition, $K_0^0(0)$, from a, and then calculate r_0.

For bound states, Gao finds a expression for K_l^0 from the asymptotic forms of $f_{El}^0(r)$ and $g_{El}^0(r)$ given by $r \to \infty$

$$\begin{aligned} f_{El}^0(r) &\to (2\pi\kappa)^{-1/2}(W_{f-}e^{\kappa r} + W_{f+}e^{-\kappa r}) \ , \\ g_{El}^0(r) &\to (2\pi\kappa)^{-1/2}(W_{g-}e^{\kappa r} + W_{g+}e^{\kappa r}) \ , \end{aligned} \tag{5.5}$$

where κ represents the bound state momentum. The functions $W_{f\pm,g\pm}$ are defined by the energy and the shift in the order of the Bessel functions, and for the sake of brevity, we will not discuss their form. However, we can look at the asymptotic forms of f and g and conclude that in order to obtain a normalizable solution, the $e^{\kappa r}$ terms must cancel. This condition provides a restriction on K_l^0, and it is defined as

$$K_l^0(E) = \chi_l(\Delta) = W_{f-}/W_{g-} \ , \tag{5.6}$$

where $\Delta = 2\mu E\beta_6^2/16\hbar^2$.

An example plot of $\chi_{l=0}(\Delta)$ is shown in Fig. 5.1. Once $\chi_l(\Delta)$ is known (from the scattering length or a bound state), the intersections of the dashed, red line at that value and the $\chi_l(\Delta)$ function predict the presence of bound states.

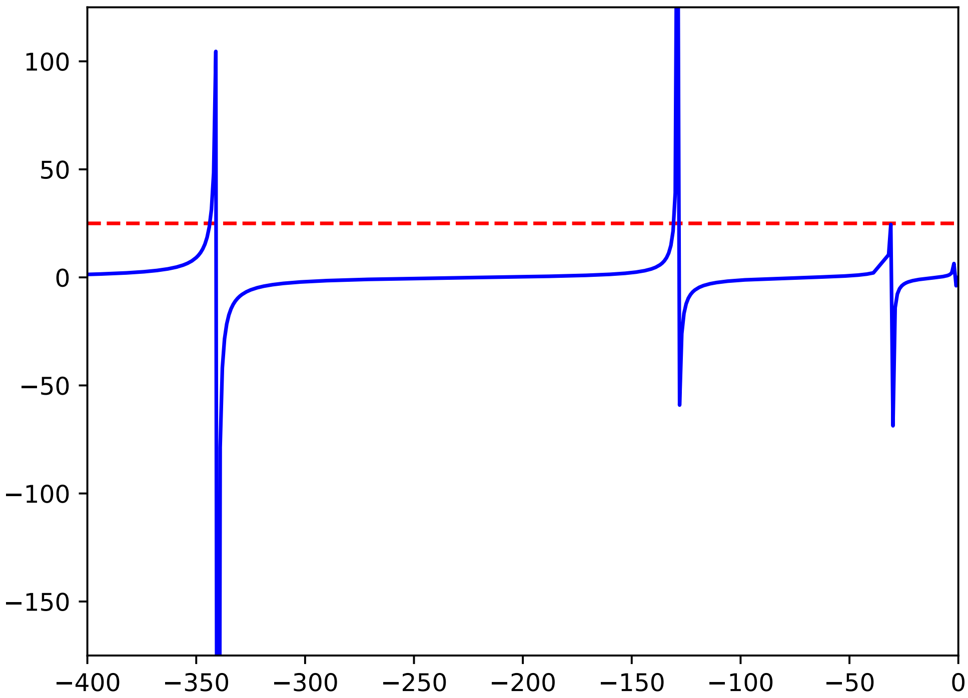

Figure 5.1: $\chi_{l=0}$ as a function of the dimensionless parameter Δ. The solid, blue line is $\chi_{l=0}$. The dashed, red line is example value of $\chi_{l=0}$ given to illustrate the multiple intersections and the corresponding bound state spectrum.

5.2.2 Universality in the Three-Body Sector

Another fascinating aspect of van der Waals universality is its reach beyond the two-body sector. In the three-body sector, the three-body parameter is defined at unitarity for three identical bosons by [8]

$$E_T^{(n)} \to \left(\frac{1}{515.03}\right)^{n-n_*} \frac{\hbar^2 \kappa_*^2}{m} \text{ as } n \to \infty \text{ with } a \to \pm\infty, \tag{5.7}$$

is related to β_6 by [41]

$$\kappa_*^{(0)} = 2(0.21 \pm 0.01)/\beta_6. \tag{5.8}$$

Also, the quantity a_- is the value of the scattering length where the three-body state disappears through threshold and is related to β_6 [41] by

$$a_- = -(10.70 \pm 0.35)\beta_6/2\ . \tag{5.9}$$

and with more testing, we intend to confirm Eq. (5.9) and improve the accuracy of the coefficient of β_6.

The implication from Eqs. (5.8), (5.9), and (5.4) is that, provided a system with a large two-body scattering length and $\beta_6 \gg R$, our proposed theory can fix the two- and three-body sectors simply by fixing a shallow, two-body state.

5.2.3 Feshbach Resonances

In general, the scattering length for a given system is fixed — a result of the particular configuration of the charge distribution and spin that describes the system. We study systems that have a large scattering length not because they occur in nature so frequently but because in atomic physics there is a very convenient technique for tuning the scattering length. The technique exploits the existence of Feshbach resonances [15].

If one is able to control the strength and range of an interaction, one can choose parameters that fix a bound state near threshold, thus giving a large scattering length. In practice, we do not have such control. However, Feshbach showed that when a state in an energetically forbidden (closed), weakly coupled channel is tuned to the threshold in the energetically allowed (open) channel, the scattering length goes like [8]

$$a(B) = a_{bg} + \frac{c}{B - B_{res}}, \tag{5.10}$$

where B is an externally applied magnetic field, c is the width of the resonance, and a_{bg} is the scattering length where B is far away from the resonant value B_{res}.

For our purposes, when we show observables as a function of the scattering length, we are addressing experimentally attainable regimes.

5.2.4 Efimov Effect

The Efimov Effect [11] is a phenomenon that occurs when a large scattering length exists between at least two particles in a three-particle system. Vitaly Efimov showed that when the magnitude of the scattering length is much larger than the range of the interaction, a system a trimers (three-body states) exists whose separation is set by a discrete scaling factor. In the case of identical bosons at the unitary limit where $a \to \pm\infty$, each state is separated by a factor of approximately 515 from the states above and/or below it. Under these circumstances, we expect that

$$E_3^{(n+1)}/E_3^{(n)} = e^{-2\pi/s_0}, \tag{5.11}$$

where $s_0 = 1.00624$. For finite scattering lengths as well as in the unitary limit, the three-body states are shown in Fig. 5.2 (previously presented by [8]) where

$$K = \text{sign}(E)\left(\frac{m|E|}{\hbar^2}\right)^{1/2} \tag{5.12}$$

is the trimer momentum variable, T represents a trimer state, AAA is the three-particle scattering region, and AD is the atom-dimer scattering region. Along the negative y-axis, the crossings of the trimer states correspond to the three-body parameter κ_* times some multiple of $\approx \sqrt{515} \approx 22.7$ Likewise, as $1/a$ moves to the left, the crossings of the trimer

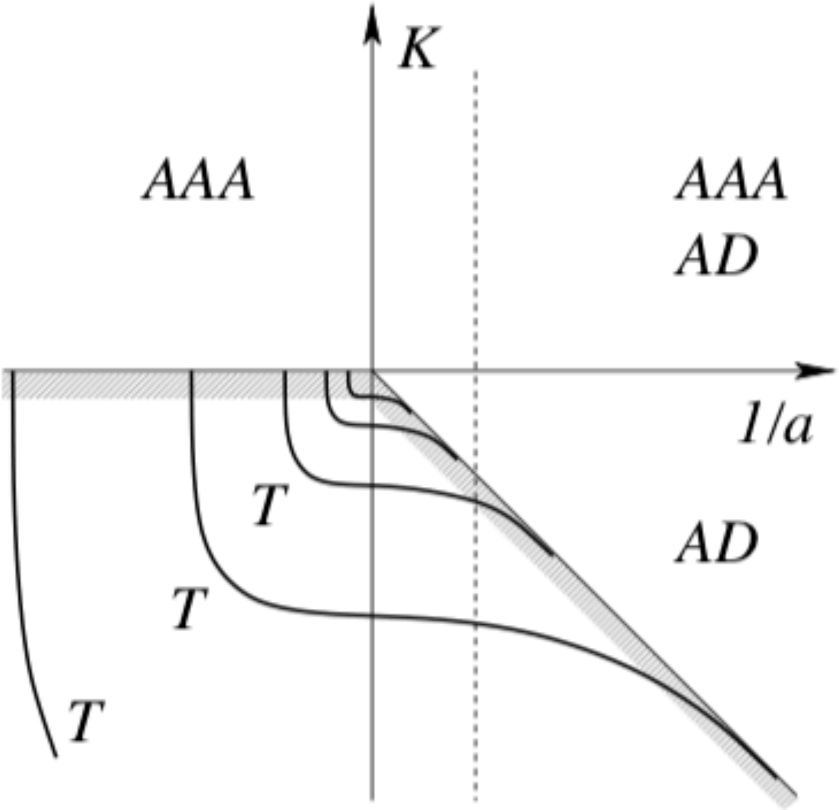

Figure 5.2: Efimov trimers as a function of the inverse scattering length.

states and the x-axis are separated by the same multiplicative factor. This discrete scaling is a universal feature of systems characterized by a large scattering length and will serve as a benchmark for our calculations.

The unique aspect for identical bosons interacting via a van der Waals potential, as mentioned in the previous section, is that not only is the separation between the three-body states fixed but there position is fixed as well. The advantage is that by fixing the shallow, two-body state, we gain information about about the three-body spectrum.

5.3 van der Waals Effective Field Theory

Systems characterized at low energies by a long-range van der Waals tail

$$V_6(r) = -\frac{C_6}{r^6}, \tag{5.13}$$

where C_6 is a measure of the strength, can have a number of different aspects as short distances. Our proposed theory is based on the assumption that we can parameterize those short-distance effects and *systematically* include corrections to that parameterization. We propose a nonlocally regulated, LO interaction of the form

$$\tilde{V}(p,k) = \tilde{\chi}(p;R)\tilde{V}_6(p,k)\tilde{\chi}(k;R) + g(R)\tilde{\chi}(p;R)\tilde{\chi}(k;R), \tag{5.14}$$

where $\tilde{V}_6(p,k)$ is the momentum-space, s-wave projection per Eq. 3.3 of

$$\rho(r;R_<)V_6(r), \tag{5.15}$$

with

$$\rho(r;R_<) = [1 - e^{-(r/R_<)^2}]^6, \tag{5.16}$$

and

$$\tilde{\chi}(p;R) = e^{-(pR/2)^6}, \tag{5.17}$$

and $R_< \equiv R/10$.

We arbitrarily choose the binding energy of the shallowest bound state of our system to be $B_2 = 1 \times 10^{-4}\ 1/\text{Å}^2$, which corresponds to a scattering length of $a \approx 100\text{Å}$. The mass of each particle is chosen to be 1. Our results for the simple model are discussed below.

5.3.1 Test Case

We tune $g(R)$ such that the shallowest bound state lies at a binding energy of our choosing, B_2. The result of that tuning over a range of R values is shown in Fig. 5.3. The system starts out with 2 two-body states, the shallowest of which lies at B_2. The first pole in the running of $g(R)$ corresponds to the inclusion of a third deep state. The second pole in the running of $g(R)$ corresponds to the inclusion of a fourth deep state. Because the counterterm is defined in momentum space while the long-range interaction is defined in coordinate space, the ratio g/C_6 has somewhat unhelpful units, but nevertheless, it provides a useful perspective on the repulsion/attraction required to maintain the shallow B_2.

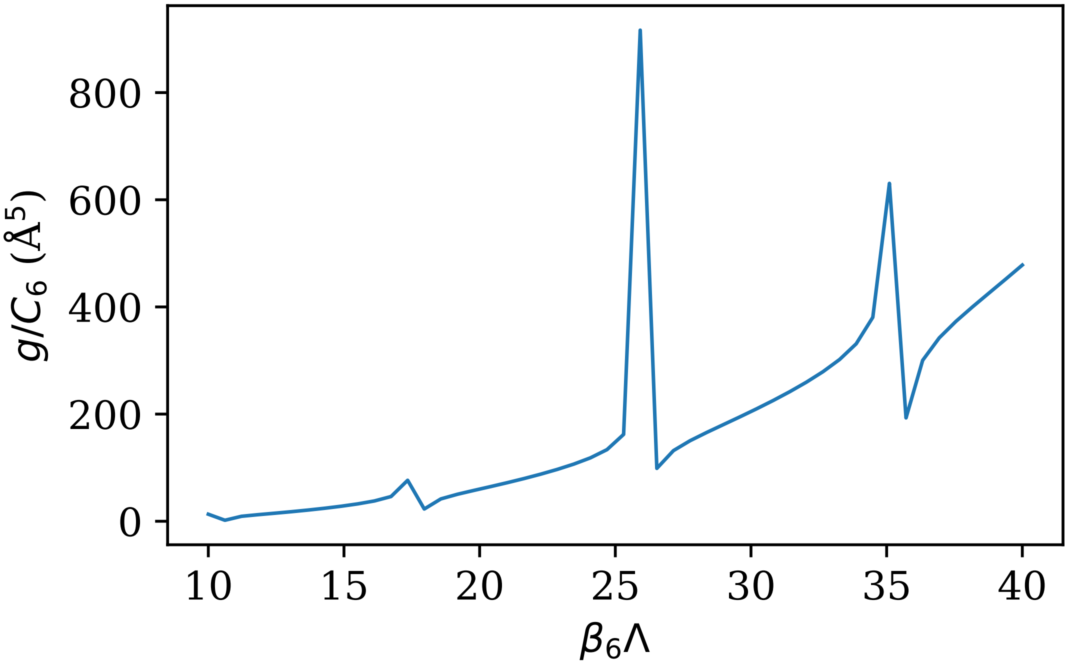

Figure 5.3: The running of the nonlocal counterterm strength as the momentum cutoff increases.

Using the RG flow in Fig. 5.3, we calculate the two-body scattering length as a function of $\beta_6\Lambda$ (with $\Lambda \equiv 2/R$) and show the results in Fig. 5.4. The blue, solid line is our calculation and the red, dashed line is a fit to Eq. (3.37). There are a few aspects of the plot that we wish to highlight. First, the curve is smooth and slowly flattens out, showing that the scattering length converges in the limit of $\Lambda \to \infty$. This shows that our two-body, contact-like counterterm is sufficient to renormalize two-body observables. Second, the value to which the scattering length converges is of the order of what we would expect. A shallow bound state of binding energy, B_2, corresponds to a large scattering length [8]

$$a \approx \sqrt{\frac{1}{mB_2}}. \tag{5.18}$$

With $B_2 = 1 \times 10^{-4}\text{Å}^{-2}$ and $m = 1$, we expect a scattering length close to 100Å which is very close to what we get. Finally, the fitted line shown is a fit to Eq. (3.37) with $n = 2$. However, similarly to the inverse cube study, there does not seem to be a clear determination of n. The standard deviation in the fit parameter c_n is roughly 4% as n is varied between 1 and 2.5.

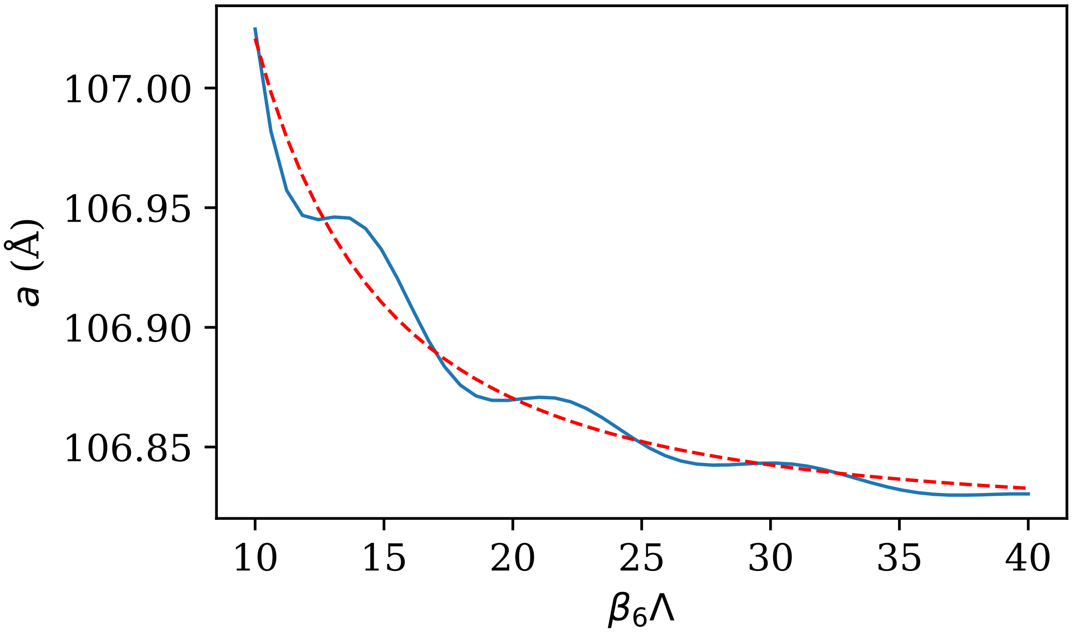

Figure 5.4: Two-body scattering length of our vdW test potential. The solid, blue line is our calculation. The dashed, red line represent a fit to Eq. (3.37).

From the plot, one can clearly see $a(\beta_6\Lambda)$ oscillating about the fit line. These oscillations are discouragingly similar to the inverse cube results and represent analytical behavior that is not captured by the simple power series expansion we propose (see Eq. (3.36)).

To highlight these oscillations, we plot $\Lambda(da/d\Lambda)$ in Fig. 5.5. While the function tends toward zero, there is a pronounced oscillatory dependence on Λ that obscures a well-supported conclusion on the value of n for the higher-order corrections. This is highlighted by taking the derivative of a with respect to Λ and compared to the expected behavior based on a fit to Eq. (3.37).

From the scattering length, we can calculate the short-range K-matrix via Eq. (5.4). Checking the intersections of that K-matrix value with $\chi_{l=0}$, we ought to be able to predict the presence of deeper, two-body bound states. Fig. 5.6 shows the deeper two-body state approaching the prediction from $\chi_{l=0}$ as $\beta_6\Lambda$ increases. We do not expect that the deeper spurious bound states that enter the spectrum will be predicted by the χ function as they are so deep that they corresponding the distances where the regulators have significant effects.

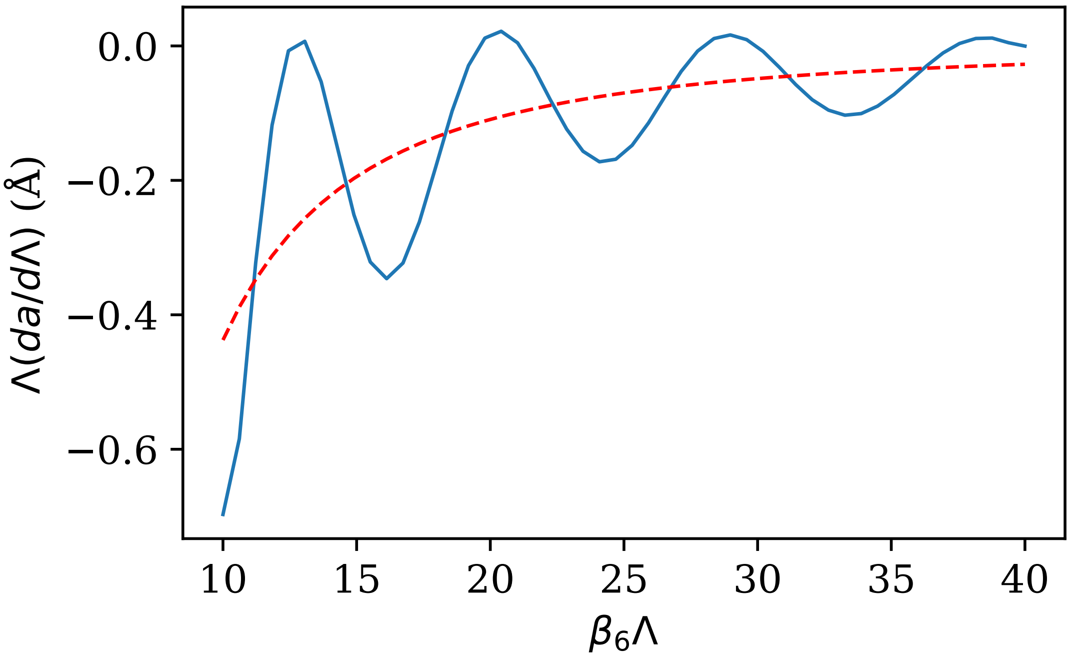

Figure 5.5: $\Lambda(d/d\Lambda)$ applied to the two-body scattering length of our vdW test potential as a function of the dimensionless quantity $\beta_6\Lambda$. The solid, blue line is our calculation. The dashed, red line is the expected behavior based on a fit to Eq. (3.37).

As a check of our scattering length calculation, we also show the phase shifts at three different energies: 0.001, 0.01, and 0.1 Å^{-2} in Fig. 5.7. The primary feature of the plot is the consistently flat behavior of the cutoff dependence at three different orders of magnitude. Along with the scattering length, this clearly demonstrates the sufficiency of a two-body, contact interaction to renormalization the vdW potential at short distances.

Unfortunately, applying the same $\Lambda(d/d\Lambda)$ analysis to the phase shifts, shown in Fig. 5.8, reveals the same oscillations seen in the scattering length. As expected, the functions tend toward zero, but the only insight gained from Fig. 5.8 is the increasing oscillation amplitude as the scattering energy E increases, an insight that fails to clearly reveal the source of these oscillations.

With the two-body observables renormalized, we turn to the three-body sector. From Section 5.2.2, we expect that the three-body bound states are fixed, at least in the unitary limit. The scattering length we chose is large which should get us close to the unitary limit. We plot our results as a function of $\beta_6\Lambda$ or $\beta_6(2/R)$ such that the asymptotic values meet

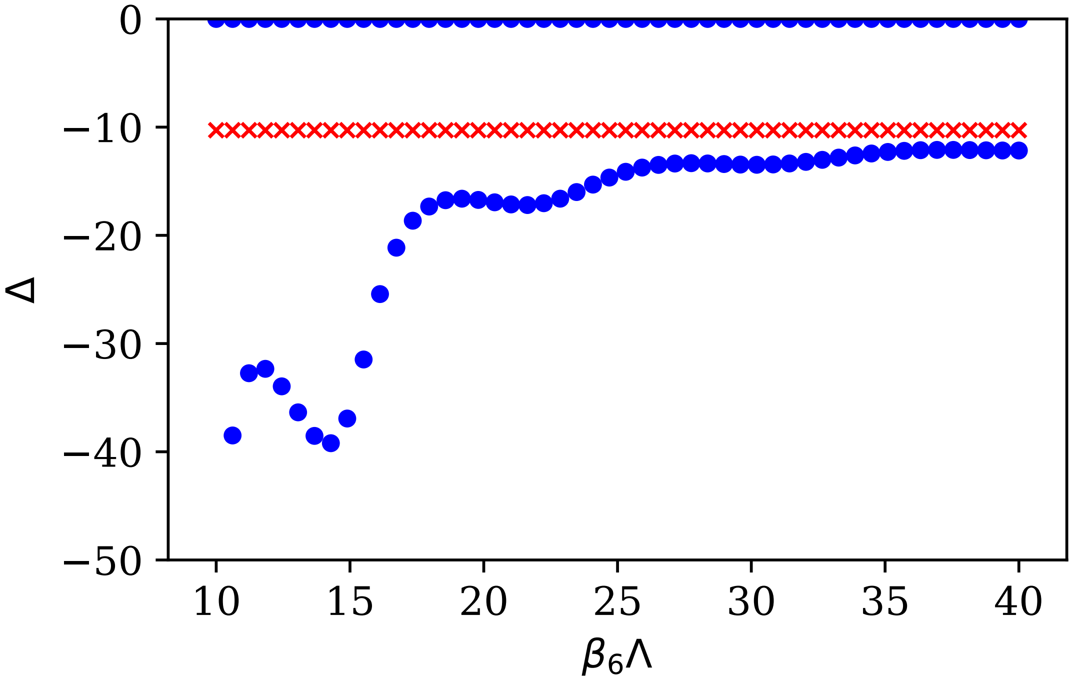

Figure 5.6: Two-body binding energies in our van der Waals test case potential as a function of the dimensionless parameter $\beta_6\Lambda$. The blue circles are the calculated values. The red x's correspond to the deeper state as predicted by the intersection of $K_0^0(0)$ and the $\chi_{l=0}$ function.

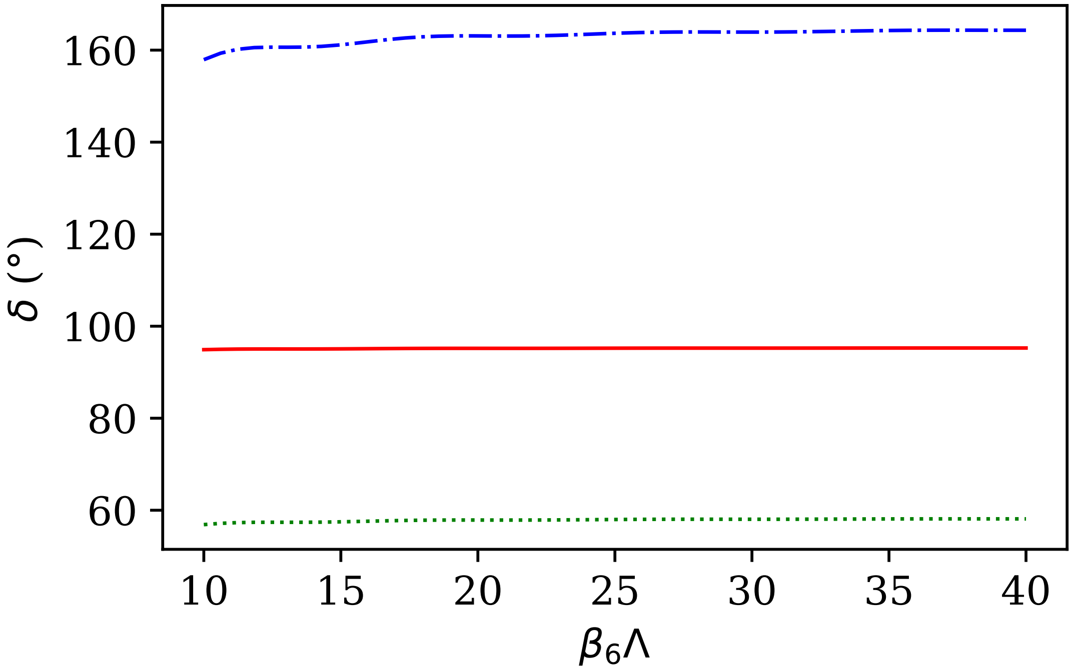

Figure 5.7: Phase shifts at 0.001 (red, solid line), 0.01 (green, dotted line), and 0.1 (blue, dot-dashed line) Å^{-2} as a function of the dimensionless parameter $\beta_6\Lambda$.

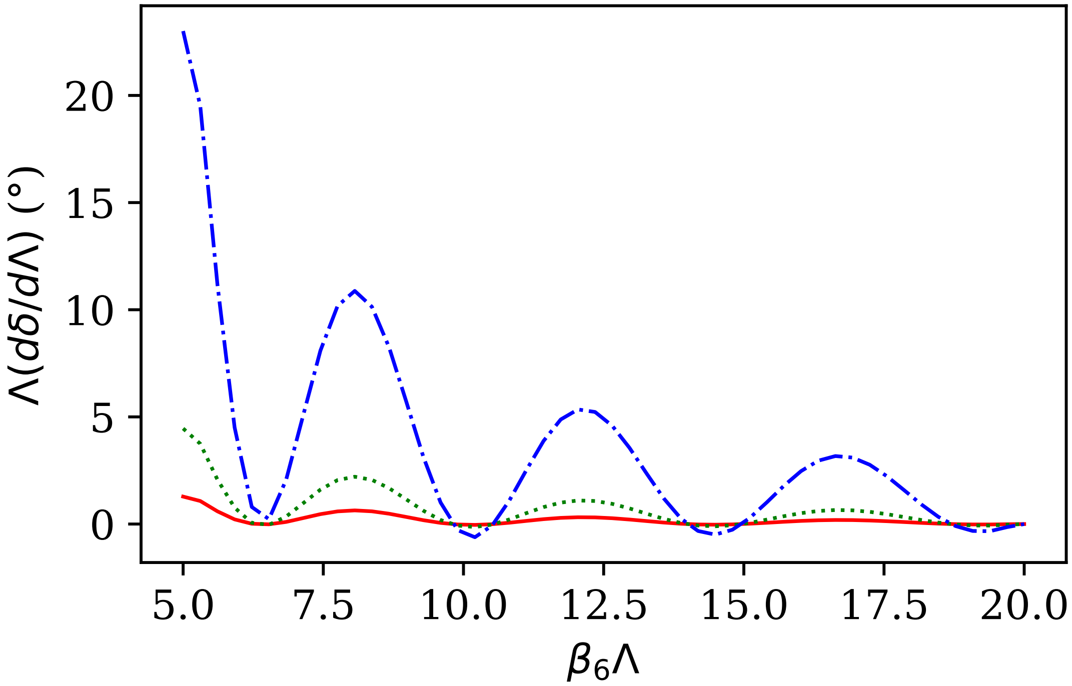

Figure 5.8: $\Lambda(d/d\Lambda)$ applied to the phase shifts at 0.001 (red, solid line), 0.01 (green, dotted line), and 0.1 (blue, dot-dashed line) Å^{-2} as a function of the dimensionless parameter $\beta_6\Lambda$.

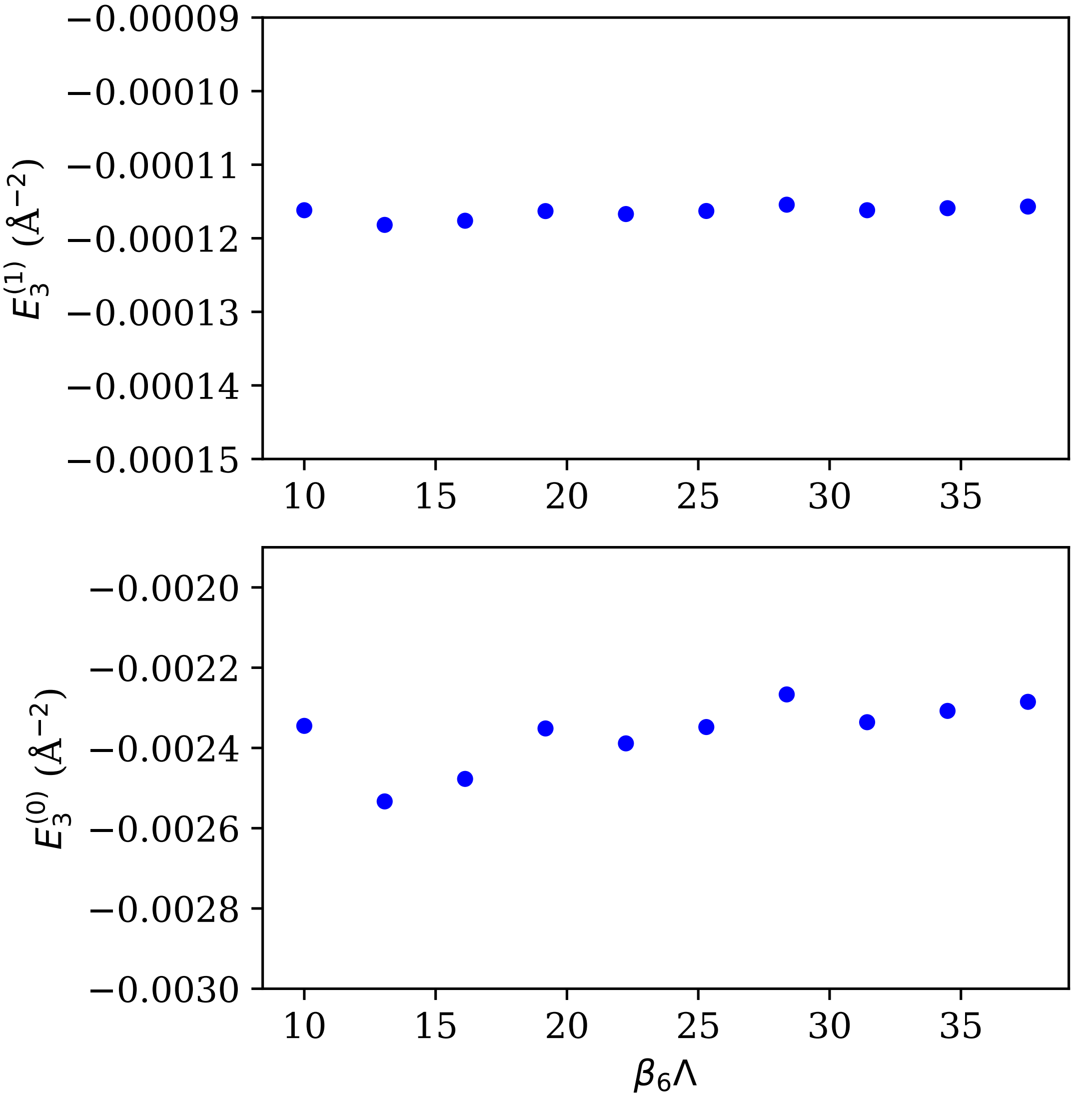

Figure 5.9: Trimer binding energies as a function of the dimensionless parameter $\beta_6\Lambda$.

the condition that $\beta_6 \gg R$. Fig. 5.9 shows the cutoff dependence of the three-body states found with our test parameters.

Finally, we compare our results for the universal predictions of κ_* and a_-. Fig. 5.10 shows the three-body states (through the trimer momentum variable) as a function of the inverse scattering length. The blue circles represent the three-body states. For $a > 0$, there are two three-body states. As $a \to \infty$, the ratio of these states increases, presumably toward the expected ratio of ≈ 515 as shown in Fig. 5.11. The agreement between the crossing of the deep, three-body states and the y-axis at the universal prediction of κ_* in Fig. 5.10

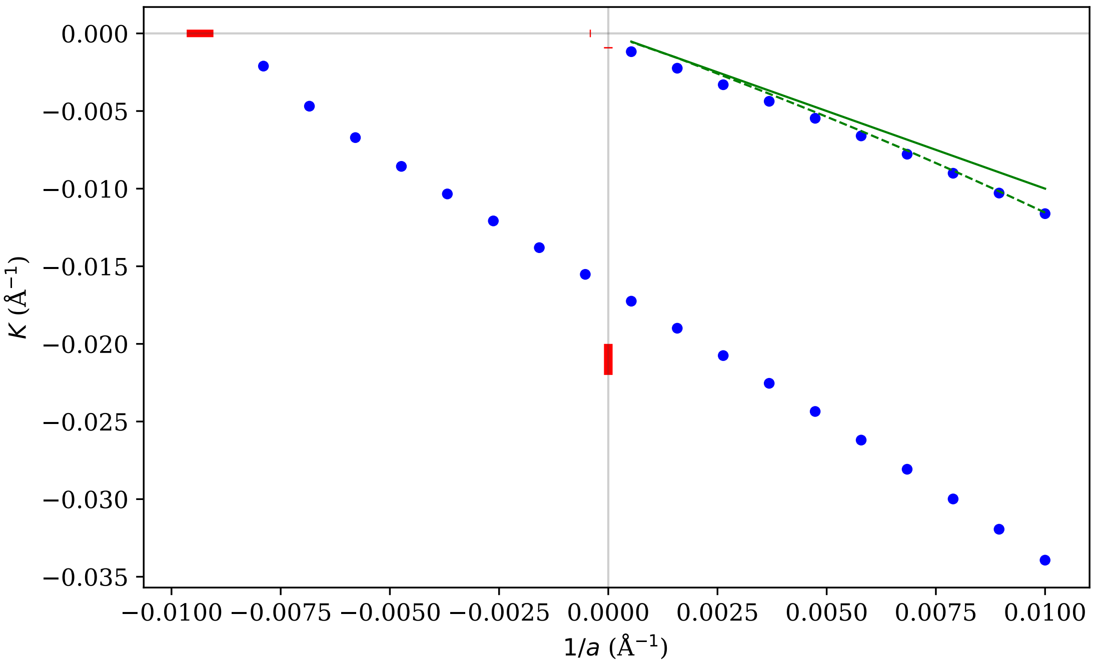

Figure 5.10: Trimer momentum variable (Eq. (5.12)) as a function of the inverse, two-body scattering length. Blue circles are the calculated states where $\beta_6/R = 0.1$. The green, solid line is $1/a$. The green, dashed line is two-body, binding momentum. The short, red lines are the universal predictions for van der Waals systems.

is promising but incomplete. Likewise for the agreement between the disappearance of the three-body states and the universal predictions for $1/a_-$. Right now, we are only capable of including s-waves in the three-body, binding energy calculation. Including $d-d$ coupling should decrease the binding energy, pulling the blue circles downward and hopefully matching up much better with the universal predictions (Eq. (5.7) and (5.9)).

5.3.2 ^{4}He

In Section 5.3.1, we proposed a LO effective theory that includes a long-range van der Waal tail and a short-distance, contact-like counterterm. We presented stable and converged results when applying test parameters to this potential. Here, we will apply the same procedure to a realistic system. The system of interest is a cold gas of neutral ^{4}He atoms.

There are several potentials that have been finely tuned and rigorously tested against the ^{4}He dimer binding energy, two-body scattering length, trimer binding energies, and

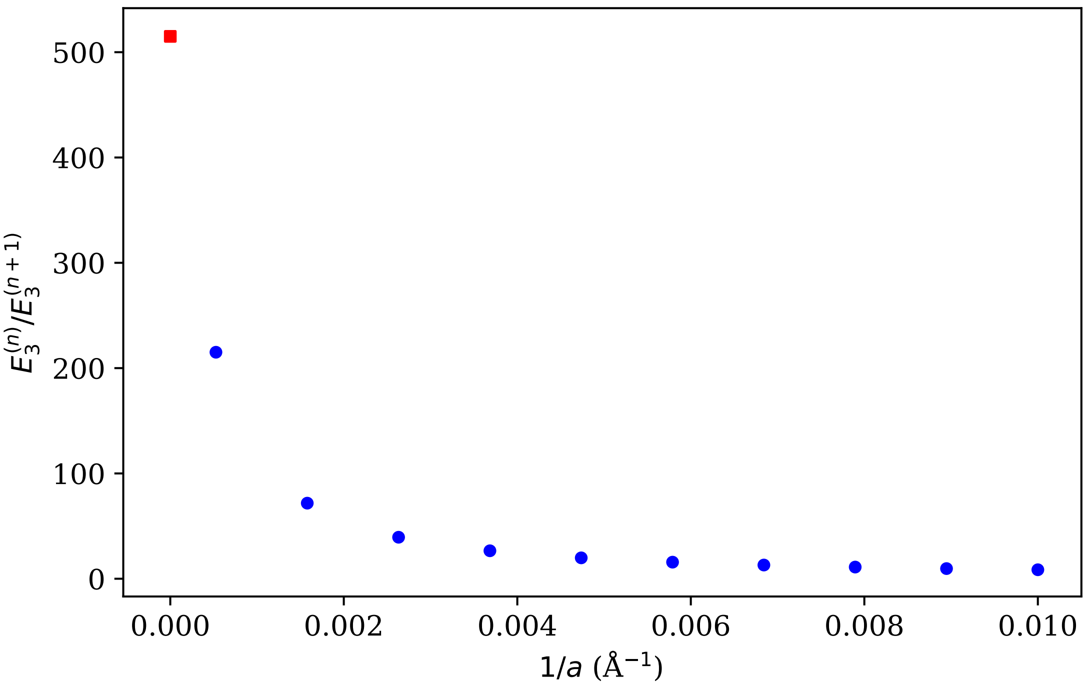

Figure 5.11: The ratio of the deeper three-body binding energy to the more shallow three-body binding energy as a function of the inverse scattering length. The blue circles are the calculation. The red square is the universal prediction at the unitary limit $1/a = 0$.

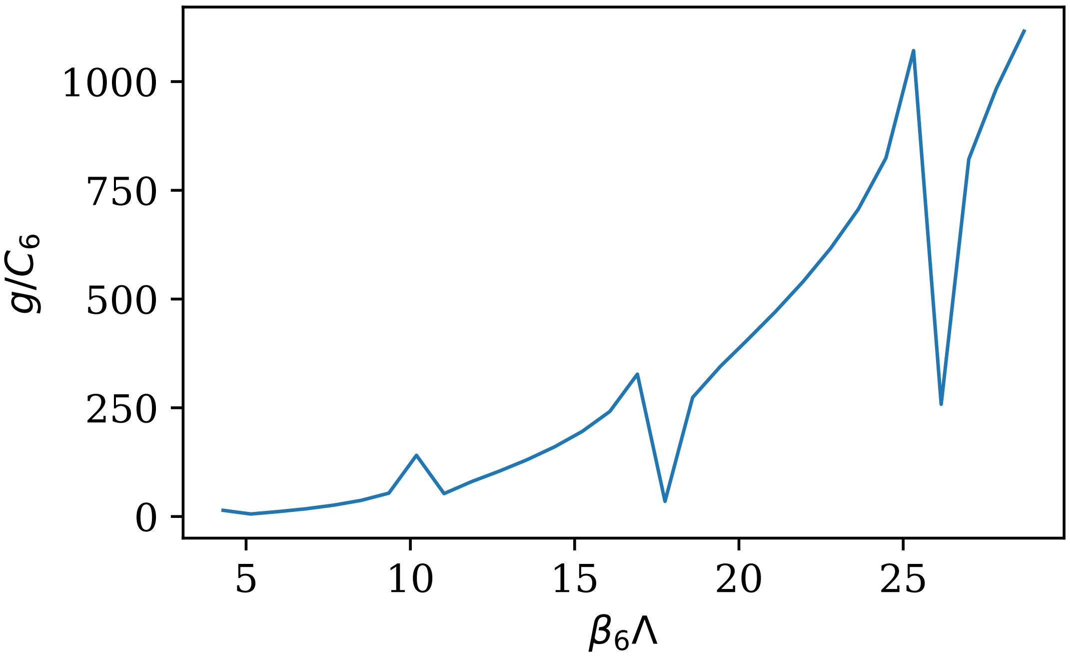

Figure 5.12: RG flow of the two-body counterterm found by tuning the shallow, two-body state to 1.31mK.

atom-dimer scattering length [10]. We will compare our vdWEFT approach to the LM2M2 potential. This potential has 17 parameters corresponding to 6 different terms, the most long-range of which is the $1/r^6$ tail. We take the coefficient of that vdW tail and add the same contact-like counterterm with its single, tunable parameter, g.

To start, we fix the single, two-body, bound state at $B_2 = 1.31$ mK. This gives the RG flow shown in Fig. 5.12. Initially, there exists only a single, two-body state. Another spurious bound state enters the spectrum almost immediately as R decreases. Eventually, a third bound state enters a little above $\beta_6/R = 5$. As in Ch. 3, these states are beyond the energy range in which our EFT claims accuracy and thus are too deep to be considered physical.

Having fixed the bound state, we calculate the two-body scattering length and present the results in Fig. 5.13. The figure shows the two-body scattering converging nicely with respect to β_6/R, and the value to which it converges matches up well with known LM2M2 result of 100Å. One may suspect however that this is simply a result of the universal relationship

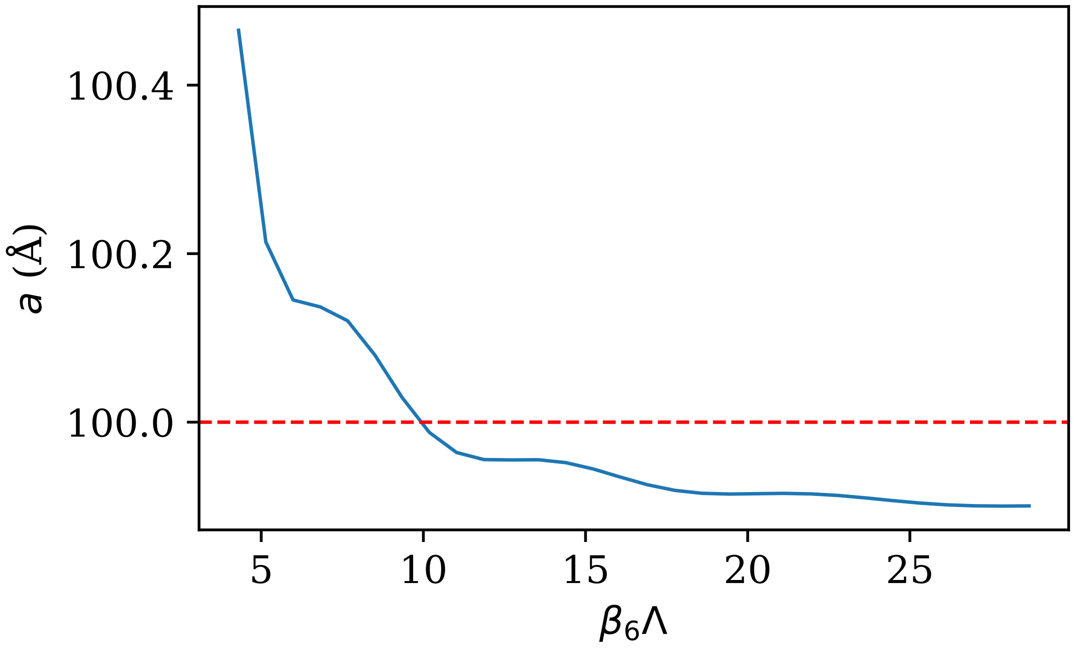

Figure 5.13: Two-body scattering length as the short-distance cutoff, R, decreases. The solid, blue line is our calculation. The dashed, red line is the LM2M2 result.

between a shallow bound state and a large scattering length. A better test of vdWEFT is the effective range.

The effective range cutoff dependence is shown in Fig. 5.14. Like the scattering length, the effective range converges with respect to $\beta_6\Lambda$, and the value to which is converges to matches up very well with the LM2M2 result of 7.33Å. The reason we are able to match this value so well is because we include the long-range vdW tail. If we were to employ a separable interaction of the form

$$\tilde{V}(p,k) = ge^{-(p/\Lambda)^2}e^{-(k/\Lambda)^2}, \tag{5.19}$$

and tune the bound state, we would reproduce the scattering length because it is related to the shallow bound state. The more shallow that state becomes, the more accurate Eq. (5.18) is. However, we would require another parameter to tune the effective range. As shown by Gao [21], once the scattering length is set, the van der Waals tail fixes the effective range.

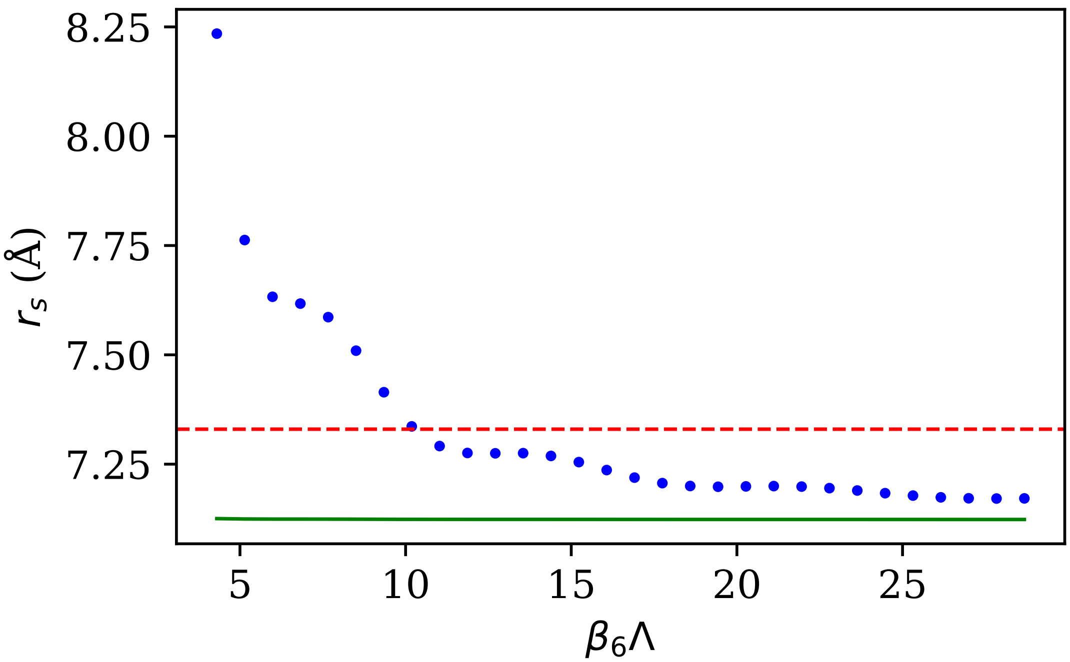

Figure 5.14: ^{4}He$-^4$He effective range as the high-momentum (short-distance) cutoff, Λ, increases. The blue dots are the calculation. The solid, green line represents the predicted values per Eq. (5.4). The dashed, red line is the LM2M2 result.

This makes our theory particularly powerful in that it captures more information about the system with very little input.

As the effective range is known from the scattering length via the short-range K-matrix, so also should any deeper two-body states that are shallow enough to be associated with the van der Waals tail. Fig. 5.15 shows the deeper state meeting up with the $\chi_{l=0}$ intersection as β_6/R increases, further establishing the reach of our theory's predictive power.

The LM2M2 is also finely tuned to reproduce two three-body states. The three-body spectrum found with our potential and the comparison to the LM2M2 results is shown in Fig. 5.16. The excited, three-body state differs by more than 10%, and the ground, three-body state differs by more than 20%. We attribute our inaccuracy to the current limitations of our calculation not the theory. We have computed the three-body binding energies using s-wave states. However, two d-wave states can couple to a final s-wave state. As mentioned in Section 5.3.1, our three-body binding energy calculations are currently limited to s-waves. We strongly suspect that once the $d-d$ coupling is included, our values will be much closer.

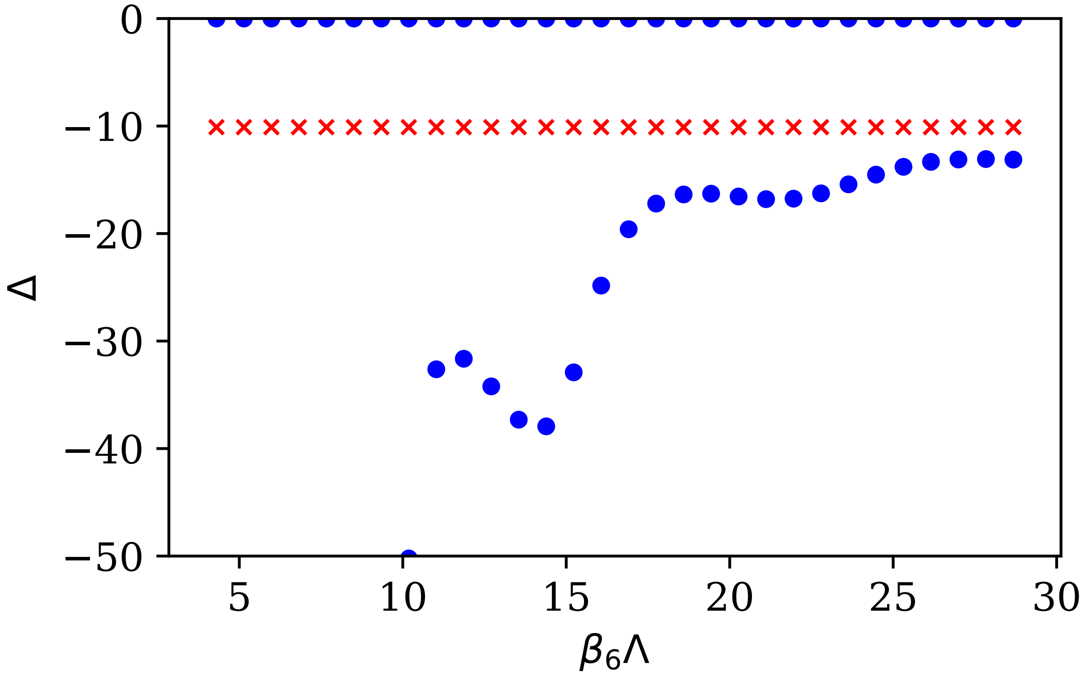

Figure 5.15: ^{4}He two-body binding energies as a function of the dimensionless parameter $\beta_6\Lambda$. The blue circles are the calculated energies. The red x's correspond to the predicted value via the intersections of $K^0_0(0)$ and the $\chi_{l=0}$ function.

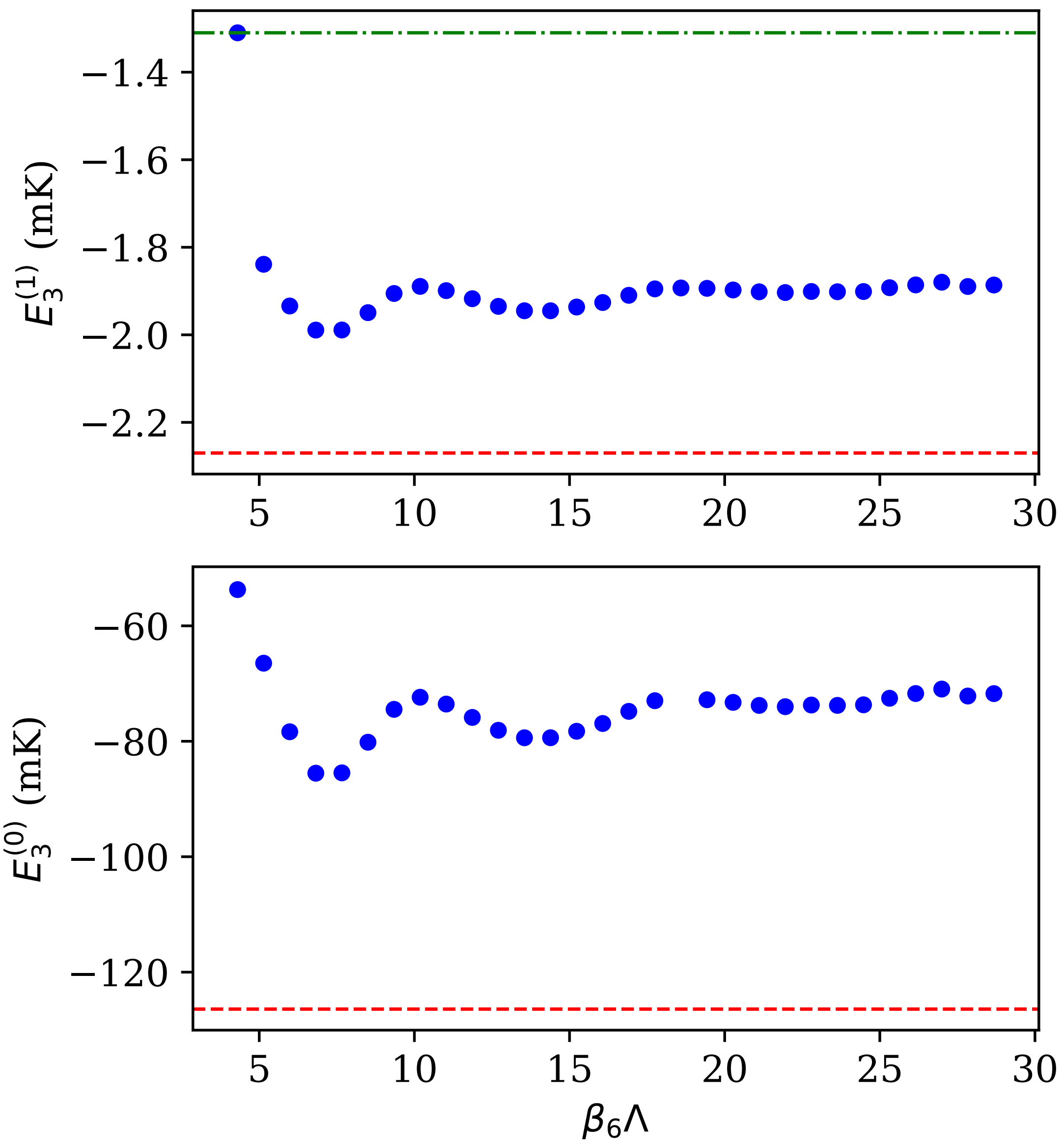

Figure 5.16: ^{4}He trimer binding energies as a function of the dimensionless parameter $\beta_6\Lambda$. The blue circles are the calculated energies. The red, dashed line is the energy from the LM2M2 potential [10].

5.4 Summary and Outlook

We have constructed a LO effective theory composed of a long-range van der Waals tail and a short-distance, contact-like counterterm. We have tested this theory on a simple system and demonstrated that results the results are consistent with known aspects of van der Waals universality. We have also applied our vdWEFT to a realistic system of ^{4}He atoms and compared it against an accurate, well-accepted model of the ^{4}He-^{4}He interaction.

The primary outstanding discrepancy between vdWEFT and the LM2M2 is the three-body spectrum. The three-body states calculated with vdWEFT are too shallow. We have proposed that this is due solely to our current lacking ability to perform calculations with higher partial waves as our current three-body codes employ s-waves only. In the future, we will include partial waves with $l > 0$, most likely resolving the discrepancy.

There is also a discrepancies between our values for κ_* and a_- and the predicted, universal relations. Again, we anticipate that including higher partial waves will account for these discrepancies.

Beyond confirming known results and improving their accuracy, we also intend to investigate the β_6 dependency of other observables such as decay widths. This requires that we significantly advance our three-body scattering code. First, we need to include higher partial waves. Second, we need to either implement the removal of multiple, spurious bound states in the scattering code or refine our implementation of the complex energy method.

Chapter 6

Numerical Implementation

The majority of the work presented in this thesis was based on numerical calculations. These calculations were implemented using Mathematica, Python, and C++. In this chapter, we will summarize how those implementations were constructed.

6.1 General Remarks

6.1.1 Frame of Reference

We perform our calculations in the center-of-mass system where the center-of-mass momentum is zero. The quantity of interest is then the relative momentum of the two particles

$$\vec{p} = \frac{1}{2}(\vec{p}_2 - \vec{p}_1). \tag{6.1}$$

We perform a partial-wave decomposition such that

$$\langle \vec{p} | p\, lm \rangle = \frac{\delta(|\vec{p}| - p)}{p^2} Y_l^m(\theta, \phi), \tag{6.2}$$

where θ and ϕ correspond to the direction of $\vec{p}$.

The normalization of the partial-wave states is

$$\langle p\, lm | p' l' m' \rangle = \frac{\delta(p - p')}{p^2} \delta_{l,l'} \delta_{m,m'}.$$

6.1.2 Numerical Integration

Most of the calculations performed in this thesis relied on numerical integration to some extent. For this we rely heavily on Gaussian quadrature. For cases where the integration was performed over the interval [-1, 1], we either extract the abscissa and weights from a library (e.g. SciPy) or calculate them via the method described in Section 4.6.1 of Numerical Recipes [50].

For cases where the integration was performed over the interval [0, Λ], we use at most two simple variable transformations. First, we shift and extend (or contract) the abscissa (x_i) and weights (w_i) on the interval [-1, 1] to the interval $[a, b]$ by

$$\begin{aligned} x_i &\to [(b-a)/2]x_i, \\ x_i &\to [(b+a)/2]x_i, \\ w_i &\to [(b-a)/2]w_i. \end{aligned} \tag{6.3}$$

Second, when the function being integrated has much more varying behavior at the low end of the interval than the high end, we redistribute the abscissa such that the density of points at lower values of the range is much higher than at higher values of the range. Specifically, consider the variable transformation

$$y = \log x + 1. \tag{6.4}$$

If the integration is to be carried out over the interval $x = [a, b]$, obtaining Gauss-Legendre abscissa and weights on the interval $y = [\log(a+1), \log(b+1)]$ and performing the transformation

$$\begin{aligned} x_i &= e^{y_i} - 1, \\ w_{x,i} &= e^{y_i} w_{y,i}. \end{aligned} \tag{6.5}$$

creates an integration mesh that packs a majority of the points at the low end of the interval. This dramatically improves the convergence of the integration of functions whose low-end behavior is much more complex. The momentum-space potentials employed in this thesis by design act more strongly at low momentum or low momentum transfer than at high momentum. Thus the procedure described in this section proved very useful.

6.2 Two-Body Calculations

Two types of two-body calculations were performed in this thesis: binding energies and scattering amplitudes. The binding energy calculations are described in Section 6.2.1, and the scattering calculations are described in Section 6.2.2

6.2.1 Binding Energies

The two-body binding energy calculations dealt with the solution of the discretized Schrödinger equation — eigenvalue problems. In momentum space, the Schrödinger equation is

$$(\frac{\hat{p}^2}{2m} + \hat{V})\,|\psi\rangle = E\,|\psi\rangle\,. \tag{6.6}$$

Projecting onto the partial-wave-project, momentum state, $\langle pl|$, we have

$$\langle pl|\,(\frac{\hat{p}^2}{2m} + \hat{V})\,|\psi\rangle = E\,\langle pl|\psi\rangle\,. \tag{6.7}$$

Inserting the complete set of states

$$\sum_l \int_0^\infty dqq^2\,|ql\rangle\,\langle ql| = 1, \tag{6.8}$$

we get

$$\left(\frac{p^2}{2m}\delta_{ll'} + \sum_{l'}\int_0^\infty dqq^2\,\langle pl|\hat{V}|ql'\rangle\right)\langle ql'|\psi\rangle = E\,\langle pl|\psi\rangle\,. \tag{6.9}$$

Considering $l = l' = 0$, we reduce this to

$$\left(\frac{p^2}{2m} + \int_0^\infty dqq^2\,\langle p|\hat{V}|q\rangle\right)\langle q|\psi\rangle = E\,\langle pl|\psi\rangle\,. \tag{6.10}$$

Now, via the method described in Section 6.1.2, we discretize the integral

$$\int_0^\infty dq q^2 \approx \sum_{j=0}^{N-1} w_j q_j^2. \tag{6.11}$$

We arrive at

$$\sum_{j=0}^{N-1} \left[\frac{p_i^2}{2m} \delta_{ij} + w_j q_j^2 V(p_i, q_j) \right] \psi(q_j) = E\psi(p_i). \tag{6.12}$$

Recognizing that everything inside the square brackets is a matrix, we are left with

$$\sum_{j=0}^{N-1} H_{ij} \psi_j = E \psi_i \tag{6.13}$$

where H_{ij} is a real matrix, the eigenvalues and eigenvectors of which can be found with the use of library routines (e.g. NumPy's `eig` function or GSL's `gsl_eigen_symmv` and `gsl_eigen_nonsymm`).

Another way to formulate the problem is to rearrange the Schrödinger equation such that

$$\begin{aligned} \hat{V} \left|\psi\right\rangle &= \left[E - \hat{p}^2/(2m)\right] \left|\psi\right\rangle \\ \hat{V} \left|\psi\right\rangle &= \hat{G}_0^{-1}(E) \left|\psi\right\rangle \\ \hat{G}_0(E) \hat{V} \left|\psi\right\rangle &= \left|\psi\right\rangle \\ \left[\hat{1} - \hat{G}_0(E)\hat{V}\right] \left|\psi\right\rangle &= 0 \\ \left[\hat{1} - \hat{K}(E)\right] \left|\psi\right\rangle &= 0. \end{aligned} \tag{6.14}$$

Projecting onto the same $\langle p_i|$ state and inserting the same complete set of states as before allows us to construct the matrix

$$\mathcal{K}_{ij} \equiv \delta_{ij} - \frac{w_j q_j^2 V(p_i, q_j)}{E - p_i^2/2m}, \tag{6.15}$$

which by Eq. (6.14) requires that $\det \mathcal{K}_{ij} = 0$. As a function of the energy E, the determinant tends to be a fairly smooth function, making the call to a simple root-finding algorithm (e.g. SciPy's `fsolve` or `newton`) quick and highly effective.

6.2.2 Scattering

Uncoupled Channels Two-body scattering is governed by the Lippmann-Schwinger equation as first stated in Section 3.2.3. For the convenience of the reader, we repeat it here. For uncoupled channels we have

$$t(p, q_0; E) = \tilde{V}(p, q_0) + \int_0^\infty dq\, q^2 \, \frac{\tilde{V}(p, q)\, t(q, q_0; E)}{E + i\epsilon - q^2/m}. \tag{6.16}$$

Again, we discretize the integral with Gauss-Legendre abscissa and weights with a finite upper limit Λ, but the added complication here is the $i\epsilon$ prescription. Two-body scattering happens at positive energy. Therefore, there is a pole in the integral of Eq. (6.16) at $q = \sqrt{mE}$. Using the identity

$$\int \frac{f(x)}{g(x) + i\epsilon} = \mathcal{P} \int \frac{f(x)}{g(x)} - i\pi \int f(x)\delta(g(x)) \tag{6.17}$$

we now have a principal value integral (denoted by $\mathcal{P}$)

$$\begin{aligned} t(p, q_0; E) = \tilde{V}(p, q_0) &+ \mathcal{P} \int_0^\Lambda dq\, q^2 \, \frac{\tilde{V}(p, q)\, t(q, q_0; E)}{E - q^2/m} \\ &- i\pi \int_0^\Lambda dq\, q^2 \, \tilde{V}(p, q)\, t(q, q_0; E)\delta(E - q^2/m). \end{aligned} \tag{6.18}$$

The incident energy $E = q_0^2/m$, and the δ function is evaluated as

$$\delta(q_0^2/m - q^2/m) = \frac{m\delta(q_0 - q)}{2q_0}, \tag{6.19}$$

such that Eq. (6.18) becomes

$$\begin{aligned} t(p, q_0; E) = \tilde{V}(p, q_0) &+ \mathcal{P} \int_0^\Lambda dq\, q^2 \, \frac{\tilde{V}(p, q)\, t(q, q_0; E)}{E - q^2/m} \\ &- i\pi \frac{m q_0}{2} \tilde{V}(p, q_0)\, t(q_0, q_0). \end{aligned} \tag{6.20}$$

Now, all we have left to do is deal with the principal value prescription. We use a technique called pole subtraction. We modify the first integral in Eq. (6.20)

$$\mathcal{P}\int_0^\Lambda dq\, q^2\, \frac{\tilde{V}(p,q)\, t(q,q_0;E)}{E-q^2/m} = \int_0^\Lambda dq\, \frac{q^2\tilde{V}(p,q)\, t(q,q_0;E) - q_0^2\tilde{V}(p,q_0)\, t(q_0,q_0;E)}{E-q^2/m} + \int_0^\Lambda dq\, \frac{q_0^2\tilde{V}(p,q_0)\, t(q_0,q_0;E)}{E-q^2/m} \tag{6.21}$$

The first integral on the right-hand side of Eq. (6.21) is now zero at $q = q_0$. The subtracted term in that integral is calculated numerically

$$\begin{aligned}\int_0^\Lambda dq\, \frac{q_0^2\tilde{V}(p,q_0)\, t(q_0,q_0;E)}{E-q^2/m}, &\approx q_0^2\tilde{V}(p,q_0)\, t(q_0,q_0;E)\sum_j w_j \frac{1}{E-q^2/m}, \\ &= m q_0^2\tilde{V}(p,q_0)\, t(q_0,q_0;q_0^2/m)\sum_j w_j \frac{1}{q_0^2-q^2}, \\ &\equiv m q_0^2\tilde{V}(p,q_0)\mathcal{N} t(q_0,q_0;q_0^2/m)\end{aligned} \tag{6.22}$$

to offset any numerical inconsistencies contributed by the mesh spacing.

The second integral on the right-hand side of Eq. (6.21) can be done analytically, giving

$$\begin{aligned}\int_0^\Lambda dq\, \frac{q_0^2\tilde{V}(p,q_0)\, t(q_0,q_0;E)}{E-q^2/m} &= q_0^2\tilde{V}(p,q_0)\, t(q_0,q_0;E)\int_0^\Lambda dq\, \frac{1}{E-q^2/m} \\ &= q_0^2\tilde{V}(p,q_0)\, t(q_0,q_0;E)\int_0^\Lambda dq\, \frac{1}{E-q^2/m}\end{aligned} \tag{6.23}$$

Now,

$$\begin{aligned}\int_0^\Lambda dq \frac{1}{E-q^2/m} &= \int_0^\Lambda dq \frac{m}{q_0^2-q^2} \\ &= \int_0^\Lambda dq \frac{m}{(q_0-q)(q_0+q)} \\ &= \frac{m}{2q_0}\int_0^\Lambda dq\left(\frac{1}{q_0-q}+\frac{1}{q_0+q}\right) \\ &= \frac{m}{2q_0}\left(\int_0^\Lambda dq \frac{1}{q_0-q} + \log\left(\frac{q_0+\Lambda}{q_0}\right)\right).\end{aligned} \tag{6.24}$$

The remaining integral is now split into two intervals

$$\int_0^\Lambda dq \frac{1}{q_0 - q} = \int_0^{2q_0} dq \frac{1}{q_0 - q} + \int_{2q_0}^\Lambda dq \frac{1}{q_0 - q}, \tag{6.25}$$

where the first is an odd integrand evenly integrated about the pole leaving the result as zero. The second integral results in

$$\int_{2q_0}^\Lambda dq \frac{1}{q_0 - q} = \log\left(\frac{q_0}{\Lambda - q_0}\right). \tag{6.26}$$

Collecting all of the terms that multiply the on-shell amplitude, $t(q_0, q_0)$, we have

$$\mathcal{C}\, t(q_0, q_0; q_0^2/m) = \frac{mq_0}{2}\tilde{V}(p, q_0)\left[2q_0\mathcal{N} + \log\left(\frac{\Lambda + q_0}{\Lambda - q_0}\right) - i\pi\right] t(q_0, q_0; q_0^2/m)$$

In order to solve for the on-shell amplitude, we must include q_0 explicitly in the momentum mesh over which the integration. However, we do not want to include the point in the sum. We exclude it by appending q_0 to the momentum mesh but requiring its corresponding weight to be zero.

In discretized form where

$$\begin{aligned} p &\to p_i \\ q &\to q_j \\ \tilde{V}(p, q) &\to \tilde{V}_(p_i, q_j) = \tilde{V}_{ij} \\ t(p, q) &\to t_(p_i, q_j) = t_{ij} \\ \int dq &\to \sum_{j=0}^{N} w_j \end{aligned} \tag{6.27}$$

with p_i and q_j representing a discrete momentum mesh

$$[q_0, q_1, \ldots, q_{N-1}, q_0].$$

and w_j representing the discrete values

$$[w_0, w_1, \ldots, w_{N-1}, 0].$$

we have

$$[\delta_{ij} - K_{ij}]\, t_{ij} = \tilde{V}_{ij}. \tag{6.28}$$

K_{ij} for $j < N$ is

$$K_{ij} = \frac{m\, w_j q_j^2 \tilde{V}_{ij}}{q_0^2 - q_j^2}$$

and

$$K_{ij} = \frac{mq_0}{2}\tilde{V}(p_i, q_j)\left[2q_0\mathcal{N} + \log\left(\frac{\Lambda + q_0}{\Lambda - q_0}\right) - i\pi\right]$$

for $j = N$.

What we have arrived at is a matrix-vector multiplication of the form

$$A\boldsymbol{x} = \boldsymbol{b},$$

where matrix A is known and vector $\boldsymbol{b}$ is known. Solving for $\boldsymbol{x}$ requires the calculation of A^{-1} which is facilitated by the computation of the LU factorization of A. The result, $\boldsymbol{x}$, are t-matrix amplitudes. The last element of vector $\boldsymbol{x}$ is the on-shell amplitude from which we calculate the partial wave amplitude by

$$f(q_0) = -\frac{m\pi}{2} t(q_0, q_0; q_0^2/m),$$

which is related to the phase shift by

$$f(k) = \frac{1}{k\cot\delta - ik}.$$

Coupled Channels For coupled channels we have

$$t_{\alpha\alpha'}(p, q_0) = \tilde{V}_{\alpha\alpha'}(p, q_0) + \sum_{\alpha''}\int_0^\infty dq\, q^2\, \frac{\tilde{V}_{\alpha\alpha''}(p, q) t_{\alpha''\alpha'}(q, q_0)}{E + i\epsilon - q^2/m}, \tag{6.29}$$

which is solved in a similar fashion. Consider a potential that is not diagonal in angular momentum such that $l = 0$ couples to $l = 2$. We will call $\alpha = 0$ and $\alpha' = 2$. If we wish to calculate the phase shift between two s-wave states, we have

$$t_{00} = v_{00} + v_{00}G_0t_{00} + v_{02}G_0t_{20},$$

which requires the solution of t_{20} which comes from

$$t_{20} = v_{20} + v_{20}G_0t_{00} + v_{22}G_0t_{20}.$$

The equations are coupled and must be solved simultaneously. We construct the matrix

$$\begin{pmatrix} v_{00} & v_{20} \\ v_{20} & v_{22} \end{pmatrix}$$

such that we have

$$\begin{pmatrix} t_{00} \\ t_{20} \end{pmatrix} = \begin{pmatrix} v_{00} \\ v_{20} \end{pmatrix} + \begin{pmatrix} v_{00} & v_{02} \\ v_{20} & v_{22} \end{pmatrix} G_0 \begin{pmatrix} t_{00} \\ t_{20} \end{pmatrix}$$

The Stapp parameterization given by Eq. (4.9) requires not only t_{00} and t_{20}, but t_{22} which comes from the solution of the similar coupled equation

$$\begin{pmatrix} t_{02} \\ t_{22} \end{pmatrix} = \begin{pmatrix} v_{02} \\ v_{22} \end{pmatrix} + \begin{pmatrix} v_{00} & v_{02} \\ v_{20} & v_{22} \end{pmatrix} G_0 \begin{pmatrix} t_{00} \\ t_{22} \end{pmatrix}$$

Where A was an $N \times N$ matrix in the uncoupled channel case, there are now two $4N \times 4N$ matrices that need to be constructed. And each channel must implement the pole subtraction described above.

6.3 Three-Body Calculations

We work in Jacobi coordinates where

$$\vec{p} = \frac{1}{2}(\vec{p}_2 - \vec{p}_1) \tag{6.30}$$

$$\vec{q} = \frac{1}{3}(2\vec{p}_3 - \vec{p}_2 - \vec{p}_1) \tag{6.31}$$

$$\tag{6.32}$$

using partial-wave-projected states with the same normalization requirements as in Section 6.2.

6.3.1 Binding Energies

To calculate s-wave, three-body bound states, as mentioned in Section 3.2.4, we solve [28]

$$\langle pq|\psi\rangle = \frac{1}{E - p^2/m - 3q^2/4m}\int_0^\infty dq' q'^2 \int_{-1}^{1} dx\, t(p, \pi_1; E - 3q^2/4m)\, \langle \pi_2 q'|\psi\rangle \ , \tag{6.33}$$

where ψ represents a single, arbitrary Faddeev component, t is the two-body t-matrix, $\pi_1 = \sqrt{q^2/4 + (q')^2 + qq'x}$, and $\pi_2 = \sqrt{q^2 + (q')^2/4 + qq'x}$.

Because we are looking for bound states, the E values are negative. Therefore, the only poles we have to concern ourselves with are the poles in the two-body t-matrix at the two-body bound state energies. As long as we are looking for proper, normalizable three-body states — states that lie beneath the deepest two-body state, we can avoid those poles entirely. The task of discretizing Eq. (6.33) is greatly simplified. We simply take

$$\begin{aligned} p &\to p_i, \\ q &\to q_j, \\ q'' &\to q_l, \\ x &\to x_n, \end{aligned} \tag{6.34}$$

and rewrite Eq. (6.33) as

$$\psi(p_i, q_j) = \frac{1}{E - p_i^2/m - 3q_j^2/4m} \sum_{l,n} w_l q_l^2 w_n t(p, \pi_{1,jln}; E - 3q_j^2/4m) \psi(\pi_{2,jln}, q_l) \ . \tag{6.35}$$

One of the difficulties of solving this equation is dealing with the off-grid values of p at which ψ must be evaluated. We solve the problem with splines, interpolating ψ without actually knowing the values of ψ. The splines we employ are derived very clear by Glöckle et al. [26]. Their function is such that

$$\psi(\pi_{2,jln}, q_l) \approx \sum_k S_k(\pi_{2,jln}) \psi(p_k, q_l).$$

Now, we have

$$\psi(p_i, q_j) = \frac{1}{E - p_i^2/m - 3q_j^2/4m} \sum_{l,n,k} w_l q_l^2 w_n t(p, \pi_{1,jln}; E - 3q_j^2/4m) S_k(\pi_{2,jln}) \psi(p_k, q_l) \ ,$$

and the summation over n can be carried out numerically, leaving

$$\psi(p_i, q_j) = \frac{1}{E - p_i^2/m - 3q_j^2/4m} \sum_{l,k} w_l q_l^2 A_{ijkl} \psi(p_k, q_l) \ .$$

Though ψ is a function of two variables, we flatten this into a single vector, create indices such that $I = jN + i$ and $J = lN + k$, simplifying the problem to

$$\psi_I = \sum_J K_{IJ}(E)\, \psi_J.$$

What we have reduced the problem to is a familiar eigenvalue problem where the determinant of $\delta_{IJ} - K_{IJ}(E)$ can be tuned to zero, providing the binding energies of the three-body states we are looking for.

6.3.2 Scattering

To further elaborate on the brief summary given in Section 3.2.5 over how we compute three-body phase shifts, we will provide more details in this section.

We begin with

$$T\left|\phi\right\rangle = tP\left|\phi\right\rangle + tPG_0T\left|\phi\right\rangle. \tag{6.36}$$

Our 3-body basis will be represented by

$$|pq\alpha\rangle \tag{6.37}$$

where α stands in for all of the relevant quantum numbers. Their normalization is such that

$$\langle p'q'\alpha'|pq\alpha\rangle = \frac{\delta(q-q')}{qq'}\frac{\delta(p-p')}{pp'}\delta_{\alpha\alpha'}. \tag{6.38}$$

Once we insert a few sets of states and project onto $\langle pq\alpha|$, we arrive at

$$\begin{aligned}\langle pq\alpha|T|\phi\rangle = \langle pq\alpha|tP|\phi\rangle +& \\ &\sum_{\alpha'}\sum_{\alpha''}\int_0^\infty dq'q'^2\int_{-1}^{1}dx\,\frac{\tilde{t}_{\tilde{\alpha}\tilde{\alpha}'}(p,\pi_1,E-3q^2/4m)}{\pi_1^{l'}} \\ &G_{\alpha'\alpha''}(qq'x)\frac{1}{E+i\epsilon-q^2/m-q'^2/m-qq'x/m} \\ &\times\frac{\langle\pi_2q'\alpha''|T|\phi\rangle}{\pi_2^{l''}}\end{aligned} \tag{6.39}$$

where

$$\langle pq\alpha|tP|\phi\rangle = \sum_{\alpha'}\int_{-1}^{1}dx\,\tilde{t}_{\tilde{\alpha}\tilde{\alpha}'}(p,\pi_1,E-3q^2/4m)\sum_{\alpha''\alpha_d}G_{\alpha'\alpha''}(q,q_0,x)\frac{\varphi_{l''}(\pi_2)}{\pi_2^{l''}}C_{\alpha''}^{m_dm_N} \tag{6.40}$$

with

$$C_{\alpha''}^{m_dm_N} = \sqrt{\frac{2\lambda+1}{4\pi}}C(\lambda\frac{1}{2}I,0m_N)C(1IJ,m_dm_N). \tag{6.41}$$

What we have now is Eq. (165) of [27]. We only study s-wave bosons in this thesis, so we drop the α notation entirely. Eq. (6.39) simplifies to

$$\begin{aligned}\langle pq|T|\phi\rangle = \langle pq|tP|\phi\rangle + \int_0^\infty dq' q'^2 \int_{-1}^{1} dx\, t(p,\pi_1,E-3q^2/4m) \\ \frac{1}{E+i\epsilon-q^2/m-q'^2/m-qq'x/m}\langle\pi_2 q'|T|\phi\rangle\end{aligned} \tag{6.42}$$

and (6.40) simplifies to

$$\begin{aligned}\langle pq|tP|\phi\rangle &= \int_{-1}^{1} dx\, t(p,\pi_1,E-3q^2/4m)\varphi(\pi_2) \\ &\approx \sum_n w_n^{(x)} t(p_i,\pi_1(q_j,q_0,x_n),E-3q_j^2/4m)\varphi(\pi_2(q_j,q_0,x_n))\end{aligned} \tag{6.43}$$

There is a pole in t at the 2-body binding energy, $E=-\gamma^2/m$. This is a problem because as we integrate over q', we are going to hit that pole as $\langle pq|T|\phi\rangle$ depends on every $\langle pq'|T|\phi\rangle$ (and consequently every $t(p,\pi_1,E-3q'^2/4m)$). In order to subtract this pole, we expose it explicitly with the substitutions

$$t(z) \equiv \frac{\hat{t}(z)}{z-\epsilon_d} \tag{6.44}$$

where $\epsilon_d \equiv -\gamma^2/m$.

The kernel term also benefits from a convenient definition (again from Glöckle)

$$\langle pq|T|\phi\rangle \equiv \frac{\langle pq|\hat{T}|\phi\rangle}{E+i\epsilon-3q^2/4m-\epsilon_d}. \tag{6.45}$$

Substituting these definitions into (6.42) and multiplying the entire equation by $(E-3q^2/4m-\epsilon_d)$, we obtain

$$\begin{aligned}\langle pq|\hat{T}|\phi\rangle = \langle pq|\hat{t}P|\phi\rangle + \int_0^\infty dq' q'^2 \int_{-1}^{1} dx\, t(p,\pi_1,E-3q^2/4m) \\ \frac{1}{E+i\epsilon-q^2/m-q'^2/m-qq'x/m}\frac{\langle\pi_2 q'|\hat{T}|\phi\rangle}{E+i\epsilon-3q'^2/4m-\epsilon_d}\end{aligned} \tag{6.46}$$

The driving term for (6.46) is simply (6.43) with $t \to \hat{t}$.

$|\phi\rangle$ is the incoming state. More explicitly, $|\phi\rangle = |\varphi q_0\rangle$. For $E = -\gamma^2/m + 3q_0^2/4m < 0$, we only have to deal with the on-shell pole which contributes to the q' integration.

First, let's simplify (6.46).

$$\begin{aligned} \frac{1}{E + i\epsilon - 3q'^2/4m - \epsilon_d} &\to \frac{1}{\epsilon_d + 3q_0^2/4m - 3q'^2/4m - \epsilon_d} \\ &= \frac{1}{(3/4m)(q_0^2 - q'^2)} \\ &= \frac{1}{(3/4m)(q_0 + q')(q_0 - q')} \\ &\to \frac{1}{(3/4m)(q_0 + q')(q_0 - q' + i\epsilon)} \end{aligned} \tag{6.47}$$

Now, (6.46) becomes

$$\begin{aligned} \langle pq|\hat{T}|\phi\rangle = \langle pq|\hat{t}P|\phi\rangle + \int_0^\infty dq' q'^2 \int_{-1}^1 dx\, t(p, \pi_1, \epsilon_d + (3/4m)(q_0^2 - q^2)) \\ \frac{1}{\epsilon_d + 3q_0^2/4m - q^2/m - q'^2/m - qq'x/m} \frac{\langle \pi_2 q'|\hat{T}|\phi\rangle}{(3/4m)(q_0 + q')(q_0 - q' + i\epsilon)} \\ = \langle pq|\hat{t}P|\phi\rangle + \frac{4m}{3}\int_0^\infty dq' q'^2 \int_{-1}^1 dx\, t(p, \pi_1, \epsilon_d + (3/4m)(q_0^2 - q^2)) \\ \frac{1}{\epsilon_d + 3q_0^2/4m - q^2/m - q'^2/m - qq'x/m} \frac{\langle \pi_2 q'|\hat{T}|\phi\rangle}{(q_0 + q')(q_0 - q' + i\epsilon)} \end{aligned} \tag{6.48}$$

We interpolate $\hat{T}$ with splines such that

$$\langle \pi_2 q'|\hat{T}|\phi\rangle \approx \sum_k S_k(\pi_2)\, \langle p_k q'|\hat{T}|\phi\rangle \tag{6.49}$$

Now, we have

$$\begin{aligned} \langle pq|\hat{T}|\phi\rangle = \langle pq|\hat{t}P|\phi\rangle + \frac{4m}{3}\sum_k \int_0^\infty dq' q'^2 \int_{-1}^1 dx\, t(p, \pi_1, \epsilon_d + (3/4m)(q_0^2 - q^2)) \\ \frac{S_k(\pi_2)}{\epsilon_d + 3q_0^2/4m - q^2/m - q'^2/m - qq'x/m} \frac{\langle p_k q'|\hat{T}|\phi\rangle}{(q_0 + q')(q_0 - q' + i\epsilon)} \\ = \langle pq|\hat{t}P|\phi\rangle + \sum_k \int_0^\infty dq' \int_{-1}^1 dx\, \frac{\mathcal{K}(p, q, x, p_k, q')\, \langle p_k q'|\hat{T}|\phi\rangle}{(q_0 - q')} \end{aligned} \tag{6.50}$$

where

$$\mathcal{K}(p,q,x,p',q') = \frac{4m}{3}\frac{q'^2\, t(p,\pi_1,\epsilon_d + (3/4m)(q_0^2 - q^2))}{\epsilon_d + 3q_0^2/4m - q^2/m - q'^2/m - qq'x/m}\frac{S_k(\pi_2)}{q_0 + q'}. \tag{6.51}$$

Before we discretize things, we'll express the pole subtraction of the q' integration explicitly. We have

$$\begin{aligned}\int_0^\infty dq' \frac{\mathcal{K}(p,q,x,p_k,q')}{q_0 - q' + i\epsilon}\,\langle p_k q'|\hat{T}|\varphi\, q_0\rangle =& \mathcal{P}\int_0^\infty dq' \frac{\mathcal{K}(p,q,x,p_k,q')}{q_0 - q'}\,\langle p_k q'|\hat{T}|\varphi\, q_0\rangle - \\ & i\pi \int_0^\infty dq' \mathcal{K}(p,q,x,p_k,q')\,\langle p_k q'|\hat{T}|\varphi\, q_0\rangle\, \delta(q' - q_0) \\ =& \mathcal{P}\int_0^\infty dq' \frac{\mathcal{K}(p,q,x,p_k,q')}{q_0 - q'}\,\langle p_k q'|\hat{T}|\varphi\, q_0\rangle - \\ & i\pi \mathcal{K}(p,q,x,p_k,q_0)\,\langle p_k q_0|\hat{T}|\varphi\, q_0\rangle\end{aligned} \tag{6.52}$$

To handle the principal value prescription numerically, we subtract the integrand at the pole and add it back analytically. We end up with

$$\begin{aligned}\int_0^\infty dq' \frac{\mathcal{K}(p,q,x,p_k,q')}{q_0 - q' + i\epsilon}\,\langle p_k q'|\hat{T}|\varphi\, q_0\rangle \approx \sum_l w_l \frac{\mathcal{K}(p,q,x,p_k,q_l)}{q_0 - q'}\,\langle p_k q_l|\hat{T}|\varphi\, q_0\rangle + \\ \mathcal{K}(p,q,x,p_k,q_0)\left[\log\left(\frac{q_0}{\Lambda - q_0}\right) - i\pi - \sum_{l'} \frac{w_{l'}^{(q)}}{q_0 - q_{l'}}\right]\langle p_k q_0|\hat{T}|\varphi\, q_0\rangle\end{aligned} \tag{6.53}$$

The kernel has two expressions. The integration expression looks like

$$\frac{4m}{3}\frac{w_n^{(x)} w_l^{(q)} q_l^2\, t_{ijln}}{\epsilon_d + 3q_0^2/4m - q_j^2/m - q_l^2/m - qq_l x/m}\frac{S_{jkln}}{q_0^2 - q_l^2} \tag{6.54}$$

where

$$
\begin{aligned}
& x \to x_n \left(\int_{-1}^{1} dx \approx \sum_n w_n^{(x)} \right) \\
& p \to p_i \\
& q \to q_j \\
& q' \to q_l \\
& t(p_i, \pi_1(q_j, q_l, x_n), \epsilon_d + (3/4m)(q_0^2 - q_j^2)) \to t_{ijln} \\
& S_k(\pi_2(q_j, q_l, x_n)) \to S_{jkln}.
\end{aligned}
\tag{6.55}
$$

The pole-subtraction term becomes

$$
\frac{4m\Delta}{3} \frac{q_0}{2} \frac{w_n^{(x)} \, t_{ijln} S_{jkln}}{\epsilon_d + 3q_0^2/4m - q_j^2/m - q_0^2/m - qq_0x/m} \tag{6.56}
$$

where

$$
\Delta = \log\left(\frac{q_0}{\Lambda - q_0}\right) - i\pi - \sum_{l'} \frac{w_{l'}^{(q)}}{q_0 - q_{l'}}. \tag{6.57}
$$

Physical observables require the scattering amplitude, given in Eq. (87) by Glöckle et al. [27]

$$
M_{m'_d m'_N m_d m_N}(\vec{q}', \vec{q}_0) \equiv -\frac{2}{3} m (2\pi)^2 \langle \phi' | U | \phi \rangle . \tag{6.58}
$$

For the case of s-wave bosons and considering only the *elastic* amplitude, we write

$$
M(\vec{q}_0, \vec{q}_0) \equiv -\frac{2}{3} m (2\pi)^2 \langle \phi | U | \phi \rangle . \tag{6.59}
$$

U is defined by Eq.(74) of [27]

$$
U = PG_0^{-1} + PT + T_4. \tag{6.60}
$$

We do not include a three-body force, so we only have

$$
U = PG_0^{-1} + PT. \tag{6.61}
$$

Acting on the incoming state $|\varphi q_0\rangle$ and projecting onto the same outgoing state $\langle\varphi q_0|$, we get

$$\langle\varphi\, q_0|U|\varphi\, q_0\rangle = \langle\varphi\, q_0|PG_0^{-1}|\varphi\, q_0\rangle + \langle\varphi\, q_0|PT|\varphi\, q_0\rangle \tag{6.62}$$

The first term on the right-hand side becomes

$$\begin{aligned}
&\int\!\!\int dpp^2dqq^2\,\langle\varphi\, q_0|pq\rangle\,\langle pq|PG_0^{-1}|\varphi\, q_0\rangle\\
&=\int\!\!\int\!\!\int\!\!\int dpp^2dqq^2dp'p'^2dq'q'^2\,\langle\varphi\, q_0|pq\rangle\,\langle pq|P|p'q'\rangle\,\langle p'q'|G_0^{-1}|\varphi\, q_0\rangle\\
&=\int\!\!\int\!\!\int\!\!\int dpp^2dqq^2dp'p'^2dq'q'^2\varphi(p)\frac{\delta(q_0-q)}{qq_0}\,\langle pq|P|p'q'\rangle\,(E-p'^2/m-3q'^2/4m)\varphi(p')\frac{\delta(q_0-q')}{qq_0}\\
&=\int\!\!\int dpp^2dp'p'^2\varphi(p)\,\langle pq_0|P|p'q_0\rangle\,(E-p'^2/m-3q_0^2/4m)\varphi(p')\\
&=\int\!\!\int dpp^2dp'p'^2\varphi(p)\int_{-1}^{1}dx\frac{\delta(p-\pi_1)}{p\pi_1}\frac{\delta(p'-\pi_2)}{p\pi_2}(E-p'^2/m-3q_0^2/4m)\varphi(p')\\
&=\int_{-1}^{1}dx\varphi(\pi_1)(E-\pi_2^2/m-3q_0^2/4m)\varphi(\pi_2).
\end{aligned} \tag{6.63}$$

Here, the total energy $E=-\gamma^2/m+3q_0^2/4m$, so we end up with

$$\frac{-1}{m}\int_{-1}^{1}dx\,\varphi(\pi_1^{(0)})(\gamma^2+\pi_2^{(0)2})\varphi(\pi_2^{(0)}) \tag{6.64}$$

with $\pi_1^{(0)}=\sqrt{\frac{1}{4}q_0^2+q_0^2+q_0^2x}=q_0\sqrt{\frac{5}{4}+x}=\pi_2^{(0)}$ for the first term on the right-hand side of (6.62). I have added the (0) superscript to distinguish from the later use of π_1 and π_2.

Now, for the second term on the right-hand side of (6.62).

$$
\begin{aligned}
&\int\int dpp^2 dqq^2 \left\langle \varphi\, q_0 | pq \right\rangle \left\langle pq | PT | \varphi\, q_0 \right\rangle \\
&= \int\int\int\int dpp^2 dqq^2 dp'p'^2 dq'q'^2 \left\langle \varphi\, q_0 | pq \right\rangle \left\langle pq | P | p'q' \right\rangle \left\langle p'q' | T | \varphi\, q_0 \right\rangle \\
&= \int\int\int dpp^2 dp'p'^2 dq'q'^2 \varphi(p) \left\langle pq_0 | P | p'q' \right\rangle \left\langle p'q' | T | \varphi\, q_0 \right\rangle \\
&= \int\int\int dpp^2 dp'p'^2 dq'q'^2 \varphi(p) \int_{-1}^{1} dx \frac{\delta(p-\pi_1)}{p\pi_1} \frac{\delta(p'-\pi_2)}{p\pi_2} \left\langle p'q' | T | \varphi\, q_0 \right\rangle \\
&= \int_{-1}^{1} dx \int dq'q'^2 \varphi(\pi_1) \left\langle \pi_2 q' | T | \varphi\, q_0 \right\rangle \\
&= \int_{-1}^{1} dx \int dq'q'^2 \varphi(\pi_1) \frac{\langle \pi_2 q' | \hat{T} | \varphi\, q_0 \rangle}{E - 3q'^2/4m - \epsilon_d} \\
&= \int_{-1}^{1} dx \int dq'q'^2 \varphi(\pi_1) \frac{\langle \pi_2 q' | \hat{T} | \varphi\, q_0 \rangle}{(3/4m)(q_0^2 - q'^2)} \\
&= \frac{4m}{3} \int_{-1}^{1} dx \int dq'q'^2 \varphi(\pi_1) \frac{\langle \pi_2 q' | \hat{T} | \varphi\, q_0 \rangle}{(q_0 + q')(q_0 - q')} \\
&\to \frac{4m}{3} \int_{-1}^{1} dx \int dq'q'^2 \varphi(\pi_1) \frac{\langle \pi_2 q' | \hat{T} | \varphi\, q_0 \rangle}{(q_0 + q')(q_0 - q' + i\epsilon)} \\
&= \frac{4m}{3} \int_{-1}^{1} dx \int dq'q'^2 \varphi(\pi_1) \frac{\langle \pi_2 q' | \hat{T} | \varphi\, q_0 \rangle}{(q_0 + q')(q_0 - q' + i\epsilon)} \\
&= \frac{4m}{3} \sum_k \int_{-1}^{1} dx \int dq'q'^2 \varphi(\pi_1) S_k^{(p)}(\pi_2) \frac{\langle p_k q' | \hat{T} | \varphi\, q_0 \rangle}{(q_0 + q')(q_0 - q' + i\epsilon)} \\
&= \frac{4m}{3} \sum_k \int_{-1}^{1} dx \Bigg[\int dq'q'^2 \varphi(\pi_1) S_k^{(p)}(\pi_2) \frac{\langle p_k q' | \hat{T} | \varphi\, q_0 \rangle}{(q_0 + q')(q_0 - q')} + \\
&\frac{q_0}{2} \varphi(\pi_1^{(0)}) S_k^{(p)}(\pi_2^{(0)}) \left\langle p_k q_0 | \hat{T} | \varphi\, q_0 \right\rangle \Delta \Bigg]
\end{aligned}
\tag{6.65}
$$

where

$$
\begin{aligned}
\pi_1 &= \sqrt{\frac{1}{4} q_0 + q'^2 + q_0 q' x} \\
\pi_2 &= \sqrt{q_0 + \frac{1}{4} q'^2 + q_0 q' x} \\
\Delta &= \log\left(\frac{q_0}{\Lambda_q - q_0}\right) - i\pi - \sum_{l'} \frac{w_{l'}}{q_0 - q_{l'}}.
\end{aligned}
\tag{6.66}
$$

Once we have U, we can calculate the atom-dimer phase shift δ by the following. Again, we are working in the partial wave basis. Explicitly, we calculate

$$\langle \varphi q_0 | U | \varphi q_0 \rangle \tag{6.67}$$

which relates to the amplitude in Cartesian-momentum coordinates by

$$\langle \phi | U | \phi \rangle = \frac{\langle \varphi q_0 | U | \varphi q_0 \rangle}{4\pi}. \tag{6.68}$$

Now, (6.59) looks like

$$M(\vec{q}_0, \vec{q}_0) \equiv -\frac{2}{3} m (2\pi)^2 \frac{\langle \varphi q_0 | U | \varphi q_0 \rangle}{4\pi}. \tag{6.69}$$

M is the elastic scattering amplitude, so we relate it to the partial-wave phase shifts by

$$M = \sum_l \frac{2l+1}{k \cot \delta_l - ik} P_l(\cos\theta). \tag{6.70}$$

Only considering s-waves, we have

$$\begin{aligned} M &= \frac{1}{k \cot \delta_0 - ik} \\ \implies \frac{1}{M} &= k \cot \delta_0 - ik \\ \implies k \cot \delta_0 &= \frac{1}{M} + ik \\ \cot \delta_0 &= \frac{1}{Mk} + i = \frac{1 + iMk}{Mk} \\ \tan \delta_0 &= \frac{Mk}{1 + iMK} \\ \implies \delta_0 &= \tan^{-1}\left(\frac{Mk}{1 + iMK} \right). \end{aligned} \tag{6.71}$$

Now we have a relationship between the three-body T-matrix and the phase shift δ.

Bibliography

[1] Acharya, B., Ekström, A., Odell, D., Papenbrock, T., and Platter, L. (2017). Corrections to nucleon capture cross sections computed in truncated Hilbert spaces. *Phys. Rev.*, C95(3):031301. 1

[2] Aziz, R. A. and Slaman, M. J. (1991). An examination of ab initio results for the helium potential energy curve. *The Journal of Chemical Physics*, 94(12):8047–8053. 65

[3] Barrett, B. R., Navrátil, P., and Vary, J. P. (2013). Ab initio no core shell model. *Prog. Part. Nucl. Phys.*, 69(0):131 – 181. 1

[4] Beane, S. R. et al. (2001). Singular potentials and limit cycles. *Phys. Rev. A*, 64:042103. 25, 33

[5] Beane, S. R., Kaplan, D. B., and Vuorinen, A. (2009). Perturbative nuclear physics. *Phys. Rev.*, C80:011001. 49, 51

[6] Binder, S. et al. (2018). Few-nucleon and many-nucleon systems with semilocal coordinate-space regularized chiral nucleon-nucleon forces. *Phys. Rev.*, C98(1):014002. 114

[7] Birse, M. C. (2006). Power counting with one-pion exchange. *Phys. Rev. C*, 74:014003. 22

[8] Braaten, E. and Hammer, H. W. (2006). Universality in Few-body Systems with Large Scattering Length. *Phys. Rept.*, 428:259–390. 69, 70, 73

[9] Cockrell, C., Vary, J. P., and Maris, P. (2012). Lithium isotopes within the *ab initio* no-core full configuration approach. *Phys. Rev. C*, 86:034325. 3

[10] Deltuva, A. (2015). Momentum-space calculation of 4he triatomic system with realistic potential. *Few-Body Systems*, 56(11):897–903. xv, 81, 85

[11] Efimov, V. (1970). Energy levels arising from resonant two-body forces in a three-body system. *Phys. Lett.*, 33B:563. 70

[12] Entem, D. R. and Machleidt, R. (2003). Accurate charge-dependent nucleon-nucleon potential at fourth order of chiral perturbation theory. *Phys. Rev. C*, 68:041001. 15

[13] Epelbaum, E., Hammer, H.-W., and Meissner, U.-G. (2009). Modern Theory of Nuclear Forces. *Rev. Mod. Phys.*, 81:1773–1825. 21, 22

[14] Epelbaum, E., Krebs, H., and Meißner, U. G. (2015). Improved chiral nucleon-nucleon potential up to next-to-next-to-next-to-leading order. *The European Physical Journal A*, 51(5):53. 22, 25, 114

[15] Feshbach, H. (1962). A unified theory of nuclear reactions. ii. *Annals of Physics*, 19(2):287 – 313. 69

[16] Forssén, C., Roth, R., and Navrátil, P. (2013). Systematics of 2 + states in c isotopes from the no-core shell model. *Journal of Physics G: Nuclear and Particle Physics*, 40(5):055105. 3

[17] Frank, W., Land, D. J., and Spector, R. M. (1971). Singular potentials. *Rev. Mod. Phys.*, 43:36–98. 23

[18] Furnstahl, R. J., Hagen, G., and Papenbrock, T. (2012). Corrections to nuclear energies and radii in finite oscillator spaces. *Phys. Rev. C*, 86:031301. 2

[19] Furnstahl, R. J., Hagen, G., Papenbrock, T., and Wendt, K. A. (2015). Infrared extrapolations for atomic nuclei. *Journal of Physics G: Nuclear and Particle Physics*, 42(3):034032. 2

[20] Furnstahl, R. J., More, S. N., and Papenbrock, T. (2014). Systematic expansion for infrared oscillator basis extrapolations. *Phys. Rev. C*, 89:044301. 2, 4, 5, 6

[21] Gao, B. (1998a). Quantum-defect theory of atomic collisions and molecular vibration spectra. *Phys. Rev. A*, 58:4222–4225. 65, 66, 82

[22] Gao, B. (1998b). Solutions of the schrödinger equation for an attractive $1/r^6$ potential. *Phys. Rev. A*, 58:1728–1734. 66

[23] Gao, B. (1999). Repulsive $1/r^3$ interaction. *Phys. Rev. A*, 59:2778–2786. 22

[24] Gao, B. (2001). Angular-momentum-insensitive quantum-defect theory for diatomic systems. *Phys. Rev. A*, 64:010701. 49

[25] Gezerlis, A., Tews, I., Epelbaum, E., Gandolfi, S., Hebeler, K., Nogga, A., and Schwenk, A. (2013). Quantum Monte Carlo Calculations with Chiral Effective Field Theory Interactions. *Phys. Rev. Lett.*, 111(3):032501. 22

[26] Glöckle, W., Hasberg, G., and Neghabian, A. R. (1982). Numerical treatment of few body equations in momentum space by the spline method. *Zeitschrift für Physik A Atoms and Nuclei*, 305(3):217–221. 97

[27] Gloeckle, W., Witala, H., Huber, D., Kamada, H., and Golak, J. (1996). The Three nucleon continuum: Achievements, challenges and applications. *Phys. Rept.*, 274:107–285. 30, 99, 102

[28] Glöckle, W. (1983). *The Quantum Mechanical Few-Body Problem.* Texts and Monographs in Physics. Springer, Berlin. 29, 96

[29] Grießhammer, H. W. (2016). Assessing Theory Uncertainties in EFT Power Countings from Residual Cutoff Dependence. *PoS*, CD15:104. 22, 33, 37

[30] Hagen, G., Papenbrock, T., Dean, D. J., and Hjorth-Jensen, M. (2010). *Ab initio* coupled-cluster approach to nuclear structure with modern nucleon-nucleon interactions. *Phys. Rev. C*, 82:034330. 2

[31] Hammer, H.-W., Nogga, A., and Schwenk, A. (2013). Three-body forces: From cold atoms to nuclei. *Rev. Mod. Phys.*, 85:197. 21

[32] Jurgenson, E. D., Navrátil, P., and Furnstahl, R. J. (2011). Evolving nuclear many-body forces with the similarity renormalization group. *Phys. Rev. C*, 83:034301. 2

[33] Lepage, G. P. (1997). How to renormalize the Schrodinger equation. In *Nuclear physics. Proceedings, 8th Jorge Andre Swieca Summer School, Sao Jose dos Campos, Campos do Jordao, Brazil, January 26-February 7, 1997*, pages 135–180. 18

[34] Long, B. and van Kolck, U. (2008). Renormalization of Singular Potentials and Power Counting. *Annals Phys.*, 323:1304–1323. 47, 50

[35] Long, B. and Yang, C. J. (2012). Renormalizing Chiral Nuclear Forces: Triplet Channels. *Phys. Rev.*, C85:034002. 22

[36] Lynn, J. E. and Schmidt, K. E. (2012). Real-space imaginary-time propagators for non-local nucleon-nucleon potentials. *Phys. Rev. C*, 86:014324. 22

[37] Machleidt, R. and Entem, D. (2011). Chiral effective field theory and nuclear forces. *Physics Reports*, 503(1):1 – 75. 6, 21

[38] Maris, P., Vary, J. P., and Navrátil, P. (2013). Structure of $A = 7 - 8$ nuclei with two-plus three-nucleon interactions from chiral effective field theory. *Phys. Rev. C*, 87:014327. 3

[39] More, S. N., Ekström, A., Furnstahl, R. J., Hagen, G., and Papenbrock, T. (2013). Universal properties of infrared oscillator basis extrapolations. *Phys. Rev. C*, 87:044326. 2, 13

[40] Müller, T.-O. (2013). Threshold law for attractive inverse-cube interactions. *Phys. Rev. Lett.*, 110:260401. 22, 47

[41] Naidon, P. and Endo, S. (2017). Efimov physics: a review. *Reports on Progress in Physics*, 80(5):056001. 65, 69

[42] Navrátil, P., Quaglioni, S., Stetcu, I., and Barrett, B. R. (2009). Recent developments in no-core shell-model calculations. *Journal of Physics G: Nuclear and Particle Physics*, 36(8):083101. 1

[43] Nogga, A., Timmermans, R. G. E., and van Kolck, U. (2005). Renormalization of one-pion exchange and power counting. *Phys. Rev. C*, 72:054006. 22, 29, 35, 49, 54, 57, 60

[44] Odell, D., Deltuva, A., Bonilla, J., and Platter, L. (2019). Renormalization of a Finite Range Inverse Cube Potential. 21

[45] Odell, D., Papenbrock, T., and Platter, L. (2016). Infrared extrapolations of quadrupole moments and transitions. *Phys. Rev.*, C93(4):044331. 1

[46] Pauli, W. and Villars, F. (1949). On the invariant regularization in relativistic quantum theory. *Rev. Mod. Phys.*, 21:434–444. 51

[47] Pavon Valderrama, M. and Ruiz Arriola, E. (2004). Renormalization of nn-scattering with one pion exchange and boundary conditions. *Phys. Rev.*, C70:044006. 22

[48] Pavon Valderrama, M. and Ruiz Arriola, E. (2005). Renormalization of the deuteron with one pion exchange. *Phys. Rev.*, C72:054002. 22, 35

[49] Pavón Valderrama, M. and Phillips, D. R. (2015). Power Counting of Contact-Range Currents in Effective Field Theory. *Phys. Rev. Lett.*, 114(8):082502. 48

[50] Press, W. H., Teukolsky, S. A., Vetterling, W. T., and Flannery, B. P. (2007). *Numerical Recipes 3rd Edition: The Art of Scientific Computing*. Cambridge University Press, New York, NY, USA, 3 edition. 88

[51] Roggero, A., Mukherjee, A., and Pederiva, F. (2014). Quantum Monte Carlo with non-local chiral interactions. *J. Phys. Conf. Ser.*, 527:012003. 22

[52] Song, Y.-H., Lazauskas, R., and van Kolck, U. (2017). Triton binding energy and neutron-deuteron scattering up to next-to-leading order in chiral effective field theory. *Phys. Rev.*, C96(2):024002. 22, 23, 31, 32, 35, 49, 54, 60, 61

[53] Sprung, D. W. L., van Dijk, W., Wang, E., Zheng, D. C., Sarriguren, P., and Martorell, J. (1994). Deuteron properties using a truncated one pion exchange potential. *Phys. Rev. C*, 49:2942–2949. 22, 35

[54] Stapp, H. P., Ypsilantis, T. J., and Metropolis, N. (1957). Phase-shift analysis of 310-mev proton-proton scattering experiments. *Phys. Rev.*, 105:302–310. 52

[55] Stetcu, I., Barrett, B., and van Kolck, U. (2007). No-core shell model in an effective-field-theory framework. *Phys. Lett. B*, 653(2–4):358 – 362. 2

[56] Varshalovich, D. A., Moskalev, A. N., and Khersonsky, V. K. (1988). *Quantum Theory of Angular Momentum*. World Scientific, Singapore. 4

[57] Wendt, K. A., Forssén, C., Papenbrock, T., and Sääf, D. (2015). Infrared length scale and extrapolations for the no-core shell model. *Phys. Rev. C*, 91:061301. 2

[58] Yang, C. J., Elster, C., and Phillips, D. R. (2008). Subtractive renormalization of the NN scattering amplitude at leading order in chiral effective theory. *Phys. Rev.*, C77:014002. 54

Appendices

A Local Regulator Sensitivity

To regulate the interaction

$$-C_3\frac{e^{-m_\pi r}}{r^3}\ , \tag{72}$$

a general (local) regulator of the form

$$(1-e^{-(r/R)^{n_1}})^{n_2}\ , \tag{73}$$

can be used. Our earliest calculations using the semi-local regulation scheme used $n_1 = 3$ and $n_2 = 1$. However, we observed some unexpected cutoff dependence in the phase shifts as shown in Fig. A.1. Simply increasing the n_2 to 4 removes the dramatic changes in the phase shift. We have also compared our local regulators with those used by others [14, 6]. In the interest of consistency and to ensure we avoid unexpected cutoff dependence, we have used a local regulator of the form $n_1 = 2$ and $n_2 = 4$ for the calculations carried out it in this work. The unexpected cutoff dependence was observed exclusively when using semi-local regulation.

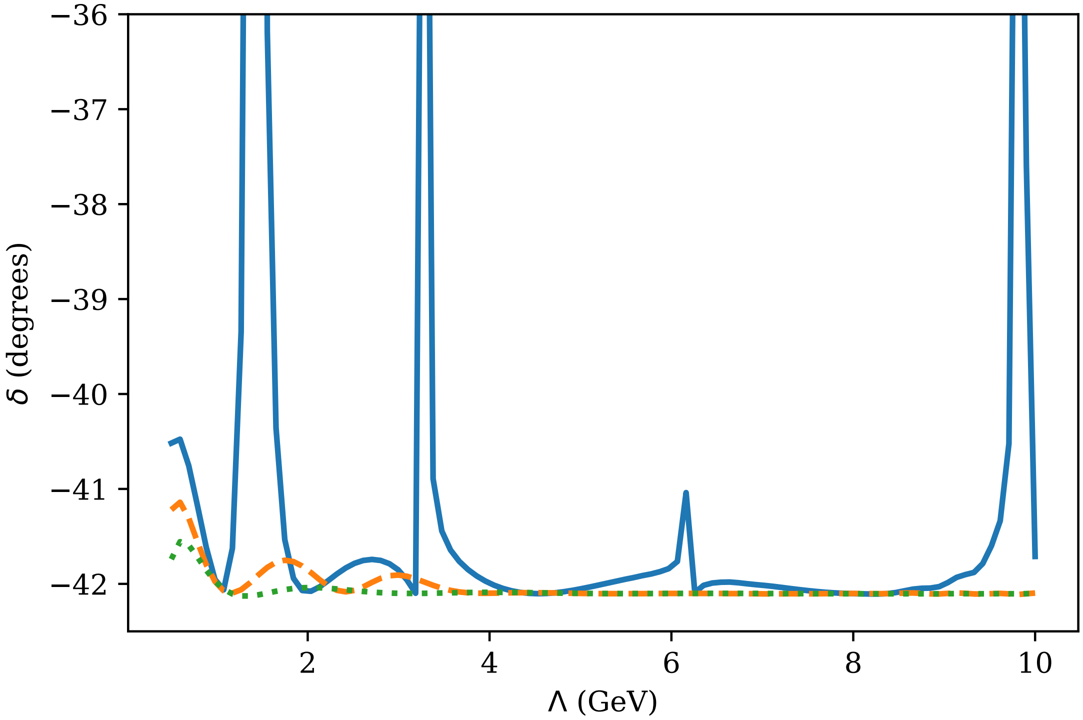

Figure A.1: Phase shifts at a center-of-mass energy of 1 MeV for three different regulators. Per Eq. (73), the solid, blue line corresponds to $n_1 = 3$ and $n_2 = 1$. The dashed, yellow line corresponds to $n_1 = 4$ and $n_2 = 1$. The dotted, green line corresponds to $n_1 = 2$ and $n_2 = 4$.

Vita

Daniel Odell received his BS in Physics at Clemson University in 2007. He was a Scientist at the Savannah River National Laboratory for three and a half years working on the Stockpile Stewardship Program. He taught high school science for two years before enrolling in graduate school at the University of Tennessee in 2013. Upon the successful completion of his PhD, he will begin as a Postdoctoral Researcher at Ohio University.